Land conversions not climate effects are the dominant consequence of sun-driven CO_2 capture, conversion, and sequestration

Moritz Adam[1,*,+], *ORCiD: 0000-0002-8794-958X*
Thomas Kleinen[2], *ORCiD: 0000-0001-9550-5164*
Matthias M. May[3], *ORCiD: 0000-0002-1252-806X*
Kira Rehfeld[1,*,+], *ORCiD: 0000-0002-9442-5362*

[1]University of Tübingen, Department of Geosciences
[2]Max Planck Institute for Meteorology, Hamburg
[3]University of Tübingen, Institute of Physical and Theoretical Chemistry
[*]Correspondence: M. Adam (moritz.adam@uni-tuebingen.de) and K. Rehfeld (kira.rehfeld@uni-tuebingen.de)
[+]Mastodon: @spacy@bawü.social

— In review at Environmental Research Letters (ERL) —

Land conversions not climate effects are the dominant consequence of sun-driven CO_2 capture, conversion, and sequestration

Moritz Adam[1,*], *ORCiD: 0000-0002-8794-958X*
Thomas Kleinen[2], *ORCiD: 0000-0001-9550-5164*
Matthias M. May[3], *ORCiD: 0000-0002-1252-806X*
Kira Rehfeld[1,*], *ORCiD: 0000-0002-9442-5362*

[1]University of Tübingen, Department of Geosciences
[2]Max Planck Institute for Meteorology, Hamburg
[3]University of Tübingen, Institute of Physical and Theoretical Chemistry
[*]Correspondence: M. Adam (moritz.adam@uni-tuebingen.de) and K. Rehfeld (kira.rehfeld@uni-tuebingen.de)

Abstract Removing carbon dioxide (CO_2) from the atmosphere is required for mitigating climate change. Large-scale direct air capture combined with injecting CO_2 into geological formations could retain carbon long-term, but demands a substantial amount of energy, pipeline infrastructure, and suitable sites for gaseous storage. Here, we study Earth system impacts of modular, **s**un-powered process chains, which combine **d**irect **a**ir **c**apture with (electro)chemical **c**onversion of the captured CO_2 into liquid or solid sink products and subsequent product **s**torage (sDACCCS). Drawing on a novel explicit representation of CO_2 removal in a state-of-the-art Earth system model, we find that these process chains can be renewably powered and have minimal implications for the climate and carbon cycle. However, to stabilize the planetary temperature two degrees above pre-industrial levels, CO_2 capturing, conversion, and associated energy harvest demand up to 0.46% of the global land area in a high-efficiency scenario. This global land footprint increases to 2.82% when assuming present-day technology and pushing to the bounds of removal. Mitigating historical emission burdens within individual countries in this high-removal scenario requires converting an area equivalent to 40% of the European Union's agricultural land. Scenarios assuming successful technological development could halve this environmental burden, but it is uncertain to what degree they could materialize. Therefore, ambitious decarbonization is vital to reduce the risk of land use conflicts if efficiencies remain lower than expected.

Introduction

Current and pledged efforts to reduce greenhouse gas emissions are insufficient to achieve net-zero CO_2 emissions in 2050 and the Paris Agreement's target in 2100 [1, 2]. To avoid exceeding future carbon emission budgets, climate change mitigation scenarios heavily rely on artificial carbon dioxide removal (CDR) from the atmosphere [3]. Proposed CDR approaches on land include but are not limited to forestation, bioenergy production with carbon capture and sequestration (BECCS), changing agricultural practices, enhancing mineral weathering, and different process chains which combine direct air capture (DAC) and subsequent carbon storage [4]. They differ in resource and cost efficiency, technological readiness, and environmental implications [5, 6]. Environmental consequences include pressure on land resources, biodiversity, and food, exacerbated by a growing population [7]. Therefore, a portfolio of CDR measures is most likely to emerge with continuously improving operability and scalability [8].

Removing CO_2 in the projected order of 10 gigatonnes per year or more [3, 6] will demand natural and economic resources [9]. CO_2 fixation based on natural processes, such as forestation, BECCS, or enhanced weathering, is associated with high land and resource demand [8, 9, 10]. Biomass plantations also increase the use of freshwater and fertilizers and can offset

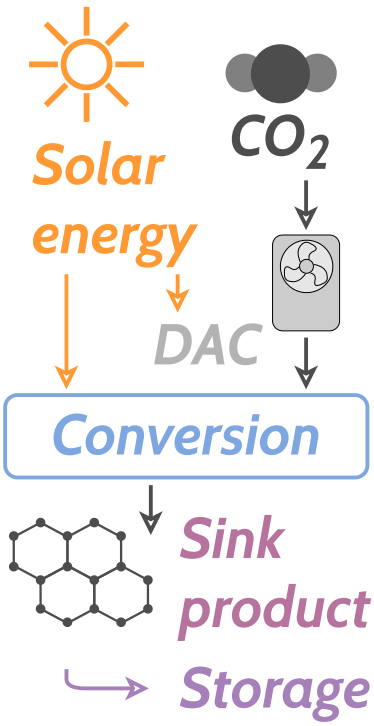

Figure 1 | The concept of sun-powered direct air capture, CO_2 conversion, and sink product storage (sDACCCS). Here, we assume photovoltaics to power the DAC process stage. Solar energy also drives the electrochemical conversion of captured CO_2. The conversion into a permanently storable, carbon-rich, and low-energy sink product either takes place in an integrated, photoelectrochemical device or the solar absorber and electrolysis are separated.

their mitigation potential through biogeochemical and -physical effects [11, 12]. Given their constraints, meeting large-scale CDR targets exclusively with nature-based CDR is impossible within the planetary boundaries [6, 11, 12]. These deficits make large-scale CO_2 fixation with purely technological DAC attractive. DAC is often understood to deliver CDR as part of a process chain that injects the captured CO_2 gas into bedrock or abandoned oil and gas fields [4, 13]. However, process chains complementing DAC with (electro)chemical CO_2 conversion into sink products and storage of the products were also proposed (DACCCS) and could be solar-powered (sDACCCS, Figure 1) [14, 15]. Carbon-rich but low-energy liquids or solids like formate or oxalate are particularly suitable for long-term CDR because they are easy to store and maximize removed carbon per unit of energy invested [14].

DAC process chains promise higher land use efficiencies than, for example, biomass-based CDR, which may omit adverse climatological and biogeochemical effects [9]. Still, they are technologically immature, cost-intensive, and energy-demanding [5, 6, 16]. Environmental consequences, including land cover change, are often assumed to be low [16, 17]. The consequences are, however, poorly constrained from an Earth system perspective, especially for process chains requiring energy for CO_2 conversion [6, 18, 19]. Also, the number of safe storage sites is limited [6], and process chains building on direct gas injection for carbon storage could increase the profitability of fossil fuel exploitation [13, 20, 21]. Here, proposed process chains targeting carbon-rich solid or liquid sink products for permanent storage by (electro)chemically converting the captured CO_2 provide an alternative [14, 15]. This approach would avoid incentivizing hydrocarbon fuels because it maximizes the carbon and not the energy content in the sink products and expands the scope of suitable storage sites beyond sealed geological reservoirs.

Uncertainty dimension	Spread covered by simulation experiments	
CDR share in mitigation	***min*** – As implicitly contained in SSP 1-2.6 [29, 30]	***max*** – Pushing the limits of DAC deployment [cf. 6]
Deployment location	***Eql*** – Delocalized across suitable locations	***Prop*** – Localized according to emission burden [31]
Technological efficiency	***hE*** – Highly efficient, hoped-for technologies [14, 32, 33, 34]	***lE*** – Present-day process chain [35, 32, 33, 34]

Control experiment	Description	Purpose
Pathway control	Only implicit CDR	Evaluate implications of explicit CDR
Control	Equilibrium simulation starting from 2015 emissions	Estimate internal model variability

Table 1 | Covering the uncertainty space with scenarios for sDACCCS deployment. All CDR experiments and the pathway control simulation target SSP1-2.6 [29, 30] and are CO_2 emission-forced.

Converting captured CO_2 into carbon-rich but low-energy sink products can be achieved with electrochemistry. The energy for the electrochemical CO_2 conversion can either be supplied externally, for example through photovoltaics, or by a solar absorber that integrates with the catalytic conversion reaction [14, 15]. At present, industrial-scale electrolysis would already be available for producing sink products out of CO_2 and high conversion efficiencies have generally been demonstrated [22]. However, integrated, photoelectrochemical designs with a solar absorber in direct contact to the electrodes offers great benefits for conversion efficiencies [14, 15] and are actively developed on a lab scale. Conversion efficiencies promise more efficient use of land resources than natural photosynthesis, but have not been scrutinized in any scenario experiments. Aside from the sink product design that maximizes safe CO_2 removal per unit of energy invested, sDACCCS can operate off the energy grid and neither requires the suitable sites and legal framework for gas injection nor extensive infrastructure for CO_2 transport. This modularity could facilitate fast scale-up. However, combining DAC-based process chains with a carbon-free energy supply is crucial for carbon-negativity, no matter if they achieve long-term carbon removal by storing CO_2 gas or a sink product [23, 24, 25, 26]. Including this energy harvest in the assessment of DAC-based technology is essential because the technology could, otherwise, be carelessly perceived as a high-gain, low-side effect promise for reaching net-negative greenhouse gas emission budgets and offsetting residual emissions [27, 8, 19].

Modular DACCCS process chains could be a strategic addition to future CDR portfolios. However, their requirements for natural resources and monetary investments are uncertain [6]. Incorporating potential pitfalls like non-CO_2 effects within the Earth system into the design of CDR portfolios is equally important [28], especially if risks arise from CDR approaches falling short of high expectations. However, large-scale Earth system impacts of DACCCS including the required renewable energy harvest have not yet been assessed. Therefore, we examine implications of exemplary DACCCS process chains targeting a solid sink product within an Earth system model. We investigate CO_2 capture and conversion into formate (HCO_2^-) along two technological pathways, one building on present-day and one on hoped-for technology. To keep the scenarios comparable, we assume solar energy to drive the capturing and conversion stages in both of them. This on-site energy harvest is included in the sDACCCS process chains' land demand without relying on grid electricity. To include pathway dependencies and achieve comparability with other Earth system simulations, we conduct model experiments with a time-dependent CDR target, emission forcing, and land use scenario.

Our simulations cover three pivotal uncertainty dimensions for Earth system implications sDACCCS: (i) reliance on CDR, (ii) spatial deployment, and (iii) technological efficiency (Table 1; further details on the scenario design in the methods section). Side effects typically scale with the need for CDR, the first uncertainty dimension. Our simulation ensemble covers a low and a high level of explicit CDR forcing, which both result in a net emission forcing compatible with the extended shared socioeconomic pathway [29, 30] (SSP) 1-2.6. Given the Earth system's heterogeneity, the localization of CDR can be relevant for its Earth system implications. Here, two stylized burden-sharing scenarios span the uncertainty space of potential sDACCCS de-

ployment locations. Finally, the energy efficiency of any terrestrial CDR process chain influences its land use efficiency [9, 25]. In our experiments, sDACCCS efficiencies either correspond to a present-day technology state employing DAC with industrial-scale electrolysis or a state combining DAC with integrated photoelectrochemical CO_2 conversion. Both technology scenarios assume solar energy to power the whole sDACCCS process chain.

We examine the impact of sDACCCS on climate, land carbon stocks, and land cover at regional and global levels, utilizing a state–of–the–art Earth system model (ESM). To our knowledge, the framework, as described in the subsequent methods section, is the first explicit, interactive, and dynamic representation of a purely technological CDR approach in an ESM [cf. 12, 18, 36]. The implementation allows us to explicitly simulate first-order interactions of sDACCCS with the climate and carbon cycle, including those induced by solar energy harvest, physical surface modifications, and land use change. In emission-driven experiments spanning the three uncertainty dimensions identified above (Methods), we dynamically adjust the CDR cover in space and time in response to actual CO_2 removal. We can hereby establish a first estimate for the climatic impact and land footprint of the different sDACCCS process chains and scenarios up to the year 2200. Within the limitations of our model, we find no significant and persistent non-CO_2 effects on the climate and terrestrial carbon cycle (Results, Discussion). However, depending on technological progress and spatial layout, the land conversions associated with sDACCCS (Results) could co-determine if societies want to implement such highly efficient but costly CDR approaches (Discussion).

Methods

We employ a modified version of the Max Planck Institute for Meteorology Earth system model v1.2 (MPI-ESM) [37, 38] to quantify interactions of sDACCCS within the Earth system. MPI-ESM is specifically calibrated to the anthropogenic warming [37] and contributes to IPCC's physical science basis through the coupled model intercomparison project (CMIP) phases 4–6 [39, 37, 18, 40]. The simulated land carbon cycle agrees well with observations [37] and its response to CO_2 forcing is close to the CMIP5 and 6 multi-model means [40]. MPI-ESM contains submodels of the atmosphere [41, 42], land surface [38], ocean and sea ice dynamics [43], and marine biogeochemistry [44]. Its land model JSBACH3.2 is the main interface for incorporating land-based sDACCCS process chains as it provides radiative, momentum, moisture, and gas exchange with the atmosphere. Further, the land model parameterizes vegetation competition, photosynthetic productivity, vegetation–climate interactions, and anthropogenic land use change. Representing sDACCCS in MPI-ESM also requires minor adjustments to the land–atmosphere coupling but they are restricted to passing additional variables between submodels and coupling explicit CDR to the atmospheric balances. We use a horizontal grid spacing of approximately $200\,\mathrm{km}$ for atmosphere and land (T63 spectral truncation) and about $150\,\mathrm{km}$ for the ocean [37].

The representation of sDACCCS process chains within JSBACH has five primary goals: (i) predict their land use requirements under different irradiation conditions, (ii) simulate their impacts on the surface balances that are associated with changes in the physical surface properties, (iii) parametrize the CO_2 sequestration under technological uncertainty, (iv) model changes in sDACCCS land cover and consequences for land-stored carbon interactively and explicitly based on SSP-derived scenarios, and (v) minimize the interference with existing process models to ensure consistency between simulations with and without sDACCCS. Therefore, our main extensions to JSBACH comprise (Figure S1):

- a new land cover class and type which represent sDACCCS in JSBACH's surface tiling

scheme (Supplementary Information (SI))

- an implicit handling of sDACCCS on the unvegetated fraction of land when computing grid cell-averaged surface properties (SI)
- a zero-dimensional parametrization of the CO_2 withdrawal through sDACCCS
- a dynamic scheme for deploying sDACCCS on the land surface based on the simulated potential withdrawal and spatiotemporal CDR targets
- amended rules for anthropogenic land cover change, which prioritize agricultural land use transitions over those through sDACCCS (SI) and cover changes in carbon and nitrogen pools.

Parameterizing CO_2 withdrawal through sDACCCS

The working principle of sDACCCS process chains is to store solar energy in the molecular bonds of liquid or solid carbon-rich products [14]. A solar absorber excites charge carriers through the photoelectric effect. The catalyzed reduction of carbon dioxide molecules subsequently consumes these electrons, either in an integrated device as suggested by May and Rehfeld [14] and covered in our high efficiency (hE) technology scenario or in an industrial-scale electrolysis as assumed in the low efficiency (lE) scenario. Solar energy powers CO_2 capture (hE, lE) and electrolysis (lE).

A zero-dimensional model parameterizes these sDACCCS process chains (Figure S5), by deducing the CO_2 withdrawal from the incident irradiation along a sequence of process steps which consecutively reduce the amount of energy available for CO_2 fixation (SI). From our model's perspective, the lE and hE technology pathways differ by conversion efficiencies along the process chain (all parameters in SI). Thus, by reducing the conversion efficiency, we account for system losses and solar energy harvesting. We choose formate as an exemplary sink product because it has a high, but not optimal solar–to–carbon (STC) efficiency and can form a mineral that is easy to store [14]. Products like oxalate would beat the STC efficiency of formate substantially [14]. Thus, we deliberately assume a moderate upper bound for the maximum removal efficiency of sDACCCS. For the radiative balance, we draw on the radiation scheme of the ECHAM6.3 atmosphere model, but include the thermal cooling effect that results from CO_2 fixation in an integrated process chain.

Irradiation is the only climatic variable directly driving CO_2 sequestration and storage in our model. For hE, assuming no effect of temperature on the catalyzed reaction's efficiency is motivated by the large uncertainties of system efficiencies. In the case of lE, we assume electrolysis temperatures can be controlled. Because technological developments are currently uncertain, we neglect the effect of temperature on the CO_2 capturing stage. Further, we assume conversion efficiencies to level off according to a sigmoid curve at low local CO_2 surface concentrations (SI).

CDR land cover dynamics

Biophysical interactions and feedbacks in the Earth system, such as effects of vegetation composition and land carbon uptake, depend on the CO_2 concentration. Therefore, precisely controlling the effective CO_2 emission forcing is essential for maintaining consistency among sDACCCS simulations and control experiments. However, achieving the same effective forcing, irrespective of individual spatiotemporal CDR targets, is challenging because the explicit CO_2 removal itself responds to climate variability, land availability, and the spatial layout. If only

spatially resolved CDR area changes from theoretical calculations were prescribed, the net emission forcing between experiments and different realizations of the same experiment could drift apart. Therefore, we develop a scheme, which dynamically determines fractional changes in sDACCCS cover based on spatial deployment weights and global SSP-derived CDR targets. The scheme simultaneously accounts for every grid cell's CO_2 withdrawal potential in response to climate variability and land use constraints, corrects previous offsets to the targeted CDR pathway that are due to variability, and determines the necessary land cover change to meet the spatiotemporal CDR targets (SI, Figure S3).

Because CO_2 removal through sDACCCS is explicit in our model, we adapt MPI-ESM's spatially-resolved emission forcing such that the net forcing remains in line with the respective SSP. Starting from a forcing baseline, we rescale all grid cells with a positive emission flux according to their relative contribution to the global emissions (Figure 2a, SI). Greenhouse gases besides CO_2 are concentration-forced and always follow SSP3-7.0. In experiments beyond 2100, we extend the modified CO_2 emission forcing and other greenhouse gas forcings as described by Meinshausen et al. [30]. In all simulations, non-sDACCCS land use forcing [45] follows ScenarioMIP [46] protocols along SSP3-7.0. Different SSP land use forcings could result in incompatible CDR scenarios, because some of them implicitly contain biomass plantations and forestation for CDR purposes. By applying the same forcing baseline in all experiments and not varying land use requirements for any other land cover than sDACCCS, we isolate its effects on the Earth system.

Scenario design

Our study's simulation experiments cover three uncertainty dimensions. The shared socioeconomic pathways [29] (SSPs) and their extensions to 2500 [30] estimate the need for CDR, the first of these dimensions. These pathways provide self-consistent storylines concerning energy demand, warming target, carbon pricing, land use, and the emission budget [29]. Although the SSPs underestimate alternatives to CDR [48], we let emission forcings effectively follow SSP 1-2.6 (Figure 2a, b). SSP1-2.6 is compatible with limiting global warming below 2°C at a probability $> 67\%$ [3]. Because the SSPs do not define spatially explicit DAC targets, this pathway is a globally evolving control for our experiments. To capture a large spread of CDR reliance under the same emission pathway, we further utilize SSP3-7.0, which is close to the world's current emission pathway. Our low-sDACCCS scenario (*min*, Table 1) corresponds to the amount of carbon capture and storage implicitly contained within SSP 1-2.6 [29]. In a second scenario (*max*), we suppose CO_2 emissions to be halfway between the SSP 3-7.0 and SSP 1-2.6 pathways and allocate the excess carbon budget entirely to sDACCCS. While not corresponding to a self-consistent SSP, this scenario allows a test of the Earth system's sensitivity to sDACCCS process chains if the world were locked in on enormous amounts of CDR due to a deferred achievement of net-zero emissions [49]. Reaching ~ 40 Gt CO_2 yearly withdrawal at the end of this century, max is also a potential upper bound for DAC-like CDR [6].

The share of investments, tradeoffs, and gains of large-scale CDR among countries still has to be established [50] while taking appropriate burden sharing [51, 31], technology-specific requirements and land availability (Figure 2c) into account [6]. Here, two burden-sharing scenarios cover this uncertain spatial CDR layout. The *Eql* scenario targets equally dispersed deployment of sDACCCS across grid cells, marking the extreme case of minimized CDR burden per land area (Figure S9). On the other hand, in the *prop* scenario, we demonstrate the implications of distributing future CDR across countries based on their historical emission burden [31, 51] (Figure 2d, Figure S9).

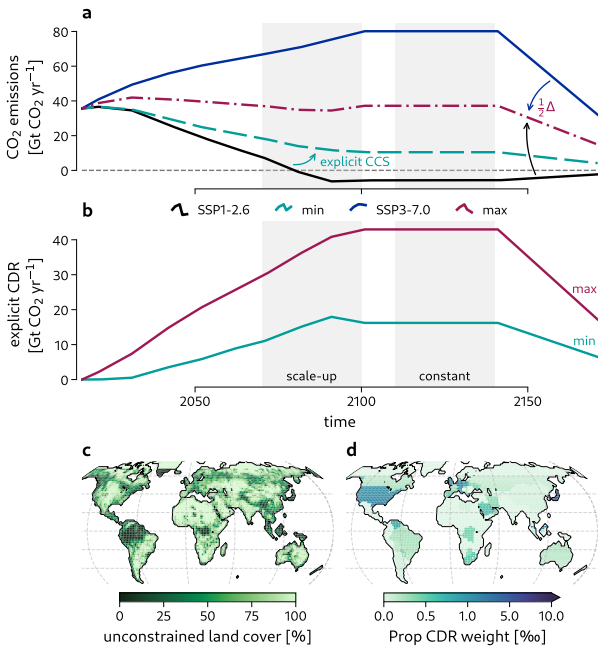

Figure 2 | The projected need for CDR and modeling constraints for solar energy-driven direct air capture, CO_2 conversion, and sink product sequestration (sDACCCS). a, Net CO_2 emissions in SSPs 1-2.6 and 3-7.0 (solid lines) with derived forcing scenarios for the explicit CDR simulations (dashed). For min, we choose SSP1-2.6 as the baseline and add the implicit forcing through carbon capture and storage from the SSP scenario database [29]. In the max experiments, we reduce SSP3-7.0 emissions by half of the difference to SSP1-2.6. **b**, Global, explicit CDR targets resulting in a net forcing compatible with SSP1-2.6 when combined with the derived forcings from **a**. Shadings indicate periods of scale-up and sustained CO_2 removal. **c**, Present-day spatial constraints to sDACCCS deployment [47, 45] (Scenario design). **d**, CDR deployment weights of the prop scenario drawing on country-wise emission burdens [31]. Given solar insolation as primary energy source, the scenario limits deployment to 60°S–60°N (Scenario design).

All stages of DACCCS process chains contribute to their overall efficiency. For sDACCCS, this includes capturing ambient CO_2, converting it into a safely storable sink product, transporting and storing the product, and energy provisioning [14, 52]. In this study, we assume that photovoltaics provide all necessary external energy and include it in the modeling. Present-day DAC facilities combined with industrial-scale electrolytic CO_2 reduction and photovoltaics (lE) would already be available for producing carbon sink products [53]. However, lE has less than optimal conversion efficiencies and is uneconomical. This technology stage still provides a baseline scenario of unrealized technological expectations (3.5% sDACCCS chain efficiency including system losses, SI). In contrast, prospective photoelectrochemical CO_2 reduction which integrates a solar absorber with the catalytic CO_2 reduction [15] (hE) represents a more efficient CO_2 conversion pathway (7.1% chain efficiency, SI). Although derived from specific process chains, one can interpret the uncertainty range spanned by the lE and hE scenarios more widely for any sun-powered DAC chain because the overall chain's efficiency is their single modeling constraint.

Confidence intervals

To gauge the significance of anomalies among different CDR experiments and between simulations with and without explicit CDR representation, we estimate the range of simulated climate variability. The internal model variability is small compared to this climate variability. We ini-

tialize a control simulation with the same 2015 state as all other experiments in our study and run it until 2500. For variability estimates, we report the 95% interquartile range computed from the standard deviation of annual (global carbon stocks, land cover transformations) and three-decadal means (climatic variables, regional anomalies) within the time period from 2260 to 2499 (both years included). Within this period, the control simulation is close to a dynamic equilibrium. We determine confidence ranges after all data processing steps. Thus, we ensure to include non-linear effects of processing operations on uncertainties, for example, when aggregating data over a region.

Results

This section presents our results on potential sDACCCS effects on climate, carbon cycle, and land use in topical segments for each aspect.

Negligible implications for climate of large-scale sDACCCS

A central argument for removing CO_2 through DAC process chains are presumed minor effects on climate, in particular compared to implications of large-scale biomass production [6]. Our experiments confirm that large-scale sDACCCS, which includes solar energy harvest, neither causes additional global climate change (Figure 3) nor substantially shifts regional climate (Figure 4).

The response of the global mean CO_2 concentration and surface air temperature (Figure 3a, e) indicates that none of the three uncertainty dimensions results in a different global climate in the periods of DAC scale-up (anomalies to the pathway control experiment reported for 2069-2099) and constant CDR (2110-2139). Slight differences during CDR scale-down are due to model limitations after 2170 (SI). All experiments fall within the range of the pathway control experiment and meet CDR targets accurately (Figure 3b–d). This suggests that the spatial sDACCCS configuration has a negligible impact on global climate. Thus, it is not per se necessary to represent DAC explicitly in space when considering only the global climate response. However, spatially explicit sDACCCS induces significant changes in surface balances in some IPCC regions (Figure 4a–g). In the extreme case of highly localized CDR cover on the Arabian Peninsula (ARP* region, Figure 4b) within the hEmaxProp experiment, sDACCCS increases the excess downwelling radiation at the surface by 32% (43% in lEmaxProp) through changes in surface albedo (Figure 4a, b). In hEmaxProp, localized sDACCCS also significantly reduces the local CO_2 surface concentration by up to 6.0 ppm in central North America (CNA, 1.4% of the mean), 3.3 ppm in northern and central Europe (NCE, 0.8%), and 1.8 ppm over the Arabian Peninsula (ARP, 0.4%). Except for the Kazakh Steppe and parts of Siberia, impacts on the regional surface energy balance through sDACCCS deployment, as well as interactions with the surface moisture balance (Methods), do not lead to significant local changes in surface air temperature, soil moisture (Figures 4d–g, S17–S18), cloud cover, and precipitation (not shown). Only a few changes stand out against the expected internal variability, such as increased soil moisture in NCE (Figure 4g). Even when technological efficiencies remain low and the CDR deployment is pushed to the upper limit (lEmaxProp), climate implications mostly stay within or close to the range of variability (Figure 4b–g, SI).

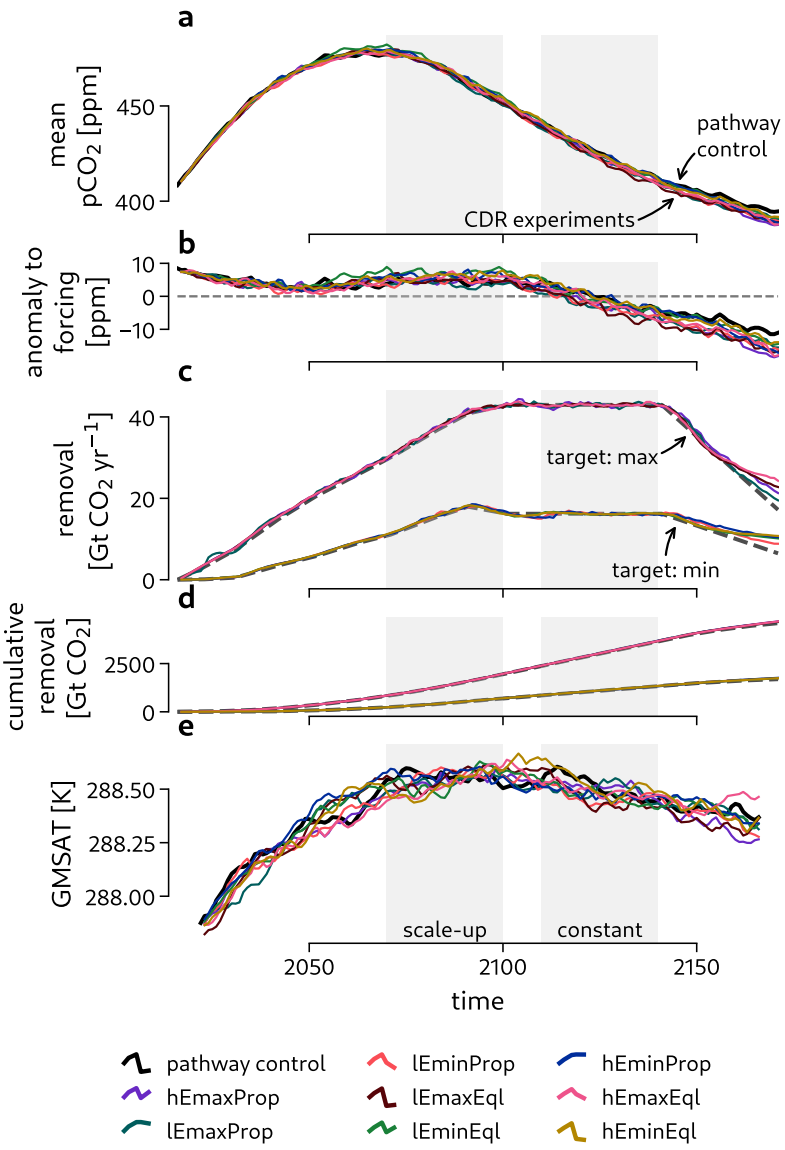

Figure 3 | Global climate response to spatially resolved sDACCCS. a-e, Global mean CO_2 concentration (pCO_2, **a**), anomaly of pCO_2 to SSP-1.26 concentration forcing [29, 30] (**b**), global CO_2 removal rate (**c**), cumulative CO_2 removal (**d**), and global mean surface air temperature (**e**) for pathway control and CDR experiments. Shading highlights periods of final CDR scale-up and constant CDR.

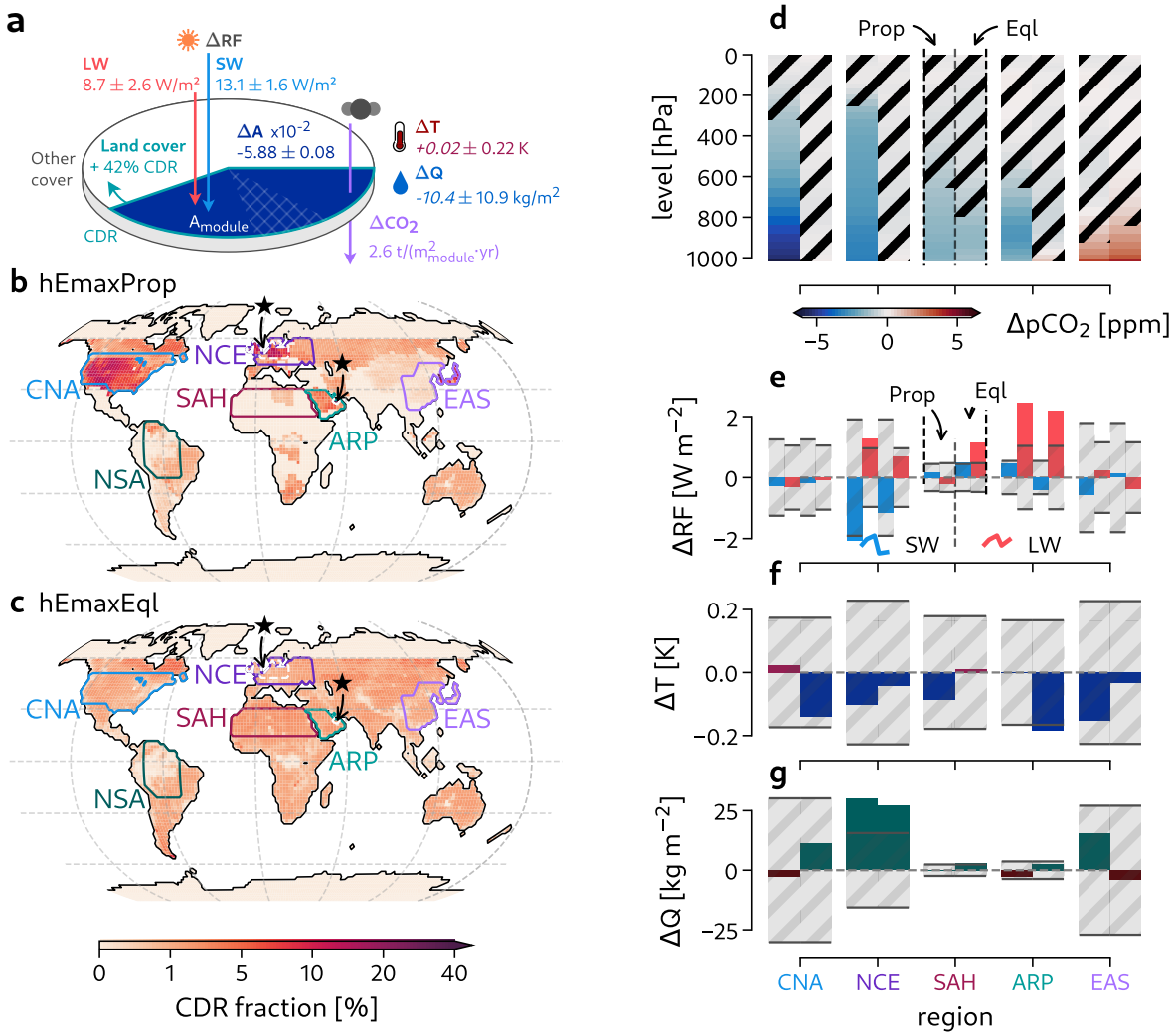

Figure 4 | Regional climate responses to spatially resolved sDACCCS. a, Implications of spatially resolved sDACCCS (CO_2 withdrawal: ΔCO_2) for the energy balance (ΔA albedo change, ΔRF shifts in long-wave (LW) and short-wave (SW) radiative forcing) and climate (ΔT surface air temperature change, ΔQ change in soil moisture) using the ARP* region in hEmaxProp as an example. Insignificant values with respect to 95% of variability in the control experiment are in italics. **b, c**, Mean sDACCCS realized in hEmaxProp and hEmaxEql experiments during the period of constant CDR. Selected IPCC reference regions [54] (SI) are indicated. Stars highlight subregions ARP* and NCE*. **d–g**, Mean anomalies in pCO_2 along the atmospheric column (corrected for global pCO_2 anomaly, **d**), radiative forcing (**e**), surface air temperature (**k**), and soil moisture content (**f**) for the hEmax experiment compared to the pathway control experiment in selected regions during the time period of constant CDR. Hatchings in **g** mask insignificant data with respect to the two-sided 95th percentile of pCO_2 variability in the control experiment and indicate 95% of interquartile ranges of respective variables in the control experiment in **e–g**.

Small but spatially heterogeneous implications of large-scale sDACCCS for the carbon cycle

Many land regions comprise vast vegetated and agricultural lands. Establishing large-scale sDACCCS could decrease land-stored carbon and biospheric carbon uptake, diminishing the net CO_2 removal potential of sDACCCS. However, our simulation results suggest that while the effects on carbon stocks are globally and regionally significant, they do not substantially reduce the removal potential. sDACCCS causes most land cover degradation in the scale-up period (Figure S30), reducing land-stored carbon compared to the baseline experiment (Figure 5 a-d). This dynamic is reflected by decreased natural CO_2 uptake during the scale-up phase (Figure 5e, f). During the time of constant CDR, vegetation carbon stocks and associated biomass litter partially recover in the hEmax experiments globally and in most regions (Figure 5a, d; SI). In the lEmax experiments, this recovery overcompensates previous losses (Figure 5b, SI). At the same time, soil carbon stocks diminished through sDACCCS deployment only show little signs of recovery throughout the scenario (Figure 5a, b). Since the baseline and CDR experiments share the same emission pathway (Figure 2a; Methods), overcompensated losses in vegetation-stored carbon during periods of constant CDR and CDR scale-down are not a result of changing climate and vegetation growth. Instead, sDACCCS shifts dominant vegetation types in all phases of CDR deployment, which explains the overcompensation (SI). Total global average losses in land-stored carbon between 4.4 Gt C (lEminProp) and 12.9 Gt C (lEmaxEql) by 2100 are in the same order of magnitude as sDACCCS' simulated annual removal (17.5 Gt C/yr in lEminProp, 41.1 Gt C/yr in lEmaxEql), but two orders of magnitude smaller than cumulated removals (705 Gt C in lEminProp, 1966 Gt C in lEmaxEql; Figure 2c, d).

Regionally, land carbon is not equally distributed on the land surface [55, 56]. Therefore, the implications of sDACCCS for the carbon cycle depend on the spatial scenario. Our simulations show that minimizing its environmental impact is not only a matter of global localization versus delocalization of sDACCCS. For example, the localized prop scenario results in a higher carbon stock decrease in the CNA and EAS regions than the delocalized eql scenario, which in turn impairs carbon stocks in the NSA region more substantially (Figure 5c-f). This effect propagates to the global scale, with more pronounced vegetation carbon stock anomalies (in reference to baseline) in eql experiments during the period of CDR scale-up and more substantial soil carbon decline in prop simulations from 2090 onwards (Figure 5a, b).

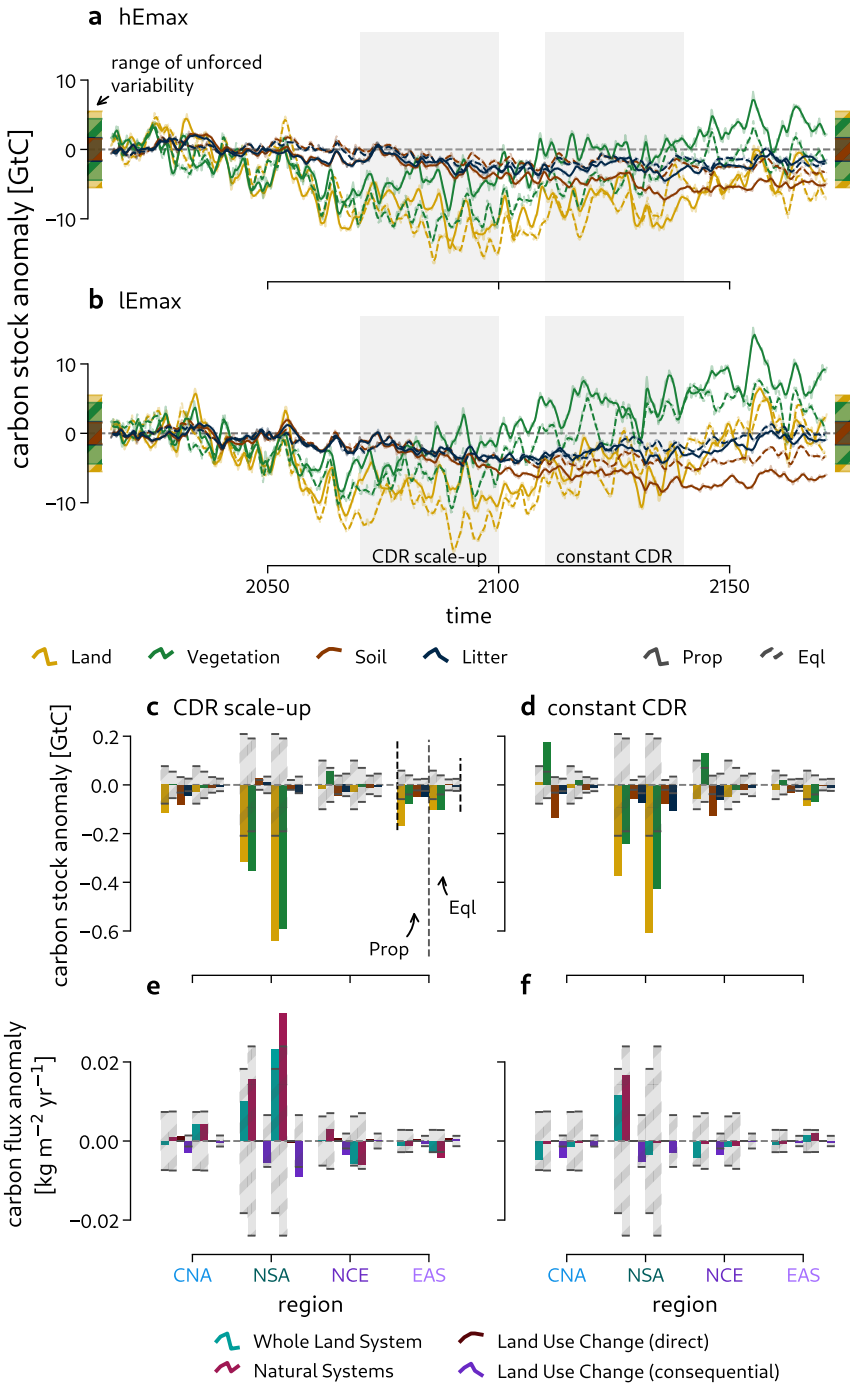

Figure 5 | Effects of sDACCCS on global and regional carbon cycle. a, b, Global carbon stock response of hEmax (a) and lEmax (b) experiments. Land carbon stocks comprise carbon stored in live vegetation, soils, litter, and product pools. As product pools are small compared to the other categories, they have been omitted in the figure. **c, d**, Total carbon stock anomaly of hEmax experiments in selected IPCC regions during periods of CDR scale-up and constant CDR as indicated in **a, b**. **e, f**, as **c, d** but for average carbon fluxes. Here, negative values indicate an increased carbon sink, while positive anomalies reflect increased emissions. Consequential land use change fluxes reflect decreasing emissions through crop harvest, grazing, and product decomposition as a result of establishing sDACCCS land cover instead. All anomalies are with respect to the pathway control simulation. Hatchings indicate the multiannual (**a, b**) and three-decadal 95% (**c-f**) interquartile ranges of the control simulation for comparison.

Potential for land use conflicts

Land is a pivotal, but limited resource for food production, CO_2 buffering, and biodiversity. Land conversion induced by harvesting energy and processing CO_2 through sDACCCS process chains varies between 0.46% (hEminEql) and 2.82% (lEmaxProp) of global land area (Figure 6a, Figure S29), with the technological efficiency as a central parameter for these land conversions. For example, CDR covers 3.46 million km^2 in lEmaxProp, but only 1.69 million km^2 (1.38% of global land area converted) in hEmaxProp, which is in the range of the global urban land area (1.91 million km^2 in 2015 [57]). Compared to the strong effect of efficiency parameters, the localization of sDACCCS is less relevant on a global scale. Increasing the sDACCCS efficiency from lEmaxProp to hEmaxProp causes 44% less grasslands to be replaced (64% less between lEminProp and hEminProp). Conversely, grassland conversion in simulations with localized CDR (Prop) and delocalized deployment (Eql) under the same global CDR scenario only shifts between 7% (hEmax) and 50% (hEmin). Similarly, the higher efficiency of hE process chains can prevent up to 43% (maxEql) of agricultural lands from conversion, while the spread between different localizations is 38% at most (lEmax). At the same time, land cover of trees and shrubs increases in simulations with the lower lE efficiency.

While technological efficiency dominates net land conversions globally, the spatial deployment impacts land use regionally. Considering the core of northern and central Europe (NCE*) in the low-efficient lE max (max) simulations as an example (Figure 6b, c), sDACCCS covers 17.6% of the region in lEmaxProp during the constant CDR period. As many central European countries have a high historical emission burden, the lEmaxEql experiment only converts 2.4% of land in NCE* for CDR. The implications of the historical burden-sharing scenario become more evident when putting these land cover adjustments into perspective. In the lEmaxEql experiment, NCE* loses grass- and agricultural land only slightly above the Earth system's internal variability. Forests and shrubs dynamically adjust in the same order. In contrast, in lEmaxProp, converted grasslands alone correspond to the equivalent of 37% of the European Union's agricultural area during the constant CDR period. Since agricultural lands make up $\sim$48% of the region's entire area [58], this would constitute a significant intervention into the land system. Converted pastures and croplands add the equivalent of another 13%. Roughly doubling the sDACCCS chain's efficiency (hEmax) would approximately halve the pressure of sDACCCS on regional land resources with the equivalent of 2.4% of the EU's agricultural lands converted to CDR in eql and 20% for emission burden sharing (Figure S31). Because of their historical emission burden, similar regional effects apply to central North America, Japan, South Korea, and parts of the Arabian Peninsula (Figure 6c, d). These solid regional effects of sDACCCS cover on land resources indicate that unmatched technological expectations in a high-CDR world could likely lead to target conflicts between CO_2 removal and land resources, ecosystem services, and food production.

Discussion and conclusion

Our study targets unquantified implications of DAC-based process chains on climate, carbon cycle, and land cover identified in IPCC assessments [18, 6]. Leveraging a novel explicit and dynamic representation of land-based CDR in a comprehensive Earth system model, we present simulations of solar energy-powered process chains targeting solid or liquid carbon sink products through direct air capture, CO_2 conversion, and sequestration (sDACCCS). The simulations indicate that large-scale sDACCCS does not substantially offset its climate change mitigation potential by impacting regional surface climate or carbon stocks beyond global-scale effects of CDR on the Earth system [59]. The Kazakh Steppe and adjacent parts of Siberia are an exception where solar energy harvest for sDACCCS increase surface temperature by $\sim$1K. The minor

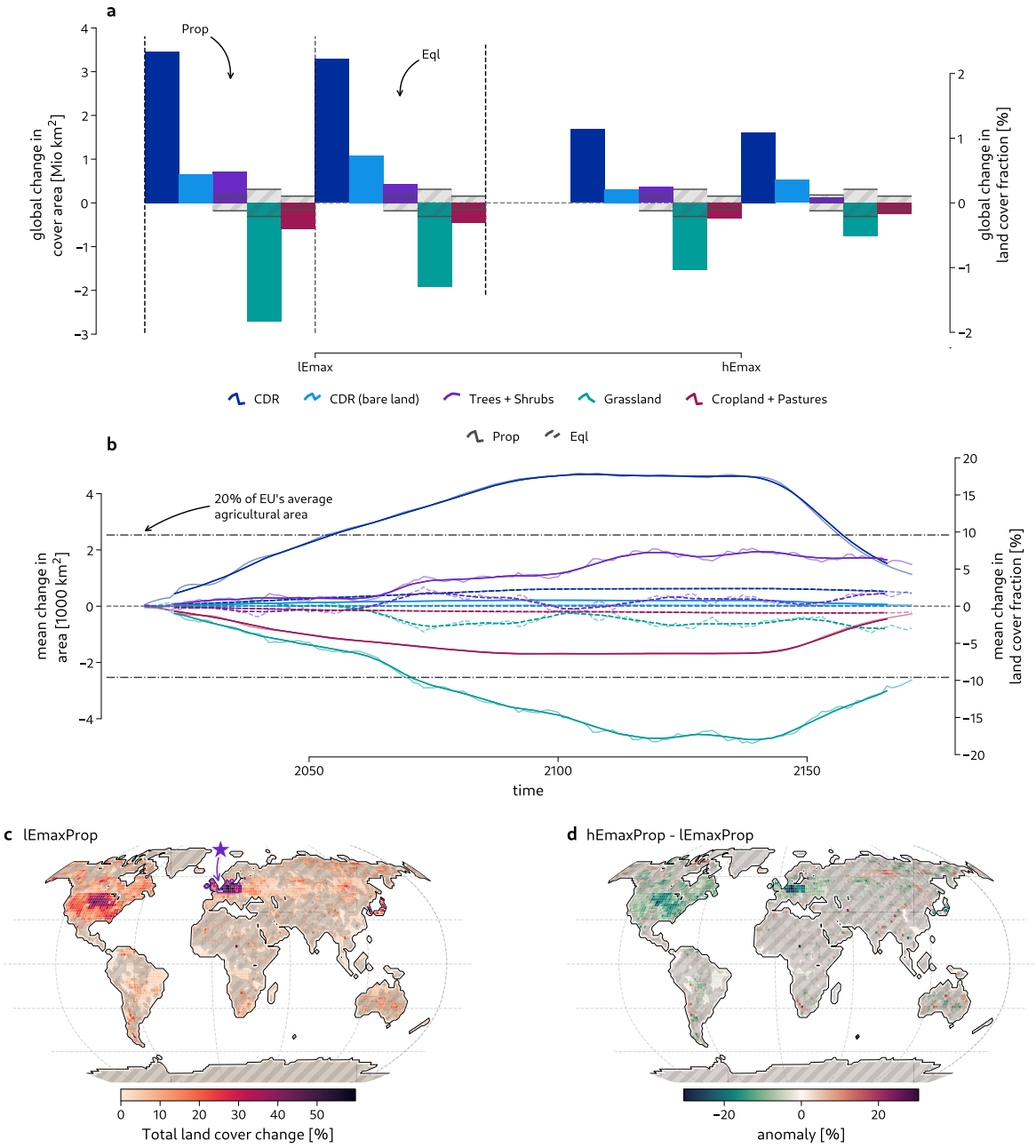

Figure 6 | Land cover transformation resulting from sDACCCS deployment. a, Mean global changes in area and land cover fraction in the period of constant CDR compared to the pathway control simulation for the max (max) lE and hE experiments. The share from CDR cover on bare land is also shown separately. **b**, Land conversions over time in the NCE* region, as indicated in **c**, when comparing lEmaxProp to the pathway control experiment. Shading indicates the time period of constant CDR. Color ranges at the edges of the zero-axis represent the range of intererannual variability in the unforced control experiment. **c**, Total land cover change on potentially vegetated land in the lEmaxProp experiment during the constant CDR time period (see Figure S32 for land cover change on unvegetated land). A star marks the NCE* region. **d**, Reduced land conversion in the experiment with higher sDACCCS efficiency (hEmaxProp) compared to **c**. Hatchings represent the three-decadal 95% interquartile ranges of the control simulation, where applicable (see Methods).

climatic effects contrast the significant ramifications suggested for some large-scale biomass-based CDR [11, 12]. Further, they are orders of magnitude smaller than studies of exascale solar harvest might suggest [60, 61, 62]. These studies find substantial climatic shifts induced

by solar farms, but only when pushing photovoltaics beyond demand and localizing facilities predominantly in deserts [60, 61], where albedo effects are most potent. Climate change due to sDACCCS cover does not have to be confined to the deployment location, but could be due to atmospheric teleconnections. However, while our simulations show signs of remote climate variations (Figures S17–S18), they barely exhibit significant climate shifts in any region, making offsite consequences unlikely.

Especially if DAC-based technologies cannot meet expectations, there would still be substantial land conversions in a high-CDR world if solar energy harvest is included in the assessment, as previously suggested based on theoretical calculations [63, 19]. These results underline the importance of research efforts into land use-efficient DACCCS process chains. The efficient hE chain, for which we assumed rather conservative efficiencies (Methods) and not the most ideal sink products [14], could constitute such an approach. However, the risks of relying extensively on DAC-type process chains also become evident. For example, land conversions in central Europe which are equivalent to 18% of regional agricultural area (high-CDR world, high efficiency, localized sDACCCS) would constitute a remarkable local intervention into already pressured regions. Underwhelming technological performance could raise this toll to orders of 37%. Hence, reaching a high efficiency both for sDACCCS technology and energy supply can make the difference between an acceptable CDR burden and one exceeding limited land resources [7, 64, 25].

As a consequence of CDR deployment, our simulations reduce agricultural land use and thus emissions through grazing and crop harvest (Figure 5e-g). In some focus regions, these reduced land use emissions offset CO_2 emissions associated with deploying sDACCCS. While the decrease in agricultural land is simply a consequence of the model's land use scheme (Methods, SI), this observation highlights that more efficient food production and plant-based diets would not only decrease land use emissions, but could free up space for CDR deployment [65].

The effect of spatial deployment on global land conversion is almost negligible. However, it co-determines regional land conversions and the potential to lose land-stored carbon. Different distributions of DAC, conversion facilities, and associated energy harvest among countries could shift environmental impacts between regions. Previous studies already show how the spatial configuration of growing biomass for CDR could affect carbon stocks, land cover, and climate [66]. Thus, burden-sharing should go beyond politico-economical dimensions and climate change impacts and also account for CDR's entire environmental burden.

DAC-like technological progress is uncertain and impossible to extrapolate. Reliable real-world efficiency data is scarce, limiting the accuracy of CDR process models to first-order approximations. In addition, spatial constraints are incomplete and future CDR burden sharing is vague. Therefore, our scenario design spreads a range of uncertainty, but whether it covers future technological and political-economic development is unknown. Therefore, we interpret our simulations as storyline experiments, not predictions. As hopes for CDR grow, the storylines can provide indications whether DAC and sDACCCS could benefit the climate and environment.

Our CDR extension exclusively represents DAC-based process chains, including CO_2 conversion to a sink product, and assumes solar energy to drive the CO_2 reduction. Extending modeling capabilities to assess DAC process chains with several renewable energy sources at a time and alongside natural photosynthesis-based approaches [12] and synergies is required to guide the evaluation of CDR portfolios. For instance, our model overestimates the net loss of grasslands in temperate climates because it does not account for the fact that meadows typ-

ically fill the space between the absorbers, creating habitats for insect pollinators as a positive side effect [67]. Experiments with interactive land use scenarios could help optimizing adverse and beneficial side effects of CDR approaches in space and time. Finally, generating evidence from a model ensemble could corroborate our results.

We demonstrate that the net CO_2 removal potential of sDACCCS does not suffer substantially from reduced carbon stocks and biospheric carbon uptake due to land conversion. However, the removal potential of sDACCCS is subject to other constraints over its life cycle. Environmental consequences could arise from provisioning resources, constructing and maintaining sDACCCS installations, handling the sink product, and dismantling CDR devices, all of which require life cycle assessment [26, 68]. Other constraints not represented in Earth system models are economic costs, energy and resource demands, and the geological storage potential and resulting permanence of CO_2 storage, all of which depend on the chosen sink product [14]. Constraining them requires dedicated inventories and modeling.

Our study provides novel evidence indicating that, within the scope and limitations of our modeling approach, DAC-based process chains targeting liquid or solid products by converting the captured CO_2 cause negligible impacts on climate. Also, these sDACCCS process chains do not induce carbon emissions from the biosphere that would substantially offset their removal potential. At the same time, our results suggest that associated land conversions could lead to substantial target conflicts in a world overly reliant on CDR. In such a world, the risks for target conflicts are particularly high if technological efficiencies fall short of expectations, but persist if highly efficient carbon fixation would be available. Minimizing adverse consequences requires high technological efficiency, keeping the overall CDR need low through plausible emission reductions, and limiting excessive expectations on CDR. Therefore, reducing the reliance on yet unrealized technological advancements is vital in light of the growing evidence of all lifecycle costs of CO_2 removal.

Supplementary Material

Further information on the methods used throughout our study is available as Supplementary Information. This supplement contains comprehensive descriptions of the sDACCCS representation in MPI-ESM, model validation, scenario design, and robustness testing.

Data and Code availability

MPI-ESM is licensed under the MPI-ESM Software License Agreement, a free, non-commercial, and personalized license and can be obtained at https://code.mpimet.mpg.de/projects/mpi-esm-license. Extensions to represent sDACCCS process chains in MPI-ESM can be made available separately upon request. Code reproducing the figures of the manuscript and the supplementary material will be made available on GitHub (https://github.com/paleovar/) and, along with relevant model output, on Zenodo.

Acknowledgements

M.A. acknowledges funding from the German Federal Environmental Foundation (DBU) and the Landesgraduiertenförderung Baden–Württemberg. M.A., M.M., and K.R. acknowledge funding from the German Federal Ministry for Education and Research (BMBF), project "NETPEC" (grant no. 01LS2103A). T.K. acknowledges funding from BMBF through the Palmod project (grant no. 01LP1921A) and from the European Research Council under the European Union's Horizon 2020 programme as part of the Q-Arctic project (grant no. 951288). M.A. and K.R. acknowledge the German Climate Computing Centre (DKRZ) for providing resources and com-

pute time through the CITRONE and PalMod projects. M.A., M.M., and K.R. acknowledge the CDRterra project for providing a forum for discussions, in particular Julia Pongratz and Yiannis Moustakis for discussions around CDR modeling. The authors thank all contributors to the Max Planck Institute for Meteorology Earth system model for making their code available and accessible, and Elisa Ziegler for valuable feedback on the manuscript.

Author contributions

Conceptualizing the project: M.A., K.R.
Developing the methodology: M.A., K.R. with input from T.K. and M.M.
Developing the software: M.A. with help from T.K.
Conducting the simulations, analyzing the data, performing visualization: M.A.
Acquiring funding: K.R., M.A., M.M.
Administering the project: K.R., M.M
Writing the original draft: M.A.
Contributing to writing and editing the manuscript: all

Competing interests

The authors declare no competing interests.

Correspondence and requests for materials

should be addressed to Moritz Adam and Kira Rehfeld.

References

[1] H. D. Matthews and S. Wynes. "Current global efforts are insufficient to limit warming to 1.5°C". *Science* 376.6600 (2022), 1404–1409. DOI: 10.1126/science.abo3378.

[2] M. Pathak et al. "Technical Summary". *Climate Change 2022: Mitigation of Climate Change. Contribution of Working Group III to the Sixth Assessment Report of the Intergovernmental Panel on Climate Change*. Cambridge, UK and New York, NY, USA: Cambridge University Press, 2022. DOI: 10.1017/9781009157926.002.

[3] K. Riahi et al. "Mitigation pathways compatible with long-term goals". *Climate Change 2022: Mitigation of Climate Change. Contribution of Working Group III to the Sixth Assessment Report of the Intergovernmental Panel on Climate Change*. Ed. by P. Shukla et al. Cambridge, UK and New York, NY, USA: Cambridge University Press, 2022. DOI: 10.1017/9781009157926.005.

[4] M. Babiker et al. "Cross-sectoral Perspectives". *Climate Change 2022: Mitigation of Climate Change. Contribution of Working Group III to the Sixth Assessment Report of the Intergovernmental Panel on Climate Change*. Cambridge, UK and New York, NY, USA: Cambridge University Press, 2022. DOI: 10.1017/9781009157926.005.

[5] G. F. Nemet et al. "Negative emissions - Part 3: Innovation and upscaling". *Environmental Research Letters* 13.6 (2018), 063003. DOI: 10.1088/1748-9326/aabff4.

[6] S. Fuss et al. "Negative emissions - Part 2: Costs, potentials and side effects". *Environmental Research Letters* 13.6 (2018), 063002. DOI: 10.1088/1748-9326/aabf9f.

[7] E. F. Lambin and P. Meyfroidt. "Global land use change, economic globalization, and the looming land scarcity". *Proceedings of the National Academy of Sciences* 108.9 (2011), 3465–3472. DOI: 10.1073/pnas.1100480108.

[8] S. M. Smith et al. *The state of carbon dioxide removal*. 2023. DOI: 10.17605/osf.io/w3b4z.

[9] P. Smith et al. "Biophysical and economic limits to negative CO2 emissions". *Nature Climate Change* 6.1 (2016), 42–50. DOI: 10.1038/nclimate2870.

[10] P. Köhler, J. Hartmann, and D. A. Wolf-Gladrow. "Geoengineering potential of artificially enhanced silicate weathering of olivine". *Proceedings of the National Academy of Sciences* 107.47 (2010), 20228–20233. DOI: 10.1073/pnas.1000545107.

[11] V. Heck et al. "Biomass-based negative emissions difficult to reconcile with planetary boundaries". *Nature Climate Change* 8.2 (2018), 151–155. DOI: 10.1038/s41558-017-0064-y.

[12] T. F. Loughran et al. "Limited Mitigation Potential of Forestation Under a High Emissions Scenario: Results From Multi-Model and Single Model Ensembles". *Journal of Geophysical Research: Biogeosciences* 128.12 (2023). DOI: 10.1029/2023jg007605.

[13] N. M. Dowell et al. "The role of CO2 capture and utilization in mitigating climate change". *Nature Climate Change* 7.4 (2017), 243–249. DOI: 10.1038/nclimate3231.

[14] M. M. May and K. Rehfeld. "ESD Ideas: Photoelectrochemical carbon removal as negative emission technology". *Earth System Dynamics* 10.1 (2019), 1–7. DOI: 10.5194/esd-10-1-2019.

[15] M. M. May and K. Rehfeld. "Negative Emissions as the New Frontier of Photoelectrochemical CO2 Reduction". *Advanced Energy Materials* (2022), 2103801. DOI: 10.1002/aenm.202103801.

[16] M. Fasihi, O. Efimova, and C. Breyer. "Techno-economic assessment of CO 2 direct air capture plants". *Journal of Cleaner Production* 224 (2019), 957–980. DOI: 10.1016/j.jclepro.2019.03.086.

[17] K. S. Lackner et al. "The urgency of the development of CO2 capture from ambient air". *Proceedings of the National Academy of Sciences* 109.33 (2012), 13156–13162. DOI: 10.1073/pnas.1108765109.

[18] J. Canadell et al. "Global Carbon and other Biogeochemical Cycles and Feedbacks". *Climate Change 2021: The Physical Science Basis. Contribution of Working Group I to the Sixth Assessment Report of the Intergovernmental Panel on Climate Change*. Ed. by V. Masson-Delmotte et al. United Kingdom and New York, NY, US: Cambridge University Press, Cambridge, 2021, 673–816.

[19] J. Sekera and A. Lichtenberger. "Assessing Carbon Capture: Public Policy, Science, and Societal Need". *Biophysical Economics and Sustainability* 5.3 (2020), 14. DOI: 10.1007/s41247-020-00080-5.

[20] W. Carton et al. "Negative emissions and the long history of carbon removal". *Wiley Interdisciplinary Reviews: Climate Change* 11.6 (2020). DOI: 10.1002/wcc.671.

[21] H. J. Buck. "Should carbon removal be treated as waste management? Lessons from the cultural history of waste". *Interface Focus* 10.5 (2020), 20200010. DOI: 10.1098/rsfs.2020.0010.

[22] M. Schreier et al. "Solar conversion of CO2 to CO using Earth-abundant electrocatalysts prepared by atomic layer modification of CuO". *Nature Energy* 2.7 (2017), 17087. DOI: 10.1038/nenergy.2017.87.

[23] D. S. Goldberg et al. "Co-Location of Air Capture, Subseafloor CO2 Sequestration, and Energy Production on the Kerguelen Plateau". *Environmental Science & Technology* 47.13 (2013), 7521–7529. DOI: 10.1021/es401531y.

[24] United States National Research Council. *Climate Intervention: Carbon Dioxide Removal and Reliable Sequestration (2015)*. Washington, DC: The National Academic Press, 2015. DOI: 10.17226/18805.

[25] T. Terlouw et al. "Life Cycle Assessment of Direct Air Carbon Capture and Storage with Low-Carbon Energy Sources". *Environmental Science & Technology* 55.16 (2021), 11397–11411. DOI: 10.1021/acs.est.1c03263.

[26] S. Deutz and A. Bardow. "Life-cycle assessment of an industrial direct air capture process based on temperature–vacuum swing adsorption". *Nature Energy* 6.2 (2021), 203–213. DOI: 10.1038/s41560-020-00771-9.

[27] C. Breyer et al. "Direct Air Capture of CO2: A Key Technology for Ambitious Climate Change Mitigation". *Joule* 3.9 (2019), 2053–2057. DOI: 10.1016/j.joule.2019.08.010.

[28] K. Zickfeld et al. "Net-zero approaches must consider Earth system impacts to achieve climate goals". *Nature Climate Change* 13.12 (2023), 1298–1305. DOI: 10.1038/s41558-023-01862-7.

[29] K. Riahi et al. "The Shared Socioeconomic Pathways and their energy, land use, and greenhouse gas emissions implications: An overview". *Global Environmental Change* 42 (2017), 153–168. DOI: 10.1016/j.gloenvcha.2016.05.009.

[30] M. Meinshausen et al. "The shared socio-economic pathway (SSP) greenhouse gas concentrations and their extensions to 2500". *Geoscientific Model Development* 13.8 (2020), 3571–3605. DOI: 10.5194/gmd-13-3571-2020.

[31] C. L. Fyson et al. "Fair-share carbon dioxide removal increases major emitter responsibility". *Nature Climate Change* 10.9 (2020), 836–841. DOI: 10.1038/s41558-020-0857-2.

[32] M. A. Green et al. "Solar cell efficiency tables (Version 61)". *Progress in Photovoltaics: Research and Applications* 31.1 (2023), 3–16. DOI: 10.1002/pip.3646.

[33] M. Ozkan et al. "Current status and pillars of direct air capture technologies". *iScience* 25.4 (2022), 103990. DOI: 10.1016/j.isci.2022.103990.

[34] D. W. Keith et al. "A Process for Capturing CO2 from the Atmosphere". *Joule* 2.8 (2018), 1573–1594. DOI: 10.1016/j.joule.2018.05.006.

[35] M. Schreier et al. "Efficient photosynthesis of carbon monoxide from CO2 using perovskite photovoltaics". *Nature Communications* 6.1 (2015), 7326. DOI: 10.1038/ncomms8326.

[36] I. Melnikova et al. "Carbon Cycle Response to Temperature Overshoot Beyond 2°C: An Analysis of CMIP6 Models". *Earth's Future* 9.5 (2021), 1–19. DOI: 10.1029/2020ef001967.

[37] T. Mauritsen et al. "Developments in the MPI-M Earth System Model version 1.2 (MPI-ESM1.2) and Its Response to Increasing CO2". *Journal of Advances in Modeling Earth Systems* 11.4 (2019), 998–1038. DOI: 10.1029/2018ms001400.

[38] C. H. Reick et al. "Representation of natural and anthropogenic land cover change in MPI-ESM". *Journal of Advances in Modeling Earth Systems* 5.3 (2013), 459–482. DOI: 10.1002/jame.20022.

[39] V. Eyring et al. "Overview of the Coupled Model Intercomparison Project Phase 6 (CMIP6) experimental design and organization". *Geoscientific Model Development* 9.5 (2016), 1937–1958. DOI: 10.5194/gmd-9-1937-2016.

[40] V. K. Arora et al. "Carbon–concentration and carbon–climate feedbacks in CMIP6 models and their comparison to CMIP5 models". *Biogeosciences* 17.16 (2020), 4173–4222. DOI: 10.5194/bg-17-4173-2020.

[41] S. Rast et al. *User manual for ECHAM6*. Reports on Earth System Science / Max Planck Institute for Meteorology. Max Planck Institute for Meteorology, 2013. URL: http://hdl.handle.net/11858/00-001M-0000-0013-FCB9-8.

[42] B. Stevens et al. "Atmospheric component of the MPI-M Earth System Model: ECHAM6". *Journal of Advances in Modeling Earth Systems* 5.2 (2013), 146–172. DOI: 10.1002/jame.20015.

[43] J. H. Jungclaus et al. "Ocean Circulation and Tropical Variability in the Coupled Model ECHAM5/MPI-OM". *Journal of Climate* 19.16 (2006), 3952–3972. DOI: 10.1175/jcli3827.1.

[44] H. Paulsen et al. "Incorporating a prognostic representation of marine nitrogen fixers into the global ocean biogeochemical model HAMOCC". *Journal of Advances in Modeling Earth Systems* 9.1 (2017), 438–464. DOI: 10.1002/2016ms000737.

[45] G. C. Hurtt et al. "Harmonization of global land use change and management for the period 850–2100 (LUH2) for CMIP6". *Geoscientific Model Development* 13.11 (2020), 5425–5464. DOI: 10.5194/gmd-13-5425-2020.

[46] B. C. O'Neill et al. "The Scenario Model Intercomparison Project (ScenarioMIP) for CMIP6". *Geoscientific Model Development* 9.9 (2016), 3461–3482. DOI: 10.5194/gmd-9-3461-2016.

[47] ESMAP. *Global Photovoltaic Power Potential by Country*. 2020. URL: https://globalsolaratlas.info/global-pv-potential-study (visited on 01/27/2023).

[48] D. P. v. Vuuren et al. "Alternative pathways to the 1.5 °C target reduce the need for negative emission technologies". *Nature Climate Change* 8.5 (2018), 391–397. DOI: 10.1038/s41558-018-0119-8.

[49] G. Realmonte et al. "An inter-model assessment of the role of direct air capture in deep mitigation pathways". *Nature Communications* 10.1 (2019), 1–12. DOI: 10.1038/s41467-019-10842-5.

[50] G. P. Peters and O. Geden. "Catalysing a political shift from low to negative carbon". *Nature Climate Change* 7.9 (2017), 619–621. DOI: 10.1038/nclimate3369.

[51] N. J. v. d. Berg et al. "Implications of various effort-sharing approaches for national carbon budgets and emission pathways". *Climatic Change* 162.4 (2020), 1805–1822. DOI: 10.1007/s10584-019-02368-y.

[52] C. Breyer, M. Fasihi, and A. Aghahosseini. "Carbon dioxide direct air capture for effective climate change mitigation based on renewable electricity: a new type of energy system sector coupling". *Mitigation and Adaptation Strategies for Global Change* 25.1 (2020), 43–65. DOI: 10.1007/s11027-019-9847-y.

[53] A. Kaur et al. "Challenges in scale-up of electrochemical CO2 reduction to formate integrated with product extraction using electrodialysis". *Journal of Chemical Technology & Biotechnology* 96.9 (2021), 2461–2471. DOI: 10.1002/jctb.6812.

[54] M. Iturbide et al. "An update of IPCC climate reference regions for subcontinental analysis of climate model data: definition and aggregated datasets". *Earth System Science Data* 12.4 (2020), 2959–2970. DOI: 10.5194/essd-12-2959-2020.

[55] L. Xu et al. "Changes in global terrestrial live biomass over the 21st century". *Science Advances* 7.27 (2021), eabe9829. DOI: 10.1126/sciadv.abe9829.

[56] L. Mo et al. "Integrated global assessment of the natural forest carbon potential". *Nature* (2023), 1–10. DOI: 10.1038/s41586-023-06723-z.

[57] World Bank. *World Development Indicators (WDI)*. 2024. URL: https://datacatalog.worldbank.org/search/dataset/0037712/World-Development-Indicators (visited on 08/09/2024).

[58] Land Use, Food and Agriculture Organization of the United Nations. *FAO Land Use Indicators*. July 2023. URL: https://www.fao.org/faostat/en/%5C#data/RL (visited on 11/13/2023).

[59] K. Zickfeld et al. "Asymmetry in the climate–carbon cycle response to positive and negative CO2 emissions". *Nature Climate Change* 11.7 (2021), 613–617. DOI: 10.1038/s41558-021-01061-2.

[60] Y. Li et al. "Climate model shows large-scale wind and solar farms in the Sahara increase rain and vegetation". *Science* 361.6406 (2018), 1019–1022. DOI: 10.1126/science.aar5629.

[61] Z. Lu et al. "Impacts of Large-Scale Sahara Solar Farms on Global Climate and Vegetation Cover". *Geophysical Research Letters* 48.2 (2021), 1–10. DOI: 10.1029/2020gl090789.

[62] A. Hu et al. "Impact of solar panels on global climate". *Nature Climate Change* 6.3 (2016), 290–294. DOI: 10.1038/nclimate2843.

[63] National Academies of Sciences, Engineering, and Medicine. *Negative Emissions Technologies and Reliable Sequestration: A Research Agenda*. Washington, D.C.: The National Academies Press, 2019. DOI: 10.17226/25259. URL: https://www.nap.edu/catalog/25259.

[64] United Nations Convention to Combat Desertification. *The Global Land Outlook, second edition*. Bonn: UNCCD, 2022.

[65] M. N. Hayek et al. "The carbon opportunity cost of animal-sourced food production on land". *Nature Sustainability* 4.1 (2021), 21–24. DOI: 10.1038/s41893-020-00603-4.

[66] V. K. Arora and A. Montenegro. "Small temperature benefits provided by realistic afforestation efforts". *Nature Geoscience* 4.8 (2011), 514–518. DOI: 10.1038/ngeo1182.

[67] H. Blaydes et al. "Solar park management and design to boost bumble bee populations". *Environmental Research Letters* 17.4 (2022), 044002. DOI: 10.1088/1748-9326/ac5840.

[68] M. Z. Jacobson. "The health and climate impacts of carbon capture and direct air capture". *Energy and Environmental Science* 12.12 (2019), 3567–3574. DOI: 10.1039/c9ee02709b.

Supplementary Information to "Land conversions not climate effects are the dominant consequence of sun-driven CO_2 capture, conversion, and sequestration" by M. Adam et al.

In this Supplementary Information (SI), we describe the representation of sDACCCS in MPI-ESM step by step (Section S1) and discuss technology assumptions (Section S2), scenario design (Section S3), and model validation (Section S4). Furthermore, we include figures supplementing the results of the main manuscript (Figures S9–S32).

List of Tables

List of Figures

S1 Details of the sDACCCS representation in MPI-ESM

CDR land cover on vegetated and bare land

JSBACH sub-divides every grid cell into tiles (see references Reick et al. [67] and Reick et al. [68] for any details on JSBACH). Each tile is associated with a type of land cover, with changing tile (cover) fractions resulting from natural or anthropogenic land cover change. Supported cover types include different plant functional types (PFTs), unvegetated (bare) land, and glaciers, assuming a well-mixed domain within the grid cell [67]. To represent sDACCCS land cover on the vegetated fraction of land, we expand the lookup table defining every land cover type's parameters and introduce a new land cover class. This class allows to exclude sDACCCS from calculations dedicated to vegetation and to compute CDR-specific processes exclusively on the sDACCCS tile. On unvegetated land, the pre-existing version of JSBACH cannot separate bare soil into different tiles, as it does for vegetated land. However, one could deploy sDACCCS on bare land where plants cannot grow because bioclimatic conditions exceed their capabilities. As an additional complication, JSBACH implicitly accounts for bare land when computing land surface properties like albedo for the vegetated land fraction. To accommodate these constraints within our modeling goals, we represent sDACCCS implicitly on the bare fraction. With this extension of JSBACH's tiling concept, the overall sDACCCS land cover fraction in a grid cell, f_{CDR}, consists of the cover fractions c^{v}_{CDR} on vegetated land and c^{b}_{CDR} on bare land

$$f_{\mathrm{CDR}} = c^{v}_{\mathrm{CDR}}\, f_{v,\mathrm{max}} + c^{b}_{\mathrm{CDR}}\, f_{b} \tag{21}$$

Here, $f_b = 1 - f_{v,\mathrm{max}}$ denotes the fraction of bare land, and $f_{v,\mathrm{max}}$ the potential vegetation extent.

sDACCCS land cover class

We implement the sDACCCS land cover class (Figure S1i-ii) with masks ι^{k} building on JSBACH's land cover lookup table. These masks help to separate processes taking place on CDR tiles and on vegetation tiles ($\iota^{v \vee \mathrm{CDR}}$) from those exclusively involving sDACCCS (ι^{CDR}) or vegetation tiles (ι^{v}). Based on the ι^{k}, we exclude sDACCCS chains from processes like carbon allocation through photosynthesis, vegetation dynamics, dynamic phenology, and disturbances. Calculations involving both vegetation and CDR tiles include (bio-)physical surface properties, radiative balances, soil hydrology, and land use transitions. Processes exclusive to sDACCCS CDR cover are the CO_2 withdrawal through (photo-)electrochemical reduction, fill-up of the sink product pool, and coupling of the CDR cover to the spatiotemporal target.

Land surface properties

Through solar energy harvest and CO_2 capturing facilities, large-scale sDACCCS would alter the surface albedo and the surface roughness lengths. Changes in these properties can modify the absorption of shortwave radiation, the back-scattering of short- and longwave radiation, and the transport of heat and momentum through the atmospheric boundary layer. In this study, we assume an effective albedo of 0.27 for sDACCCS tiles, similar to previous studies

on the climatic effects of photovoltaics within general circulation models [69]. As roughness lengths we assume 1m, the same as JSBACH does for tropical deciduous and extra-tropical trees. This assumption is motivated by the expected size of DAC facilities and large-scale solar parks.

sDACCCS land cover could be deployed both on vegetated and bare land. However, JSBACH's tiling scheme [68, 67] focusses on resolving different surface types on the vegetated fraction of land. Therefore, treating the bare land's properties implicitly in many computations is handy in the default model, while it complicates representing sDACCCS as an additional surface cover on unvegetated land. To still account for CDR on unvegetated land implicitly, we modify JSBACH's albedo and roughness schemes to account for the implicit sDACCCS cover on the bare fraction of land. This approach allows to represent CO_2 withdrawal on bare land, land use through sDACCCS, and impacts of CDR on the surface energy balance (Figure S1). At the same time, we can keep JSBACH's default schemes, for example, for vegetation dynamics. However, bare land neither contains a soil model nor soil carbon stocks. Thus, CDR land use transitions only impact existing carbon stocks on the vegetated fraction of a grid cell.

Surface albedo

For each tile, JSBACH distinguishes between cover area and vegetation canopy area [67]. The canopy fraction can be smaller than or equal to the tile cover fraction. Without changing the tile fraction, this approach allows handling dynamically changing leaf area and the subsequent effect of exposing bare soil on the tiles' albedo. For CDR cover, we assume that (i) sDACCCS on bare soil does not get exposed through canopy gaps, (ii) sDACCCS cover is not subject to canopy gaps that are not already covered by its effective albedo (iii) the turnover of soil organic matter does not change the soil albedo on sDACCCS-covered land, (iv) tree stems do not affect the albedo of sDACCCS, and (v) sDACCCS does not impact the other tiles' surface properties.

JSBACH represents gaps in the canopy which expose bare soil on the vegetated fraction of land (Figure S2) with the "sky view factor" [68] κ_k, $k \in K = \{\mathsf{LCT}_i \,|\, \iota_i^{\upsilon} = \mathsf{TRUE} \vee \iota_i^{\mathrm{CDR}} = \mathsf{TRUE}\}$, $i = 1, 2, \ldots, N_{\mathsf{LCT}}$. For vegetation, κ_k is a function of the dynamic leaf area index Λ_k [68]. Respecting (i), κ_k differs between vegetation and CDR cover

$$\kappa_k = \begin{cases} 1 - f_{\upsilon}, & \iota_k^{\mathrm{CDR}} = \mathsf{TRUE} \\ 1 - \left[f_{\upsilon} \cdot (1 - e^{-\Lambda_k/2}) \right], & \text{else} \end{cases} \tag{22}$$

where f_{υ} is the potentially vegetated cover fraction and we assume $\iota^{\upsilon \vee \mathrm{CDR}} = \mathsf{TRUE}$ here in the first place. JSBACH's sky view factor that includes the shading effect of tree stems for forest vegetation [68], $\kappa_{\mathsf{stem},k}$, remains untouched, following (iii) and (iv)

$$\kappa_{\mathsf{stem},k} = \kappa - \left[1 - f_{\upsilon} \cdot (1 - e^{-1/2 (\Lambda_k + \Xi_k)}) \right] \tag{23}$$

To now account for the implicit CDR cover on bare land, we split the contributions of sDACCCS on bare soil from the remaining bare land whose exposed fraction increases through canopy gaps. Thus, the "background albedo", a tile's albedo prior to considering snow cover and tree stems, is

$$\alpha_k^{bg} = \begin{cases} (1 - \kappa_k)\, \alpha_{c,k} + (\kappa_k - f_{\mathrm{CDR}}^b)\, \alpha_{\mathrm{soil}}, & \iota_k^F = \mathsf{TRUE} \\ (1 - \kappa_k)\, \alpha_{c,k} + (\kappa_k - f_{\mathrm{CDR}}^b)\, \alpha_{\mathrm{soil}} & \\ \qquad + \alpha_{\mathrm{CDR}} \cdot f_{\mathrm{CDR}}^b, & \text{else} \end{cases} \tag{24}$$

Here, $\alpha_{c,k}$ denotes the canopy albedo of a land cover type's effective CDR albedo, α_{soil} the albedo of unvegetated land, and ι_k^F the mask for forest PFTs. Other than in JSBACH's default

scheme, α_k^{bg} distinguishes between forested land and non-forest cover. This design choice simplifies applying (iv). Incorporating snow cover on the vegetation canopy and on sDACCCS, as well as tree stems results in the albedo α_k for tile k on the vegetated fraction of land (Figure S2)

$$\alpha_k = \begin{cases} \max\Big[(\kappa_k - \kappa_{\text{stem},k} - f^b_{\text{CDR}})(c_{\text{sn}}\alpha_{\text{sn}} + (1-c_{\text{sn}})\,\alpha_{\text{soil}}) \\ \qquad + \kappa_{\text{stem},k}\left(c_{\text{snc}}\alpha_{\text{snc}} + (1-c_{\text{sn}})\,\alpha_{\text{soil}}\right) \\ \qquad + (1-\kappa_k)\big(c_{\text{snc}}\alpha_{\text{snc}} + (1-c_{\text{snc}})\,\alpha_k^{bg}\big),\ \alpha_k^{bg}\Big] & \iota_k^F = \text{TRUE} \\ \qquad + f^b_{\text{CDR}}\left(c_{\text{sn}}\alpha_{\text{sn}} + (1-c_{\text{sn}})\,\alpha_{\text{CDR}}\right), \\ \max\Big[c_{\text{sn}}\alpha_{\text{snc}} + (1-c_{\text{sn}})\,\alpha_k^{bg},\ \alpha_k^{bg}\Big], & \text{else} \end{cases} \tag{25}$$

In Equation (25), α_{sn} and α_{snc} denote the snow albedo on ground and on the canopy, c_{sn} and c_{snc} are the respective cover fractions. Again, (i) and (iv) result in separate terms for the contributions of sDACCCS on the fraction of bare land and on exposed soil itself. Equations (24) and (25) incorporate the unvegetated land into the albedo of vegetated tiles. Then, as in the default model [68], the aggregated albedo of a land grid box is

$$\alpha = \sum_{k \in K} c_k \alpha_k \tag{26}$$

Surface roughness

In JSBACH, contributions of the surface type $z_{0_m}^{\text{surf}}$ and the underlying orography $z_{0_m}^{\text{oro}}$ make up the effective roughness length for the turbulent transport of momentum [68] z_{0_m}

$$z_{0_m} = \sqrt{(z_{0_m}^{\text{surf}})^2 + (z_{0_m}^{\text{oro}})^2} \tag{27}$$

The turbulent heat transport only depends on the surface roughness of the land cover, $z_{0_h}^{\text{surf}}$. In both cases, the parameters for the surface roughness lengths have to be aggregated from the tile level to the grid cell resolution. JSBACH employs the concept of a blending height [70] to achieve this downscaling [68]. The reasoning behind this concept is that surface heat and momentum fluxes originating from multiple surface types cannot be distinguished above a certain blending height l_b. Similar to the albedo calculations, JSBACH handles bare soil implicitly when computing a grid cell's roughness length. We expand this approach for the implicit sDACCCS fraction on unvegetated land. The effective bare fraction f_{b_j} on a vegetated tile j and the effective fraction of implicit CDR that is deployed on bare soil f_{CDR_j} are

$$\begin{aligned} f_{b_j} &= (1 - f_v) \cdot c_j \cdot (1 - c^b_{\text{CDR}}) \\ f_{\text{CDR}_j} &= (1 - f_v) \cdot c_j \cdot c^b_{\text{CDR}} \end{aligned} \tag{28}$$

where the prefactor $1 - f_v$ spreads the implicit bare and sDACCCS-covered land fraction across all vegetated tiles, assuming a well-mixed domain [67]. c^b_{CDR} again denotes the fraction of sDACCCS cover on bare land and c_j the cover fraction of the respective tile j. Then, we can treat f_{b_j} and f_{CDR_j} separately when aggregating the surface roughness with the blending height approach. The roughness length for heat transport follows as [68, 70]

$$z_{0_h}^{\text{surf}} = l_b \exp\left\{ -\left(\sum_{j=1}^{N^v_{tiles}} \sum_{i \in \{j, b_j, \text{CDR}_j\}} \sum_{\{\text{sn, nsn}\}} \frac{f_i}{\left(\ln\left({}^{l_b}/_{z^j_{0_h}}\right)\right)^2} \right)^{-1/2} \right\} \tag{29}$$

with grid cell cover fractions f_i and blending height $l_b = 100\,\text{m}$. The sum over {sn, nsn} symbolizes that the surface roughness for heat transport changes if snow covers a surface (sn) compared to when it does not (nsn). An analogous calculation yields the roughness length for turbulent momentum transport. For $z_{0_m}^{\text{surf}}$, the only difference lies in the fact that JSBACH does not differentiate between snow-covered and snow-free surfaces [68].

CDR land cover dynamics

Two stages make up our CDR deployment scheme. First, we translate the global SSP-based CDR target into a spatially explicit target change of fractional sDACCCS area (Figure S3). Subsequently, we integrate these anticipated area changes into JSBACH's land use transition scheme. The transition scheme combines a set of priority rules for land conversion with a series of transition matrices converting between cover types. It resolves land use change including cyclic ("secondary") transitions at annual time scale and interpolates them linearly onto a daily resolution.

First stage – Converting spatiotemporal targets into anticipated changes in sDACCCS

We initially determine the globally integrated mismatch between the cumulated CDR target $\tilde{T}$ and cumulative simulated withdrawal through sDACCCS, $\tilde{W}$ (Figure S3). With a second-order Taylor expansion of this mismatch, we incorporate offsets from internal variability over time while smoothly changing sDACCCS cover a smooth effective forcing. The condition is supposed to hold after sDACCCS has been deployed over the course of year i while the computation takes place at the beginning of it, i.e. at the end of year $i-1$.

$$\begin{aligned} 0 &\stackrel{!}{=} T(t) - W(t) \\ &= T_i - W_i + \partial_t T|_i - \partial_t W|_i + \frac{\partial_t^2 T|_i - \partial_t^2 W|_i}{2} + \sigma(\Delta t^3) \end{aligned} \tag{30}$$

To solve Equation (30) for the residual CDR deployment, denoted Δ_i, we reformulate it in terms of the annual target removal rates T_i and actual (simulated) rates W_i. To account for the linear interpolation of land cover changes over a year [68] which leads to a systematic lag of the W_i behind the T_i, we further introduce target removal rates $T^*_{i-1/2}$ that lag the T_i by half a year. Based on the $T^*_{i-1/2}$, we can eventually avoid a systematic bias in Equation (30). With these adjustements, the cumulative removal is

$$\tilde{T}_i = \sum_{j \le i} T_j = \tilde{T}^*_{i-1/2} + \frac{T^*_{i+1/2} + T^*_{i-1/2}}{2} \tag{31}$$

with cumulative target removal at the middle of the previous simulation year $\tilde{T}^*_{i-1/2} = \sum_{j \le i-1/2} T^*_j$. The second term in Equation (31) reflects the linear interpolation of land cover changes. Similarly, we obtain an expression for the first derivative

$$\partial_t \tilde{T}|_i = T_i = \frac{T^*_{i+1/2} + T^*_{i+1/2}}{2} \tag{32}$$

and the second derivative

$$\partial_t^2 \tilde{T}|_i = \tilde{T}^*_{i+1} - 2\tilde{T}^*_i + \tilde{T}^*_i \tag{33}$$

Inserting the definition (31) into Equation (33) yields an expression that is independent of the subsequent cumulative target

$$\partial_t^2 \tilde{T}|_i = \frac{1}{2}(T^*_{i+3/2} + T^*_{i+1/2} - 3T^*_{i-3/2} + T^*_{i-3/2}) \tag{34}$$

Then, the expressions (31)-(34) can all be computed from the global CDR scenario. For the realized, piece-wise linear cumulative CDR, we obtain

$$\tilde{W}_i = \sum_{j \le i} W_j \tag{35}$$

Its first derivate can be expressed as a the sum of last year's CO_2 removal and the residual sDACCCS deployment

$$\partial_t \tilde{W} = W_i = W_{i-1} + \Delta_i \tag{36}$$

and the second derivative can be discretized analogously to Equation (33)

$$\partial_t^2 \tilde{W} = \tilde{W}_{i+1} - 2\tilde{W}_i + \tilde{W}_{i-1} \simeq \tilde{T}_{i+1} - 2\tilde{W}_i + \tilde{W}_{i-1} \tag{37}$$

where we assume $\tilde{W}_{i+1} \to \tilde{T}_{i+1}$. Solving for Δ_i yields an expression

$$\Delta_i = \Delta_i\Big(\tilde{T}_i, \partial_t \tilde{T}_i(T^*_{i+1/2}, T^*_{i-1/2}), \partial_t^2 \tilde{T}_i(T^*_{i+3/2}, T^*_{i+1/2}, T^*_{i-1/2}, T^*_{i-3/2}), \tilde{W}_i, \partial_t^2 \tilde{W}_i(\tilde{W}_{i+1}, \tilde{W}_i, \tilde{W}_{i-1})\Big) \tag{38}$$

To improve numerical stability, we test different linearization coefficients for the different orders in (38) and eventually draw on 1/2 for the zeroth and first order term, and 1 for the second order term. Thus, we emphasize smoothness of the CDR pathway. For many parts of the deployment scheme it is irrelevant if $\Delta >= 0$ or $\Delta < 0$ (index dropped in the following). Therefore, the scheme's steps apply to both cases, CDR establishment and dismantling, if not stated otherwise.

The withdrawal potential ψ_{ij} of every grid cell $(i,\ j) \in \{(1,\ 1), (1,\ 2), \dots, (n_{\text{lon}},\ n_{\text{lat}})\}$ translates the spatiotemporal sDACCCS target into anticipated changes of sDACCCS land cover (Figure S3). However, the target change in CDR Δ_i is an extensive quantity. Thus, ψ_{ij} has to be scaled by the corresponding maximum CDR cover fraction to obtain the CDR in relation to changes in the cover fraction. The maximum CDR cover is $f_{\text{max}} - f_\epsilon$ with the technical lower limit to the grid cell cover fraction f_ϵ [68]. Therefore, the relative potential withdrawal ψ^r_{ij} is

$$\psi^r_{ij} = \frac{\psi_{ij}}{f_{\text{max}} - f_\epsilon} \tag{39}$$

Correcting for natural land cover dynamics δ (see below), the anticipated change in sDACCCS grid cell fraction is

$$\Delta\widetilde{f}_{ij} = \frac{(\Delta + \delta) \cdot w^c_{ij}}{\psi^r_{ij}} \tag{40}$$

As the concluding step of the first stage of sDACCCS deployment (Figure S3), we iteratively spread the CDR deployment $\Delta_r = \Delta_i + \delta$ across all cells that are (i) involved in the deployment process in the sense of a contribution weight $w^c_{ij} > 0$ (see below), (ii) can support a growing (decreasing) CDR fraction because they have not reached the upper (lower) CDR fraction limit up to the current year, and (iii) have not reached the upper (lower) CDR limit in a previous step of the current iteration. The result of the iteration is the realizable fractional change in sDACCCS cover Δf_{ij} and also covers numerical inaccuracies that occur from normalizations. The realized change can only be determined following the natural and anthropogenic land cover dynamics.

The iteration takes place as long as $\Delta_r > \delta_{\text{tol}}$ and the criterion $n_{\text{iter}} < n_{\text{iter, max}}$ for a finite loop is fulfilled. Here δ_{tol} is a tolerance parameter, $n_{\text{iter, max}}$ denotes the maximum number permitted iterations, and n_{iter} is the iteration counter. At the start of the iteration, the globally realizable CDR target $\Delta_{\text{iter}} = 0$. Drawing on (13), (i)-(iii) translate into

$$\begin{aligned} \Delta f_{ij} &= \min\left[\Delta f + \frac{\Delta_r \cdot w^c_{ij}}{\psi^r_{ij}},\ \Delta f^{\text{max}}_{ij}\right] \\ &\forall\,(i,\ j) \in \{(1,\ 1),\ (1,\ 2),\ \dots,\ (n_{\text{lon}},\ n_{\text{lon}}) \mid \Delta f_{ij} < \Delta f^{\text{max}}_{ij}\} \end{aligned} \tag{41}$$

in the iteration step. To guarantee $W_i \geq 0$ and $\tilde{W}_i \geq 0$, the maximum change in sDACCCS cover fraction $\Delta f_{ij}^{\max}$ depends on the sign of the global change in CDR deployment

$$\Delta f_{ij}^{\max} = \begin{cases} \max\left[f_{ij}^{\max} - f_{ij},\, 0\right], & \Delta_r > 0 \\ \max\left[f_{ij} - f_{\epsilon},\, 0\right], & \text{else} \end{cases} \tag{42}$$

The $f_{ij}^{\max}$ account for additional land availability constraints due to inaccessible terrain, freshwater cover, nature conservation, and settlements (Section S3). After each iteration step, the remaining CDR change gets updated as

$$\Delta_{\text{iter}} = \sum_{i=1}^{n_{\text{lon}}} \sum_{j=1}^{n_{\text{lat}}} \Delta f_{ij} \cdot \psi_{ij}^{r} \tag{43}$$

Consequentially,

$$\Delta_r = \Delta + \delta - \Delta_{\text{iter}} \tag{44}$$

following each iteration step. Note that ψ_{ij}^{r} (Equation (39)) does not have to be updated in the iteration as $f^{\max}$ and f_{ϵ} are fixed parameters. The model component handles the technical case $f_{ij} < f_{\epsilon}$ implicitly as changes in cover fractions only take place on CDR tiles with $f_{ij} \geq f_{\epsilon}$. This condition implies that sDACCCS deployment and potential destruction can only ever happen on a grid cell if that cell gets initialized with $\iota_{ij}^{\text{CDR}} = \text{TRUE}$.

While being spatially explicit and flexible to forward and backward conversions of land area to sDACCCS cover, this deployment scheme cannot compensate transient contribution weights that start out as $w_{ij}^{c} \neq 0$ and turn zero over time. The scheme will only remove the formerly installed sDACCCS cover from a cell when the $w_{ij}^{c} \neq 0$, as is evident from Equation (41). This behaviour can cause inconsistency with the contribution map. The issue is, however, only relevant if one wants to prescribe that CDR is not deployed anymore in a specific area where this was possible before, which is not the case in our study.

Second stage – determining contributions of vegetated and unvegetated land to sDACCCS cover

We translate every grid cell's anticipated change in sDACCCS cover fraction into land use transitions. On the vegetated fraction of land, this is realized through JSBACH's transition scheme. For bare land, we directly compute the new implicit CDR fraction from the anticipated change in cover fraction in Equation (40). We determine contributions of the vegetated and unvegetated land cover to sDACCCS cover, assuming that neither bare nor vegetated land is preferred for sDACCCS deployment. Formally, this assumption results in relatively equal contributions of the vegetated and bare land fraction, represented in the conditions

$$c_{\text{CDR}}^{v} \overset{!}{=} c_{\text{CDR}}^{b} \Leftrightarrow \frac{f_{\text{CDR}}^{v}}{f^{v}} \overset{!}{=} \frac{f_{\text{CDR}}^{b}}{1 - f^{v}} \tag{45}$$

Here, f^{v} is the vegetated fraction, c_{CDR}^{b} and c_{CDR}^{v} are the cover fractions of sDACCCS on bare and vegetated land, and f_{CDR}^{b} and f_{CDR}^{v} denote the respective grid cell cover fractions of the two contributions. Without dynamic vegetation, sDACCCS cover fractions on vegetated and bare land would directly result from (14)

$$\Delta c^{v} = \Delta f \quad \text{and} \quad \Delta c^{b} = \Delta f \tag{46}$$

This simple conversion from a change in grid cell fraction to a change in tile cover fraction is valid because

$$\Delta f = \Delta f^{v} + \Delta f^{b} = f^{v} \Delta c^{v} + (1 - f^{v})\, \Delta c^{b} = f^{v} \Delta f + (1 - f^{v})\, \Delta f \tag{47}$$

However, as f^v changes with shifting bioclimatic conditions [68], changes in sDACCCS cover at the same time cause a small but accumulating systematic imbalance between c^b_{CDR} and c^v_{CDR} (Figure S4). In addition, land use transitions can be partially unfulfilled due to the priority rules (see below), the conservation criterion of transition matrix elements [68], and numerical inaccuracies, causing imbalances between c^b_{CDR} and c^v_{CDR}. To prevent inconsistent CO_2 withdrawal *within* the year of occurring imbalances, we adjust the fraction of sDACCCS on bare land. This corrects the CO_2 withdrawal for an expanding/shrinking vegetated fraction but cannot respect condition (14). This is because JSBACH reads and computes agricultural land use transitions ahead of shifts in natural vegetation extent, which also fixes the timing of sDACCCS cover change. Then, at the beginning of the subsequent year(s), we correct *past* imbalances between sDACCCS cover on vegetated and bare land by adjusting anticipated cover changes. Drawing on Figure S4, the necessary adjustment to maintain the anticipated sDACCCS cover within the year of imbalances is

$$\Delta f^b_{\mathsf{des}} = (c^b_{\mathsf{CDR}} - c^v_{\mathsf{CDR}}) \cdot \Delta f^v \tag{48}$$

which adds to (15). Here, $\Delta f^v = f^v_i - f^v_{i-1}$ is the shift in vegetation extent from the previous year $i-1$ to i.

To re-adjust previous relatively unequal contributions between vegetated and bare land, the model adds (removes) a relatively higher share of sDACCCS on the under-represented (over-represented) land type while sDACCCS cover is increasing (shrinking) in three steps. First, we diagnose the imbalance between the relative cover fractions on vegetated and bare land as

$$\nu = \frac{1}{2} - \frac{c^b_{\mathsf{CDR}}}{c^b_{\mathsf{CDR}} + c^v_{\mathsf{CDR}}} \tag{49}$$

This term is zero for no mismatch in the relative cover fractions, positive for $c^b_{\mathsf{CDR}} < c^v_{\mathsf{CDR}}$, and negative for $c^b_{\mathsf{CDR}} > c^v_{\mathsf{CDR}}$. The point of view chosen here is that of the sDACCCS cover on bare land. Note, however, that

$$-\nu = \frac{1}{2} - \frac{c^v_{\mathsf{CDR}}}{c^b_{\mathsf{CDR}} + c^v_{\mathsf{CDR}}} \tag{50}$$

Thus, it is irrelevant if ν is defined in terms of the relative imbalance of c^b_{CDR} or c^v_{CDR}. The imbalance between sDACCCS cover fractions translates into fractional mismatches covered area on bare and vegetated land

$$\nu^f_b = \nu \cdot (c^b_{\mathsf{CDR}} + c^v_{\mathsf{CDR}}) \cdot (1 - f_{v,\mathsf{max}}) \tag{51}$$

$$\nu^f_v = -\nu \cdot (c^b_{\mathsf{CDR}} + c^v_{\mathsf{CDR}}) \cdot f_{v,\mathsf{max}} \tag{52}$$

In a second step, the anticipated change in sDACCCS area Δf (Equation (41)) can be corrected for these mismatches. To achieve this correction, compare each grid cell's ν^f_b and ν^f_v with the anticipated land use transitions. One can capture the compensation in these balancing terms:

Case 1: On grid cells with growing sDACCCS area ($\Delta f > 0$) grow the area more on the relatively under-represented surface type:

$$\Delta f_{b,\mathsf{bal}} = \begin{cases} \min\left[f^b_{\mathsf{CDR,max}} - f^b_{\mathsf{CDR}},\ \min\left[\Delta f, \nu^f_b\right]\right], & \nu > 0 \\ 0, & \text{else} \end{cases} \tag{53}$$

$$\Delta f_{v,\mathsf{bal}} = \begin{cases} \min\left[f^v_{\mathsf{CDR,max}} - f^v_{\mathsf{CDR}},\ \min\left[\Delta f, \nu^f_v\right]\right], & \nu < 0 \\ 0, & \text{else} \end{cases} \tag{54}$$

Case 2: On grid cells with shrinking sDACCCS area ($\Delta f < 0$), shrink the area more on the relatively over-represented surface type:

$$\Delta f_{b,\mathsf{bal}} = \begin{cases} \max\left[\Delta f, \nu_b^f\right], & \nu < 0 \\ 0, & \text{else} \end{cases} \tag{55}$$

$$\Delta f_{v,\mathsf{bal}} = \begin{cases} \max\left[\Delta f, \nu_v^f\right], & \nu > 0 \\ 0, & \text{else} \end{cases} \tag{56}$$

Here, the limits guarantee that (i) the balancing does not exceed the actual fractional sDACCCS cover change that is supposed to be realized within the current year (applies to forward and backward transitions) and (ii) that it does not exceed growth limits (forward transitions only). The lower bound for backward transitions is already included in the definition of Δf (see Equation (41)). Compensating the mismatches ν_b^f and ν_v^f thus only takes place if the sDACCCS area changes in the current annual step of land use transitions. If the sDACCCS area is constant for several years, no re-balancing between sDACCCS on vegetated and bare land will take place, avoiding repeated secondary transitions for CDR deployment. Here we assume that CDR facilities would not be relocated for re-balancing.

Finally, after accounting for the imbalance between vegetated and bare land, the sDACCCS deployment that remains to take place at relatively equal fractions on both land types is

$$\Delta f_{res} = \Delta f - \Delta f_{v,\mathsf{bal}} - \Delta f_{b,\mathsf{bal}} \tag{57}$$

Based on definitions (53) to (56), at most one of $\Delta f_{v,\mathsf{bal}}$ and $\Delta f_{b,\mathsf{bal}}$ is non-zero in a grid cell. Thus, the changes in cover fraction which have to be realized on bare and vegetated land, Δc^b and Δc^v are,

Case 1: Forward transition:

$$\Delta c^b = \min\left[f^b_{\mathsf{CDR},\,\max} - f^b_{\mathsf{CDR}},\ \Delta f_{res} + \Delta f_{b,\mathsf{bal}}\right] \cdot \frac{1}{1 - f_v} \tag{58}$$

$$\Delta c^v = \min\left[f^v_{\mathsf{CDR},\,\max} - f^v_{\mathsf{CDR}},\ \Delta f_{res} + \Delta f_{v,\mathsf{bal}}\right] \cdot \frac{1}{f_v} \tag{59}$$

Case 2: Backward transition:

$$\Delta c^b = \frac{\Delta f_{res} + \Delta f_{b,\mathsf{bal}}}{1 - f_v} \tag{60}$$

$$\Delta c^v = -1 \cdot \frac{\Delta f_{res} + \Delta f_{v,\mathsf{bal}}}{f_v} \tag{61}$$

The negative sign in Equation (61) reflects that entries in the transition matrices are always positive.

Second stage – translating anticipated changes in sDACCCS cover into land use transitions

On bare land, Δc^b directly translates into an updated implicit sDACCCS cover fraction on a daily time scale

$$c^b_{\mathsf{CDR},\,d+1} = \max\left[\min\left[c^b_{\mathsf{CDR},\,d} + \Delta c_b^{(d)},\ c^b_{\mathsf{CDR},\,\max}\right],\ c_\epsilon\right] \tag{62}$$

where $\Delta c_b^{(d)}$ is the linearly interpolated daily change in CDR cover fraction and the index d refers to the daily stepping. The purpose of the minimum cover fraction $c_\epsilon \ll 0$ and the limits employed in Equation (62) is a measure of JSBACH to ensure numerical stability.

On vegetated land, the deployment scheme takes two more steps to integrate into JSBACH's transition scheme [67, 68]. First, we determine anticipated transition matrix elements $T^{k \triangleright \mathsf{CDR}}$ from other land cover types k to sDACCCS cover and elements $T^{\mathsf{CDR} \triangleright k}$ for the opposite case. Exploiting the area conservation for all land cover types k, l, $\sum_{kl} T_{kl} = 1$, the anticipated matrix elements are

Case 1: Forward transition:

$$T^{k \triangleright \mathsf{CDR}} = \min\left[\Delta c^{\upsilon} \cdot {}^{f_k^{\upsilon}}/_{f_{\upsilon}}, 1 - \sum\nolimits_{k \neq l,\, \iota_l^{\mathsf{CDR}} = \mathsf{FALSE}} T^{k \triangleright l}\right] \tag{63}$$

$$T^{\mathsf{CDR} \triangleright k} = 0 \tag{64}$$

Case 2: Backward transition:

$$T^{\mathsf{CDR} \triangleright k} = \Delta c^{\upsilon} \cdot {}^{f_k^{\upsilon}}/_{f_{\upsilon}} \tag{65}$$

$$T^{k \triangleright \mathsf{CDR}} = 0 \tag{66}$$

The mask ι_l^{CDR} excludes CDR land cover from the summation in Equation (68). With this summation, we prioritize land use transitions of the agricultural land use scenario over CDR deployment.Following Reick et al. [68]'s line of argument and their notation, we determine the realisable annual transition matrix elements $T^{k \triangleright l}$ from the potential ones $\widetilde{T}^{k \triangleright l}$. Here, the $k, l \in \{\mathsf{LCT}_{\mathsf{veg}}\}$ denote the land cover types. The notation $k \triangleright l$ represents the matrix element converting from type k to l. For agricultural land use the $\widetilde{T}^{k \triangleright l}$ stem from a pre-defined protocol [67, 68, 71]. However, the sDACCCS cover couples dynamically to a CDR target and the climatological state of irradiation. Thus, the $\widetilde{T}^{k \triangleright l}$ with $\iota_k^{\mathsf{CDR}} = \mathsf{TRUE} \vee \iota_l^{\mathsf{CDR}} = \mathsf{TRUE}$ have to be computed annually, at the step of JSBACH's land cover change.

Exploiting the area conservation [68] $\sum_{ij} T_{ij} = 1$, the realisable transition elements $T^{k \triangleright l}$ for forward transitions are

Case 1: Forward transition:

$$\widetilde{T}^{k \triangleright \mathsf{CDR}} = \Delta c^{\upsilon} \cdot {}^{f_k^{\upsilon}}/_{f_{\upsilon}} \tag{67}$$

$$T^{k \triangleright \mathsf{CDR}} = \min\left[\widetilde{T}^{k \triangleright \mathsf{CDR}}, 1 - \sum\nolimits_{k \neq l,\, \iota_l^{\mathsf{CDR}} = \mathsf{FALSE}} T^{k \triangleright l}\right] \tag{68}$$

$$T^{\mathsf{CDR} \triangleright k} = 0 \tag{69}$$

where Equation (68) gives priority to agricultural land use transitions. The backward transitions, do not require such limits on the sDACCCS cover to prioritize the agricultural land use protocol. Therefore, the matrix elements converting from CDR-covered to other land are

Case 2: Backward transition:

$$T^{\mathsf{CDR} \triangleright k} = \widetilde{T}^{\mathsf{CDR} \triangleright k} = \Delta c^{\upsilon} \cdot {}^{f_k^{\upsilon}}/_{f_{\upsilon}} \tag{70}$$

$$T^{k \triangleright \mathsf{CDR}} = 0 \tag{71}$$

Second stage – priority rules

As the final step, we expand JSBACH's prioritization rules 1–3 for land use transitions [67, 68]. These rules determine in which order natural land gets converted into agricultural land and vice versa. Again prioritizing the agricultural land use scenario, we add *rule 4* converting natural lands to sDACCCS cover and *rule 0* for the back-conversion. Here, natural lands consist of contributions by forests (F) and grasslands (G), agricultural lands comprise pastures (P) and croplands (C).

Rule 4: $F{+}G \longrightarrow \mathsf{CDR}$ (forward transition, shrinkage of natural lands for sDACCCS)
To establish CDR land cover, convert the remainder of *G* and *F* land *after* expanding agricultural lands based on *rules 1* to *3* at equal proportion.

Rule 0: $\mathsf{CDR} \longrightarrow F + G$ (backward transition, shrinkage of sDACCCS cover)
Convert CDR-used land into F and G land based on their relative abundance while respecting their potential natural extent.

In addition to *rules 4* and *0*, we amend the existing *rules 1* to *3* because reducing CDR cover for the benefit of natural land fills up a fraction of their potential natural extent. This share of potential extent cannot be used for re-converting agricultural lands back into natural ones, analogous to shrinking different types of agricultural lands as implemented by Reick et al. [68]. We derive the formal expressions implementing the new priority rules and the amendments to existing rules in the following. The amended rules culminate in daily transition matrix elements that are applied to every tile of every land cover class.

Analogous to (10.14) – (10.18) of Reick et al. [68], our CDR model implements priority *rule 4* with a scaling factor ρ. It scales $T_{N \triangleright \mathsf{CDR}}$ in relation to the remaining natural land cover fraction after *rules 1* to *3* have been applied

$$\rho = T_{N \triangleright \mathsf{CDR}} \cdot c_N \cdot [c_N - \Delta_{G \triangleright P} - \Delta_{F \triangleright P} - \Delta_{G \triangleright C} - \Delta_{F \triangleright C}]^{-1} \tag{72}$$

Here, the $\Delta_{K \triangleright L}$, $K \in \{G, F\}$, $L \in \{P, C\}$ stand for the shares in natural vegetation cover which have already been converted to agricultural lands in the current step. Then, *rule 4* comes down to

$$\begin{aligned} T_{G \triangleright \mathsf{CDR}} &= \rho \cdot (1 - T_{G \triangleright P} - T_{G \triangleright C}) \\ T_{F \triangleright \mathsf{CDR}} &= \rho \cdot (1 - T_{F \triangleright P} - T_{F \triangleright C}) \end{aligned} \tag{73}$$

The calculations materializing *Rule 0* follow the line of arguments set out by Reick et al. [68] on *rule 1* for shrinking agricultural lands. The conversion from sDACCCS cover to F and G lands takes place at the same general relative factor a

$$\begin{aligned} T_{\mathsf{CDR} \triangleright G}\, c^v_{\mathsf{CDR}} &= a\,(c^{pot}_G - c_G) \\ T_{\mathsf{CDR} \triangleright F}\, c^v_{\mathsf{CDR}} &= a\,(c^{pot}_F - c_F) \end{aligned} \tag{74}$$

with potential natural vegetation extents c^{pot}_K. These potentially available F and G lands also constrain the transition matrix elements for the conversion from sDACCCS cover as

$$\begin{aligned} T_{\mathsf{CDR} \triangleright G} &\leq \frac{c^{pot}_G - c_G}{c^v_{\mathsf{CDR}}} \\ T_{\mathsf{CDR} \triangleright F} &\leq \frac{c^{pot}_F - c_F}{c^v_{\mathsf{CDR}}} \end{aligned} \tag{75}$$

Together, Equations (74) and (75) result in

$$a \leq \frac{1}{c^v_{\mathsf{CDR}}} \tag{76}$$

On the other hand,

$$\begin{aligned} T_{\mathsf{CDR} \triangleright N} &= T_{\mathsf{CDR} \triangleright G} + T_{\mathsf{CDR} \triangleright F} \\ &= \frac{a}{c^v_{\mathsf{CDR}}}(c^{pot}_N - c_N) \end{aligned} \tag{77}$$

Thus, in combination of Equations (74) and (77),

$$a = T_{\mathrm{CDR} \triangleright N} \, \frac{c^{v}_{\mathrm{CDR}}}{c^{pot}_{N} - c_N} \tag{78}$$

Combining conditions (76) and (78), the annual transition matrix elements for *rule 0* are

$$T_{\mathrm{CDR} \triangleright G} = \min\left[\frac{1}{c_{\mathrm{CDR}}}, \frac{T_{\mathrm{CDR} \triangleright N}}{c^{pot}_{N} - c_N}\right] \cdot (c^{pot}_{G} - c_G) \tag{79}$$

$$T_{\mathrm{CDR} \triangleright F} = \min\left[\frac{1}{c_{\mathrm{CDR}}}, \frac{T_{\mathrm{CDR} \triangleright N}}{c^{pot}_{N} - c_N}\right] \cdot (c^{pot}_{F} - c_F) \tag{80}$$

From analogous reasoning, follow the amended calculations for *rule 1* for shrinking agricultural land

$$\begin{aligned} T_{C \triangleright G} = \min\left[\frac{1}{c_C}, \frac{T_{C \triangleright N}}{c^{pot}_{N} - c_N - T_{\mathrm{CDR} \triangleright N} \, c^{v}_{\mathrm{CDR}}}\right] \\ \cdot (c^{pot}_{G} - c_G - T_{\mathrm{CDR} \triangleright G} \, c^{v}_{\mathrm{CDR}}) \\ T_{C \triangleright F} = \min\left[\frac{1}{c_C}, \frac{T_{C \triangleright N}}{c^{pot}_{N} - c_N - T_{\mathrm{CDR} \triangleright N} \, c^{v}_{\mathrm{CDR}}}\right] \\ \cdot (c^{pot}_{F} - c_F - T_{\mathrm{CDR} \triangleright F} \, c^{v}_{\mathrm{CDR}}) \end{aligned} \tag{81}$$

In addition to the default JSBACH model, *rule 1* now accounts for the fraction of potentially available natural lands which have already been "filled up" with re-converted CDR land due to *rule 0*. This fill-up is expressed by the terms $T_{\mathrm{CDR} \triangleright \{N,G,F\}} \, c^{v}_{\mathrm{CDR}}$ in equations (81). Similarly, the amendments to *rules 2* and *3* for shrinking agricultural land consist of corrections to the potential natural vegetation extent

$$T_{P \triangleright F} = \min\left[T_{P \triangleright N}, \frac{c^{pot}_{F} - (c_F + T_{C \triangleright F} \, c_C + T_{\mathrm{CDR} \triangleright F} \, c_{\mathrm{CDR}})}{c_P}\right] \tag{82}$$

$$T_{P \triangleright G} = \min\left[T_{P \triangleright N} - T_{P \triangleright F}, \frac{c^{pot}_{G} - (c_G + T_{C \triangleright G} \, c_C + T_{\mathrm{CDR} \triangleright G} \, c_{\mathrm{CDR}})}{c_P}\right] \tag{83}$$

Analogous to Reick et al. [68], the CDR model interpolates the realized land use transitions to daily resolution and converts them into tile contributions

$$T^{(d)}_{k_j \triangleright \mathrm{CDR}_i} = \frac{T_{k \triangleright \mathrm{CDR}}}{N_d} \tag{84}$$

$$T^{(d)}_{\mathrm{CDR} \triangleright k_j} = \begin{cases} \frac{T_{\mathrm{CDR} \triangleright k}}{N_d} \cdot \frac{c_{k_i}}{c_k}, & k \in \{P, C\} \\ \frac{T_{\mathrm{CDR} \triangleright k}}{N_d} \cdot \frac{c^{pot}_{k_i} - c_{k_i}}{c_k}, & k \in \{F, G\} \end{cases} \tag{85}$$

Here, the k_j are different plant functional types of land cover class k. Following each step of land cover change, we recompute the box cover fraction of sDACCCS as

$$f_{\mathrm{CDR}} = \max\Big[\min\big[c^{v}_{\mathrm{CDR}} \cdot f_v + c^{b}_{\mathrm{CDR}} \cdot (1 - f_v),\, 1\big],\, 2c_\epsilon\Big] \tag{86}$$

which enters again into the model for CO_2 sequestration.

Transitioning from no-CDR simulation spin-ups to experiments with sDACCCS representation

Integrating the components of our CDR model into ECHAM6.3 and JSBACH entails technical extensions to these models, including model restart files and support code. They spread across JSBACH's entire call tree (Supplementary Figure S S6) and into the land coupling variables of ECHAM6.3. Throughout a simulation, MPI-ESM writes restart files, typically at an interval of one simulation year. These files contain all necessary state variables to re-initialize the model from a previous simulation. Extending JSBACH with a land cover class for sDACCCS implicitly changes the format of restart files because the number of land cover types changes. To re-initialize from a spun-up simulation without sDACCCS representation, our CDR component comes with a transitioning mode. This mode runs for the first year of a simulation with CDR. During this year, no sDACCCS can deploy on the land surface, but the sDACCCS land cover type already exists in the model at a minimal technical fraction. This allows computing relevant restart variables for CDR land cover without impacting the simulated Earth system state. Only after this initial year of transition mode the CDR cover is allowed to change to non-negligible cover fractions. Our CDR extension further comes with tools for setting up CDR scenarios, pre-processing restart and input files, and post-processing CDR-specific output variables.

Zero-dimensional model for CDR through sDACCCS chains

Along seven steps, the zero-dimensional model follows the process chain from incident irradiation on a solar absorber to resulting CO_2 withdrawal (Figure S9).

(i) Absorption of solar irradiation JSBACH provides a visible and a near-infrared spectral band aggregated from the sixteen spectral bands of ECHAM6.3. We diagnose the effective absorption coefficient a_ξ, $\xi \in \{\mathsf{vis}, \mathsf{nir}\}$ of a tile

$$a_\xi = (1 - \alpha_{\mathsf{CDR},\xi})(1 - c_s) + (1 - \alpha_{\mathsf{s},\xi})\, c_s \tag{87}$$

with albedo $\alpha_{\mathsf{CDR},\xi}$ of the solar absorber in the spectral band ξ and snow cover fraction c_s. Thus, the radiative forcing includes the shading effect of snow cover, assuming that snow-covered solar absorbers can still operate with the fraction of irradiation that does not get reflected. The absorbed fraction of the incident irradiation I_{surface} follows as

$$I_{a,\xi} = a_\xi \cdot I_{\mathsf{surface}} \ \left[\mathrm{W/m^2}\right] \tag{88}$$

(ii) Effective energy flux The absorbed energy flux is subject to losses in the solar absorber and along the process chain. We capture these losses with the system efficiency η_{sys}. In addition, the amount of energy available to reduce CO_2 depends on the spatial setup of solar absorbers. We incorporate this constraint with a space factor $\mu_{\mathsf{space}} = 0.25$ which converts the area of solar absorbers to the land use footprint of sDACCCS. We choose μ_{space} in the order of typical space factors for photovoltaic devices [72, 69, 73], assuming that comparable spacing would also apply to CO_2 capturing facilities. Then, the effective irradiation flux available for reducing CO_2 molecules is

$$I_{e,\xi} = I_{a,\xi} \cdot \eta_{\mathsf{sys}} \cdot \mu_{\mathsf{space}} \ \left[\mathrm{W/m^2}\right] \tag{89}$$

(iii) Effective photon flux In a solar absorber, incident photons can be thought of as generating electron–hole pairs ($e^- + h^+$) based on the photoelectric effect. Subsequently, these electrons can be used to reduce CO_2 molecules in a catalytic reaction. The internal quantum efficiency $\eta_{\mathsf{QE}}(\lambda)$ captures the yield efficiency for charge carriers resulting from the photoelectric effect in

response to incident photons of wavelength λ [74]. $\eta_{\mathsf{QE}}(\lambda)$ differs, for example, between different materials and setups used for a solar absorber [74]. The photon flux Φ_ξ within a spectral band $[\lambda_1, \lambda_2]$ incorporates this electron yield efficiency

$$\Phi_\xi = \frac{1}{hc} \int_{\lambda_1}^{\lambda_2} \mathrm{d}\lambda \, F(\lambda) \cdot \eta_{\mathsf{QE}}(\lambda) \cdot \lambda \tag{90}$$

Here $F(\lambda)$ is the wavelength-dependent effective irradiation flux onto the solar absorber, c is the speed of light, and h the Planck constant. Given the simple spectral setup of JSBACH with two aggregated spectral bands and the uncertain technological details of sDACCCS, we assume $\eta_{\mathsf{QE}}(\lambda)$ as constant over a spectral band, $\eta_{\mathsf{QE}}(\lambda) \equiv \eta_{\mathsf{QE}}$, and employ a normalization approach of the spectral irradiance (SI S1). Then, we obtain a scaling constant relating the integrated spectral power I_ξ to the photon flux in the respective spectral band

$$\mu_\xi = {}^{\Phi_\xi}/_{I_\xi} \; \left[{}^{1}/_{(\mathsf{W} \cdot \mathsf{s})}\right] \tag{91}$$

One can interpret μ_ξ as the number of electrons excited per unit of integrated irradiance in the spectral band ξ (SI S1).

(iv) Solar energy demand of sDACCCS process chains For the high efficiency (hE) process chain, μ_ξ would already correspond to the conversion efficiency from incident irradiation to CO_2 withdrawal flux if no further energy to capture atmospheric CO_2 would be required. However, the CO_2 reduction cannot consume all available electrons because they also need to drive the capturing process. For formate as a sink product, the DAC stage consumes about one out of four available electrons (SI S2), assuming reported energy demands of existing DAC facilities around $0.5\,\mathsf{kWh}$ per kilogramm of captured CO_2 [75] and 32% yield efficiencies of future photoabsorbers [76]. We incorporate this efficiency discount by modifying the conversion efficiency, $\mu_{\mathrm{CO_2}/e^-} \rightarrow \tilde{\mu}^{\mathsf{hE}}_{\mathrm{CO_2}/e^-}$ (SI S2). In addition to the solar energy needed for atmospheric CO_2 capture, the low efficiency (lE) process chain demands energy for electrolysis. Assuming 80% overpotential of an industrial-scale electrolysis cell in the order of CO_2–to–carbon monoxide reduction [cf. 77] and silicate photovoltaic cells (25% yield efficiency [76]), this process stage demands $4.26\,\mathsf{kWh}$ per kilogramm of CO_2 reduced to formate (SI S2). We incorporate this additional energy demand in $\tilde{\mu}^{\mathsf{lE}}_{\mathrm{CO_2}/e^-}$ (SI S2).

(v) CO_2 sequestration flux Then, drawing on Equation (91) and on the energy flux available to excite electron–hole pairs (Equation (89)), the CO_2 sequestration flux $F_{\mathrm{CO_2},\,\xi}$ is given by

$$F_{\mathrm{CO_2},\,\xi} = I_{e,\,\xi} \cdot \tilde{\mu}_\xi \cdot \mu^i_{\mathrm{CO_2}/e^-} \cdot M_{\mathrm{CO_2}} \cdot {}^{1}/_{N_A} \cdot \mu_c \; \left[{}^{\mathsf{kg(CO_2)}}/_{(\mathsf{m}^2 \cdot \mathsf{s})}\right] \tag{92}$$

Here, $\mu^i_{\mathrm{CO_2}/e^-}$ denotes the number of CO_2 molecules reduced per electron and $i \in \{\mathsf{lE}, \mathsf{hE}\}$. The factor μ_c calibrates sDACCCS' land footprint to theoretical values from May and Rehfeld [73] (SI S4). The molar mass of CO_2, $M_{\mathrm{CO_2}}$, and the Avogadro constant N_A convert the net count of CO_2 molecules into a mass flux. This mass flux constitutes the CDR forcing in the CO_2 balance of ECHAM6.3.

(vi) Carbon sink pool and potential withdrawal From the withdrawal fluxes of the two spectral bands, $F_{\mathrm{CO_2,\,vis}}$ and $F_{\mathrm{CO_2,\,nir}}$, we diagnose the net change in carbon sink product m_{C} (here, expressed in units of CO_2, $m_{\mathrm{CO_2}}$). Given the area occupied by sDACCCS at time t in a grid cell with area A^t_{cell}, $A^t_{\mathsf{CDR}} = A^t_{\mathsf{cell}} \cdot f^t_{\mathsf{CDR}}$, the annual CO_2 withdrawal is

$$m_{\mathrm{CO_2}} = \sum_{t=t_0}^{t_0+N_t} m^t_{\mathrm{CO_2}} = 10^{-12} \cdot \sum_{t=t_0}^{t_0+N_t} (F^t_{\mathrm{CO_2,\,nir}} + F^t_{\mathrm{CO_2,\,vis}}) \cdot A^t_{\mathsf{CDR}} \cdot \Delta t \; \left[\mathsf{Gt(CO_2)}\right] \tag{93}$$

where t_0 denotes the first time step of a simulated year, N_t is the number of steps in that year, and Δt is a time step's length. Drawing on Equation (93), we also obtain the climatological CO_2 withdrawal potential ψ_{τ_i} at the first time step of year i, τ_i.

$$\psi_{\tau_i} = \frac{1}{N_{\text{clim}}} \sum_{\tau=\tau_{i-N_{\text{clim}}}}^{\tau_i} \sum_{t=\tau_i}^{\tau_{i+N_t}} m_{\text{CO}_2}^t \frac{A_{\text{CDR, max}}}{A_{\text{CDR}}^t} \tag{94}$$

Here, $A_{\text{CDR, max}}$ is the upper limit for the grid cell area occupied by sDACCCS, irrespective of land availability constraints. We choose an averaging interval of $N_{\text{clim}} = 15\,\text{yr}$, still allowing for variability beyond that time scale. The climatological withdrawal potential translates a CDR target into changes in sDACCCS cover fraction when computing land use transitions (see below).

(vii) Thermal cooling from CO_2 fixation The sDACCCS process chain converts solar energy into energy stored in the chemical bonds of a carbon-rich sink product. Storing this product away in an integrated process chains as in the hE scenario corresponds to a cooling of the surface climate that is not captured in the energy balance of MPI-ESM. The ESM's radiative scheme would overestimate the long-wave surface forcing through thermalization of photons that get absorbed by solar absorbers, if this effect of energy storage is not corrected for. As a conservative estimate, we diagnose the heat flux due to CO_2 fixation from the minimum energy needed to drive the reduction of CO_2 to formate, that is its Gibbs free energy of formation $\Delta G_{\text{CO}_2 \to \text{HCOOH}} = 1.4\,\text{eV} = -135.08\,{}^{\text{kJ}}/_{\text{mol}}$ [78, 73]. We diagnose the thermal cooling from constructing chemical bonds as

$$H_{\text{bonds}} = \frac{F_{\text{CO}_2} \cdot \Delta G_{\text{CO}_2 \to \text{HCOOH}}}{10^{-3} \cdot M_{\text{CO}_2}} \left[{}^{\text{W}}/_{\text{m}^2}\right] \tag{95}$$

and couple H_{bonds} into the surface energy balance of JSBACH

$$C \frac{\partial T_{\text{surf}}}{\partial t} = R_{\text{net}} + H_{\text{sensible}} + H_{\text{latent}} + H_{\text{ground}} + H_{\text{bonds}} \tag{96}$$

Here, C denotes the (dynamic) heat capacity of the surface soil layer, T_{surf} is the surface temperature, R_{net} the net radiation, and H_{sensible}, H_{latent}, and H_{ground} are sensible, latent, and ground heat fluxes, respectively [68].

Muting CDR at low ambient CO_2 concentrations

No chemical reaction removing CO_2 will occur efficiently if its concentration $[CO_2]$ is too low. Real-world reaction kinetics of direct air capture and (photo-)electrochemistry are complex and require dedicated modeling of catalysts and electrolytes based on real-world experimental data. This modeling based on first principles is different from the aim of our study, and an Earth system model would not be an ideal tool for this. Instead, we aim at storyline experiments to assess the feasibility of sDACCCS as a large-scale CDR approach in general. Therefore, a simple sigmoid response curve approximates the reaction kinetics at low CO_2 concentrations. Sigmoid response curves are a widely applied model for chemical reactions, mainly if the reaction rate depends (or is assumed to depend) on the concentration of a single educt [79]. We employ the logistic function

$$f_l = \frac{1}{1 + \exp\big(-\kappa([CO_2] - [CO_2]_H)\big)} \tag{97}$$

with decay rate $\kappa = 0.05\,{}^{\text{mol(air)}}/_{\mu\text{mol(CO)}_2}$ and a concentration at the inflection point $[CO_2]_H = 160\,{}^{\mu\text{mol(CO)}_2}/_{\text{mol(air)}}$. The chosen parameters correspond to a CDR response ≥ 0.999 for $[CO_2] >$

$299\,{}^{\mu mol}/_{mol}$ and ≥ 0.99 for $[CO_2] > 252\,{}^{\mu mol}/_{mol}$. In the model, we set $[CO_2] < 300\,{}^{\mu mol}/_{mol}$ as a threshold below which the response curve can affect CO_2 removal because of numerical reasons. If surface CO_2 concentrations in our scenarios were close to this threshold or within the range of the dampening curve, CO_2 removals would be sensitive to the parameters of the sigmoid. However, CO_2 concentrations in all of our study's experiments are far above the threshold.

As a consequence, the dampened CO_2 removal at low concentrations practically serves the purpose of numerical stability because it prevents local concentrations from dropping below unphysical levels if CO_2 concentrations are already low because of the variability of atmospheric mixing and CDR combined. This is a rare case in the model and typically would occur on time scales of single time steps (20 minutes). On the temporal resolutions of interest in our study, atmospheric mixing continuously readjusts CO_2 abundance for local CDR, even at high grid cell coverages (see Figure 3a of the updated manuscript). Future work should refine the parameters and shape of the response curve if it is relevant to the envisaged study.

Linear scaling of the photon flux

To accommodate (5) within JSBACH's simple spectral representation, we normalize the photon flux Φ_ξ by the integrated spectral power $I_\xi = \int_{\lambda_1}^{\lambda_2} \mathrm{d}\lambda\, F(\lambda)$ of the AM1.5G reference spectrum [80, 81] using the YaSoFo tool for spectral integration [73]. Table 1 summarizes results of the spectral integrations. Utilizing the same reference spectrum globally in our model neglects non-linearities in the electron yield curve of the photoelectric effect, the local seasonality of solar insolation, and climatic effects on the solar spectrum. Thus, precisely estimating global CDR potential for a specific technological pathway requires dedicated spectral modeling. Still, we correct some of these shortcomings by model calibration (see below).

S2 Process chain efficiencies of sDACCCS

To integrate energy harvest and process chain efficiencies of the hE and lE technology scenarios into the zero-dimensional sDACCCS parametrization, we draw on modified conversion efficiencies. For the hE scenario, the conversion efficiency incorporates the solar energy harvest required to drive DAC. In the lE scenario, energy harvest for DAC and electrolysis are incorporated. The on-going development of sDACCCS and DAC-type process chains limits its available efficiency estimates. However, both technology scenarios have been successfully demonstrated for hydrogen production [74, 82, 83] and with a focus on carbon capture and utilization [84, 85], aiming at synthetic fuel production not at maximizing the CO_2 withdrawal potential of sink products.

hE technology scenario

We include the energy harvest for the hE scenario's CO_2 capturing stage into its conversion factor $\mu^{\mathrm{hE}}_{CO_2/e^-}$. Therefore, we compute the module area of photovoltaic solar absorbers required to drive the DAC process delivering CO_2 as an input for photoelectrochemical (PEC) reduction. First, we obtain the CO_2 withdrawal flux F per PEC module area at a given insolation I from (7). Here, we utilize $\mu_{CO_2/e^-} = \eta_{\mathrm{STC}}$, where η_{STC} is the solar–to–carbon conversion efficiency for the PEC reduction stage alone [73]. The CO_2 withdrawal corresponds to an energy demand $E_d = F \cdot 0.5\,{}^{\mathrm{kWh}}/_{\mathrm{kg}(CO_2)}$ of the DAC stage, based on reported values of DAC facilities [86, 75] and assuming that the sorbent of CO_2 can be used within the electrolyte. Then,

$$F' = F \cdot \left(1 - \frac{F \cdot E_d}{\eta_{\mathrm{PV}} \cdot I}\right) \tag{98}$$

where η_{PV} denotes the efficiency of photovoltaic devices, assuming prospective perovskite-silicon tandem cells [76]. Now, solving (7) for the conversion factor, including 50% system loss, and utilizing the constants and parameters summarized in Table 3, we obtain $\mu^{\mathsf{hE}}_{\mathsf{CO_2}/e^-} = 0.071$. Integrating the energy harvest for DAC and associated efficiencies of the solar absorbers thus reduces the ideal conversion efficiency [73] by ∼24.1%.

lE technology scenario

In addition to the energy required to drive the DAC process, the lE scenario demands energy to drive the extraction of the CO_2 from the DAC's sorbent and for electrolysis. The minimum energy required to power the electrolytic reduction of CO_2 to formate is

$$E_{\mathsf{CO_2}} = U_{\mathsf{cell}} \cdot F \cdot n_{\mathsf{CO_2}} \cdot n_e \tag{99}$$

with U_{cell} being the cell potential, F the Faraday constant, $n_{\mathsf{CO_2}}$ the number of moles of CO_2 consumed, and $n_e = 2$ the number of electrons consumed in the half-cell evolution reaction to formate. n_i is calculated as $n_i = {}^{m_i}/_{M_i}$, with m_i being the mass of the educt/product consumed/produced and M_i the respective molar mass. In real-world electrolysis, the activation of the electrochemical reaction and electrolyte resistance demand additional energy, leading to a so-called overpotential [87]. As a result, U_{cell} has to be higher than the reaction's thermodynamic limit, as given by its Gibbs free energy [87]. Therefore, we assume cell overpotentials of 80% in light of experimental data for the reduction of CO_2 to carbon monoxide [77]. Then, drawing on the parameters and constants as summarized in Table 4, we obtain an energy demand for the electrolysis stage of $E_{\mathsf{CO_2}} = 3.045\,\mathsf{kWh}$ per $\mathsf{kg}(\mathsf{CO_2})$ reduced, corresponding to $E_{\mathsf{HCOOH}} = 1.456\,\mathsf{kWh}$ per kg formate produced. We further assume a system efficiency $\eta_{\mathsf{el}} = 0.5$ for the electrolysis setup as for the hE pathway. The energy demand of the DAC process is analogous to the hE scenario. On the energy supply side, we assume typical efficiencies of modern commercial crystalline silicate photovoltaic cells [76], applying a 1-2% discount on the most recent values to account for some lag in the rollout of newest technologies. Table 5 aggregates the assumend values for energy demands and supply of the lE scenario.

With the aggregated energy demand $E_d = \frac{E_{\mathsf{CO_2}}}{\eta_{el}} + E_{\mathsf{DAC}}$ per unit of CO_2 withdrawn from the atmosphere, we can deduce the associated withdrawal flux per module area of solar absorbers at a given insolation $I = 1000\,{}^{\mathsf{kWh}}/_{\mathsf{yr}}$ as $F_{CO_2} = 29.10\,{}^{\mathsf{kg(CO_2)}}/_{\mathsf{m^2(module)\cdot a}}$ where

$$F_{CO_2} = I \cdot \frac{\eta_{\mathsf{PV}}}{E_d} \tag{100}$$

Then, we are able to compute an effective conversion efficiency for the lE process chain by inverting (7). Again, we draw on the AM1.5G reference spectrum to convert between the power-related efficiency η_{PV} and an efficiency relating to the photon flux

$$\mu^{\mathsf{lE}}_{\mathsf{CO_2}/e^-} = \frac{F_{CO_2}}{I \cdot \mu_{\mathsf{nir+vis}}} \cdot \frac{N_A}{M_{CO_2}} \tag{101}$$

Here, we employ a scaling constant $\mu_{\mathsf{nir+vis}}$ allocating the combined irradiation I to both spectral windows of JSBACH by their respective contribution to the overall spectral power

$$\mu_{\mathsf{nir+vis}} = \frac{\Phi_{\mathsf{nir}} + \Phi_{\mathsf{vis}}}{I_{\mathsf{nir}} + I_{\mathsf{vis}}} \tag{102}$$

where individual contributions are assumed to be

$$I_\xi = \frac{\Phi_\xi}{I_\xi} \frac{I_\xi}{I_{\mathsf{nir}} + I_{\mathsf{vis}}} \cdot I \tag{103}$$

Drawing on the parameters in Table 1 and 50% system loss, we obtain $\mu^{\mathsf{lE}}_{\mathsf{CO_2}/e^-} = 0.0347$.

S3 Spatiotemporal sDACCCS targets and compatible emission forcings

One of the distinguishing features of our CDR extension to MPI-ESM is the ability to model CDR explicitly compared to the implicit representation of typical scenario simulations. However, to still obtain an effective emission forcing that is compatible between simulations and with the SSP framework, we modify the SSP emission forcing. Then, the explicit CO_2 removal and the modified forcing combine to SSP1-2.6 again. As a first step, we interpolate global emission scenarios linearly from their native five-yearly temporal resolution [88] to the CDR target's annual resolution. Due to the shape of SSP scenarios, a pice-wise linear interpolation is preferable to higher order interpolation to avoid a systematic bias in the effective emission forcing. In case of the max scenarios, the difference in net emission forcing $\Delta E = E_{\mathrm{SSP3-7.0}} + E_{\mathrm{CDR_{max}}} - E_{\mathrm{SSP1-2.6}} = \frac{E_{\mathrm{SSP3-7.0}} - E_{\mathrm{SSP1-2.6}}}{2} > 0$. For min scenarios, $\Delta E = E_{\mathrm{SSP1-2.6}} + E_{\mathrm{CDR_{min}}} - E_{\mathrm{SSP1-2.6}} = E_{\mathrm{CDR_{min}}} < 0$. Then, we re-scale all emitters in the spatial emission scenario as

$$E_{ij} = E_{ij} + \Delta E \cdot \frac{E_{ij} A_{ij} \iota^E_{ij}}{\sum_{ij} E_{ij} A_{ij} \iota^E_{ij}} \tag{104}$$

where the mask

$$\iota^E_{ij} = (E_{ij} > 0 \wedge |\phi_{ij}| < 88°) \tag{105}$$

The deployment scheme uses contribution weights w^c_{ij} to split the global target change into contributions of individual grid cells (Section S1). The w^c_{ij} have to fulfil

$$\sum_{i,j} {}^{w^c_{ij}}/_{w^a_{ij}} = 1 \tag{106}$$

with area weights w^a_{ij}. In the Eql scenario, all grid cells within a latitudinal band from ϕ_S to ϕ_N contribute a relatively equal share to the overall sDACCCS cover based on their area. We limit deployment to this latitudinal range to account for the sparse year-round sunlight in high latitudes, reducing the cost-efficiency of solar absorbers. The contribution mask for a grid cell $(i, j) \in \{(1, 1), (1, 2)(2, 1), \ldots, (N_{\mathrm{lon}}, N_{\mathrm{lat}})\}$ is

$$\iota^{\mathsf{Eql}}_{ij} \equiv \left(\iota^{\mathsf{land}}_{ij} = \mathsf{TRUE} \wedge |\phi_{ij}| < 60\,°\right) \tag{107}$$

with ϕ_{ij} indicating the cell's latitude and $\iota^{\mathsf{land}}_{ij}$ the land–sea mask (returning TRUE for land grid cells). Then, the global normalization of contribution weights is

$$\mathcal{N}^{\mathsf{Eql}} = \sum_{i,j \in I} w^a_{ij} \tag{108}$$

with area weights w^a_{ij} and $I = \{(i, j) : \iota^{\mathsf{Eql}}_{ij} = \mathsf{TRUE}\}$. The contribution weights result as

$$w^c_{ij} = \begin{cases} {}^{w^a_{ij}}/_{\mathcal{N}^{\mathsf{Eql}}}, & \iota^{\mathsf{Eql}}_{ij} = \mathsf{TRUE} \\ 0, & \text{else} \end{cases} \tag{109}$$

For the Prop scenario, we draw on a CDR burden sharing paradigm by Fyson et al. [89], which follows a "polluter pays principle" on the country level. Fyson et al. allocate responsibility for CDR deployment to those countries that exceed their "fair share" of global CO_2 emissions, taking emissions in 1990 as a baseline. To spread the countries' burdens across the grid space, we first compute gridded country masks ι^k_{ij} from political boundaries k and JSBACH's land-sea mask. For that purpose, we clip the land-sea mask to country boundaries

and interpolate missing values. This approach ensures that no ι_{ij}^k overlap, with contributions below the grid's resolution being neglected. Then, the contribution of each cell is

$$w_{ij}^c = \sum_k \frac{b^k w_{ij}^a \iota_{ij}^k}{\sum_{ij} w_{ij}^a \iota_{ij}^k} \tag{110}$$

where b^k denotes the emission burden of country k. Again, we normalize the w_{ij}^c as for the Eql scenario to fulfill Equation (106).

As a separate spatial constraint, we limit CDR cover on land that is (partially) mountainous, protected, urban, or covered by water (Figure 1c). Thus, we exclude area fractions that would likely not be used for CDR built-up. To constrain the fraction of urban settlements within each area, we draw on Hurtt et al. [71]. For all remaining constraints, we refer to ESMAP [90].

S4 Validating the extended MPI-ESM model

Effective emission forcing

We validate the physical consistency of the combined forcing of anthropogenic emissions and CO_2 removal by comparing global removal targets with simulated CDR and the atmospheric CO_2 response between CDR experiments and the pathway control experiment. Annual and cummulative CDR deployment follows targets precisely until ~2150 and we find good agreement between the CO_2 responses (Figure 2 a–d). Thus, the explicit and interactive CDR deployment scheme behaves accurately. Furthermore, these results demonstrate that CDR and the emission scenario combine accurately to an effective emission forcing. After 2150 the model exhibits some difficulties in scaling CDR down. A possible explanation is an insufficient amount of potential natural vegetation that could occupy the previously sDACCCS-covered land. The fact that the model still follows declining CDR targets for a couple of years before partially leveling off supports this hypothesis. Nonetheless, since the drift off the CDR targets occurs well outside of our time windows of interest, it is not relevant for our study's results. However, for investigating the long-term reversibility of CDR implications into the next centuries with our explicit CDR representation, this shortcoming would still have to be rectified.

Carbon conservation

A consistent response of the modeled carbon cycle is crucial for evaluating the implications of land conversions for sDACCCS on carbon stocks. Here, Figure S8 validates the consistency of the extended model's carbon cycle. We conduct test simulations (α–ϵ) differing by the global CDR target ($\alpha \leftrightarrow \beta$, γ, $\delta \leftrightarrow \epsilon$; Figure S8 b) and the resulting emission forcing (Figure S8 c), as well as the spatial sDACCCS deployment under the same effective emission pathway (β–spread-out, γ–semi-localized, δ–localized). Test experiments span 2015 to 2100. We observe a slight global drift in the global carbon budget, but it is minor compared to absolute global, marine, terrestrial, and atmospheric carbon stocks as well as their respective changes over the course of the simulations. Crucially, representing sDACCCS explicitly does not significantly alter this response, justifying our comparison between simulation experiments.

Calibrating the land footprint of sDACCCS chains

The land use efficiency of a CDR approach co-determines its environmental implications. Here, we seek to represent the land footprint of sDACCCS chains as suggested by May and Rehfeld [73, 91]. Because our zero-dimensional parametrization and JSBACH's coarse resolution of the solar spectrum strongly approximate CO_2 capturing and electrochemical processing

[73, 92], we calibrate the modeled sDACCCS land footprint to match theoretical calculations. This ensures compatible results between different studies. Given that in the zero-dimensional parametrization CO_2 removal responds linearly to irradiation, we can conduct this calibration at any pair of irradiation and removal as long as system efficiencies correspond. As an example, May and Rehfeld [73] compute that $135,000\,\mathrm{km}^2$ of land would be needed for integrated photoelectrochemical devices to deliver a CO_2 withdrawal of $10\,\mathrm{Gt\,CO_2/yr}$ assuming irradiance conditions of the Sahara desert. This theoretical calculation assumes a total system loss of 50 % and includes the footprint of the required infrastructure. However, land use for harvesting energy to drive CO_2 capture is not included.

We conduct the calibration only for the hE process chain and prior to determining the effective conversion factors μ_{hE} and μ_{IE}, which incorporate the effect on land use of energy harvest for DAC and industrial electrolysis into the technology scenarios. This approach is motivated by the fact that both scenarios can be phrased in terms of an effective theoretical conversion efficiency from solar irradiation to CO_2 removal.

Three steps make up the calibration procedure (Figure S7). Initially, we conduct a one-year test simulation with the uncalibrated sDACCCS model (blue in Figure S7), that is with a calibration factor $\mu_{\mathsf{C}} = 1$ and without accounting for the reduced conversion efficiency due to energy harvest ($\mu_{\mathsf{hE}} = 1$). Based on the simulated CO_2 removal potential ψ (Equation (9)) on all grid cells with $\psi > 0$, we match the simulated, uncalibrated response to the zero-dimensional model when calculated offline (dashed line in Figure S7). This step is necessary to again account for the two simulated spectral windows in the MPI-ESM model. Finally, we utilize the calibrated offline response (dashed in Figure S7) to determine the calibration factor $\mu_{\mathsf{C}} = 1.702$ for matching theoretical expectation (solid line in Figure S7) with the simulations (green in Figure S7).

Table 1 | Integrated properties of the reference spectrum [80, 81] used for scaling the electron yield of solar absorbers with insolation.

Parameter	Description	Value	Unit
$\Phi^{vis}_{\lambda_1,\lambda_2}$	photon flux (vis)	0.01074	10^{23} photons$/(m^2 \cdot s)$
$\Phi^{nir}_{\lambda_1,\lambda_2}$	photon flux (nir)	0.01235	10^{23} photons$/(m^2 \cdot s)$
$I^{vis}_{\lambda_1,\lambda_2}$	spectral power (vis)	467.3872	W/m^2
$I^{nir}_{\lambda_1,\lambda_2}$	spectral power (nir)	257.0784	W/m^2

Table 2 | Process stage efficiencies for energy harvest, direct air capture, and electrolysis as assumed for the hE technology scenario.

Process stage	Energy demand (+)/supply (-)
PV	$-I \cdot \eta_{\mathsf{PV}}$ kWh$(m^2 \cdot a)$
DAC	0.5 kWh/kg CO_2 [86] (no thermalization required)
PEC	parameterized in the zero-dimensional sDACCCS model

Table 3 | Efficiencies employed to compute the hE chain's conversion efficiency $\mu^{\mathsf{hE}}_{CO_2/e^-}$.

Parameter	Description	Value
η_{PV}	PV efficiency	0.32 [76] (perovskite-silicon tandem cells)
η_{STC}	solar-to-carbon efficiency formate (dual-junction solar absorber)	0.19 [73]
η_{sys}	system efficiency	0.5 [73]
μ_{space}	space factor of PV and solar absorbers	0.25

Table 4 | Constants and parameters employed to compute the lE chain's conversion efficiency μ_{lE}.

Parameter	Description	Value	Unit
U_{cell}	cell potential	2.5 (80% overpotential [77])	V
F	Faraday constant	96485	C/mol
$\Delta G_{CO_2 \to HCOOH}$	Gibbs free energy of CO_2 reduction to formate	1.4	eV
m_F	mass of formate produced	1	kg
M_F	molar mass of formate	46.03	g/mol
m_{CO_2}	mass of CO_2 reactant	1	kg
M_{CO_2}	molar mass of CO_2	44.01	g/mol
I	irradiation	location-dependent	$kWh/(m^2 \cdot a)$
η_{PV}	solar energy conversion efficiency of PV (silicon) [76]	0.25	-
η_{el}	system efficiency electrolysis	0.5	-
μ_{space}	space factor of PV	0.25	-

Table 5 | Energy supply and demand for the process stages of the lE technology scenario.

Process stage	Energy demand (+)/supply (-)	Unit
PV	$-I \cdot \eta$	kWh$/(\mathrm{m}^2 \cdot \mathrm{a})$
DAC	0.5 + 2.0 [86]	kWh$/\mathrm{kg}(CO_2)$
Electrolysis	3.045	kWh$/\mathrm{kg}(CO_2)$

Table 6 | Aggregated IPCC reference regions [93] that are highlighted in the main text.

Abbreviation	IPCC region(s)	Name(s) of the (aggregated) IPCC region(s)
CNA	WNA, CNA, ENA	Western, central, and eastern North America
NSA	NSA, SAM	Northern South America and South American Monsoon
NCE	NEU, WCE	Northern, western, and central Europe
SAH	SAH	Sahara
ARP	ARP	Arabian Peninsula
EAS	EAS	Eastern Asia

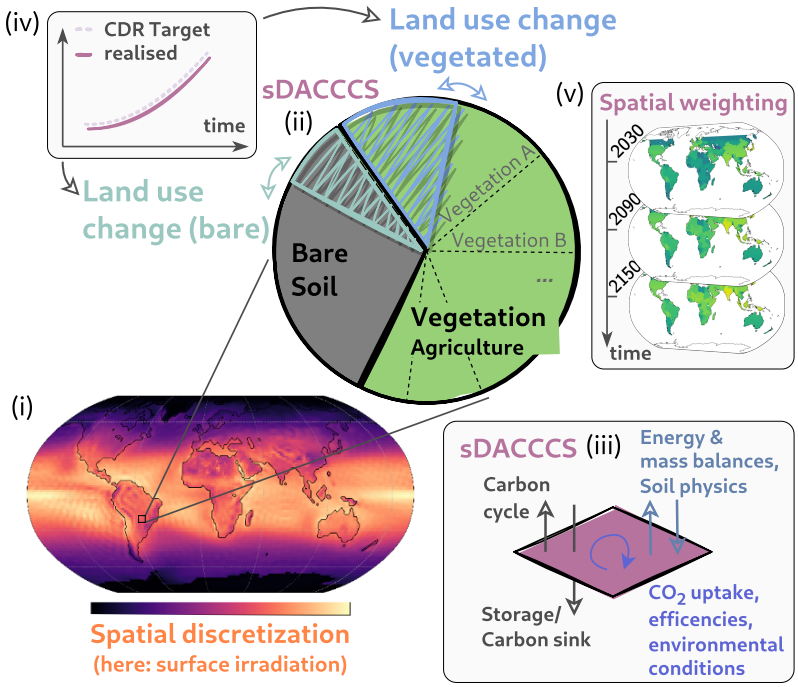

Figure S1 | Schematic overview of representing sDACCCS as an interactive and dynamic land surface type in MPI-ESM/JSBACH. Within JSBACH's spatial discretization (i) and tiling scheme (ii), we describe sDACCCS separately on vegetated and bare land (ii). In the model, sDACCCS interacts with its environment through surface balances and the carbon cycle and its CDR chain gets driven by solar irradiation (iii). In response to targeted and realized global CDR (iv), the model changes sDACCCS cover interactively while taking a spatial deployment scenario into account (v).

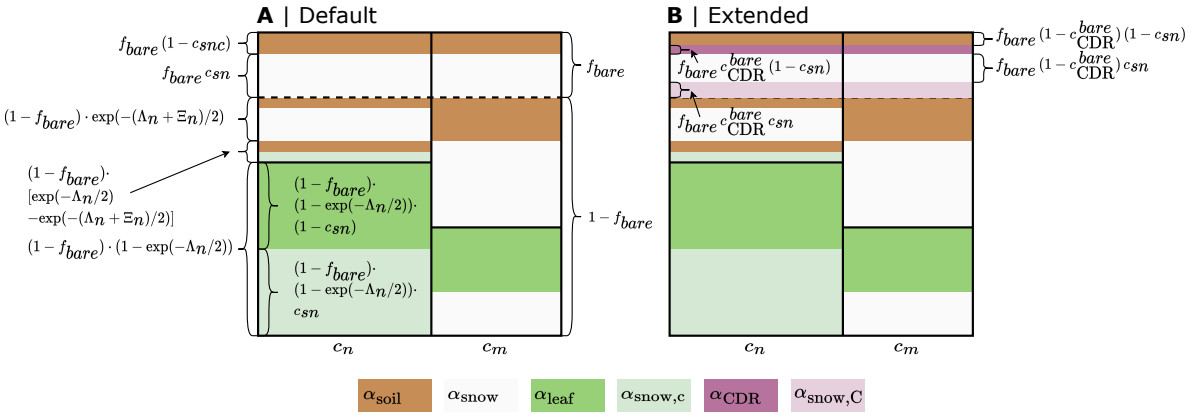

Figure S2 | Default albedo scheme of JSBACH (A) and expanded scheme including implicit CDR through sDACCCS on bare land (B). Tile n represents a forest surface type, and a shrub, grass or crop PFT covers tile m. The expanded scheme only depicts the albedo of implicit sDACCCS cover on land as α_{CDR} and $\alpha_{\mathrm{snow\,C}}$, respectively. The albedo of sDACCCS on vegetated land takes the same value but is already covered by the default scheme. It is, therefore, represented as α_{leaf} in this schematic view. Figure modified and expanded from Reick et al. [68].

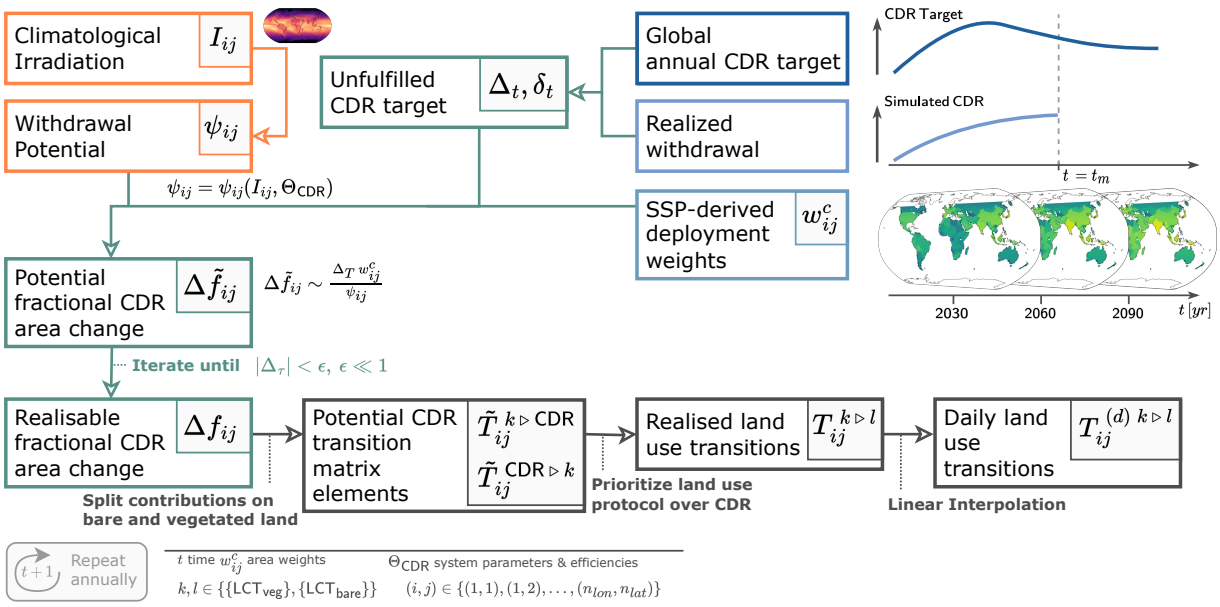

Figure S3 | Process steps and key variables for calculating the sDACCCS deployment target and land use transitions. A first stage covers the computations of the global CDR target (blue). The second stage transfers this target into anticipated fractional area changes of sDACCCS within grid cells, taking the withdrawal within the CDR tile (orange) into account. Finally, the model translates anticipated area changes into actual land cover changes (dark grey) in extension of JSBACH's land cover dynamics.

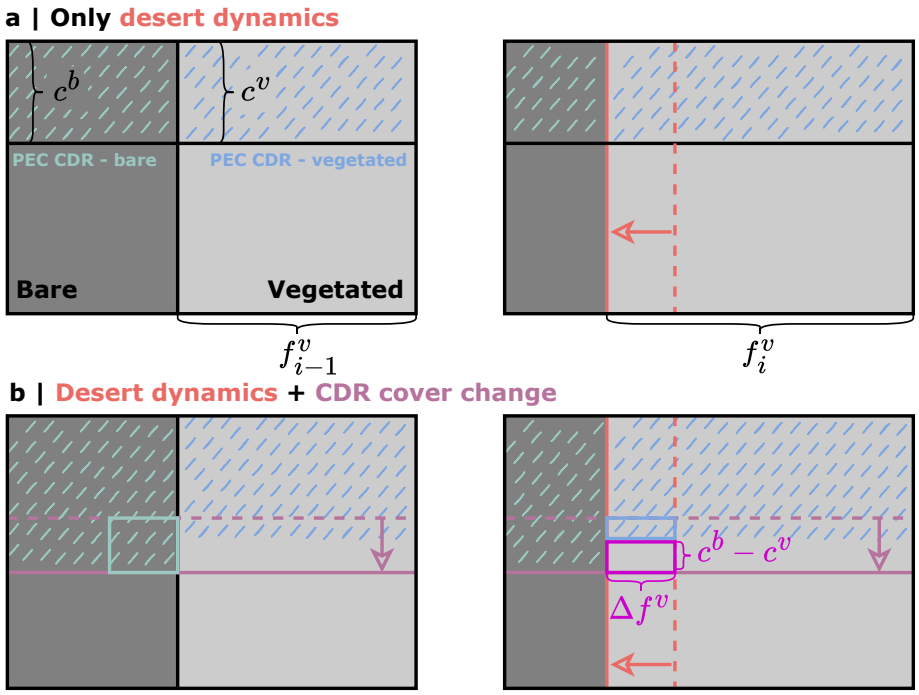

Figure S4 | Combining variations in natural vegetation extent (a) with CDR land cover change can lead to an imbalance between sDACCCS cover fractions on bare and vegetated land (b). Unbalanced cover fractions (magenta) result from unfulfilled CDR land use transitions (violet) on vegetated land if the extent of natural vegetation changes at the same time (red). The subscript CDR of cover fractions is dropped for readability.

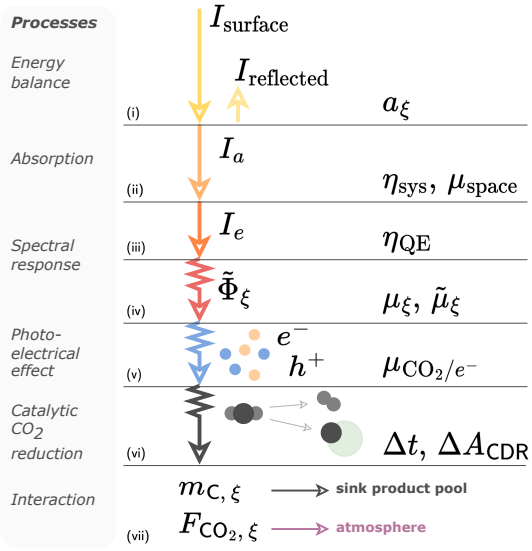

Figure S5 | Zero-dimensional parametrization of sDACCCS with idealized process steps (i) to (vii). Saw-toothed arrows indicate unit conversions through process steps.

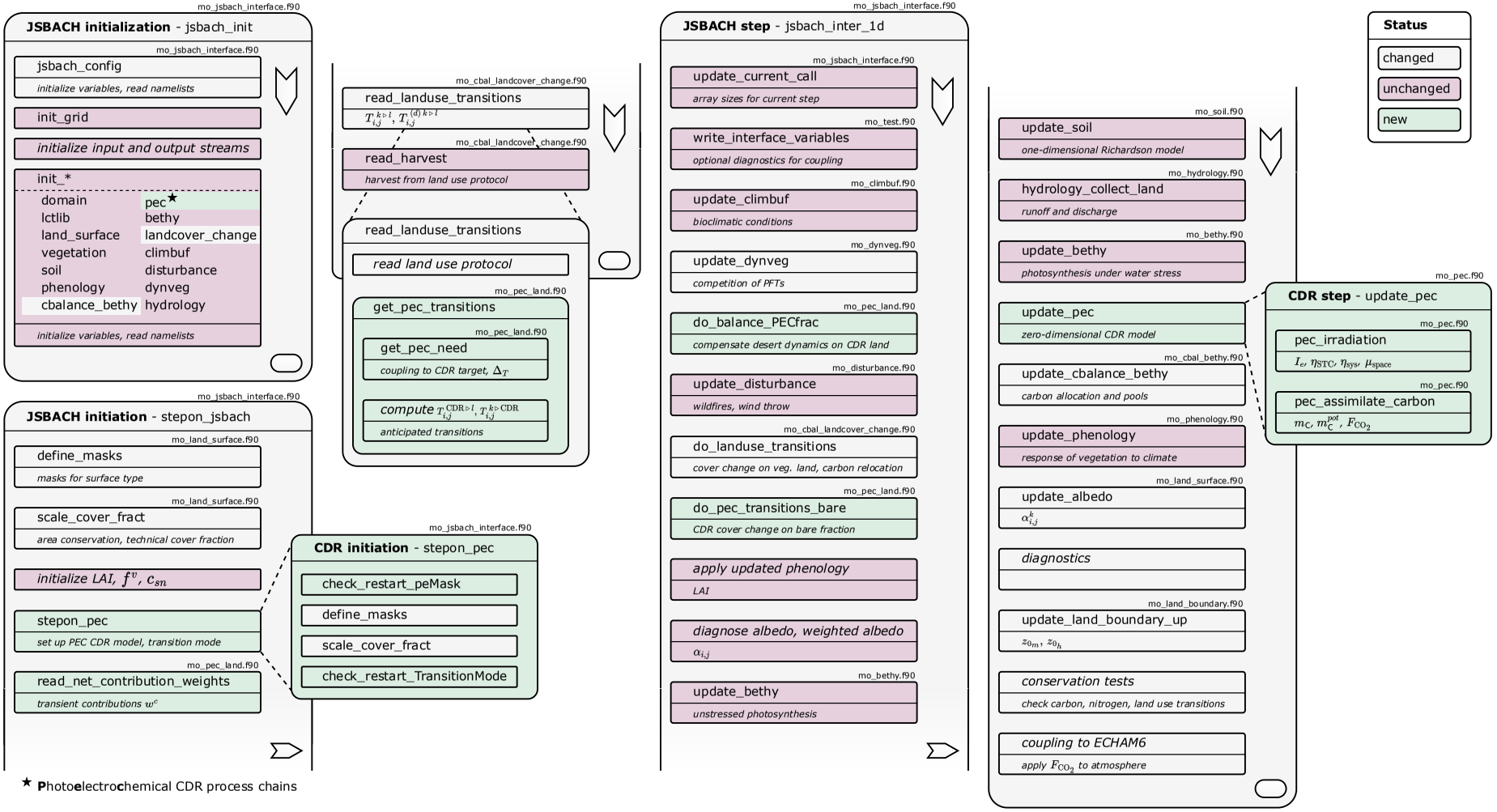

Figure S6 | Implementation of the CDR component in JSBACH's call tree. Initialization and initiation get called at the beginning of a simulation or after a restart. Land use transitions and harvest are read (vegetation)/computed (CDR) once per simulation year. Colors indicate routines and modules involved in representing the sDACCCS chains. Arrows indicate the order of calls.

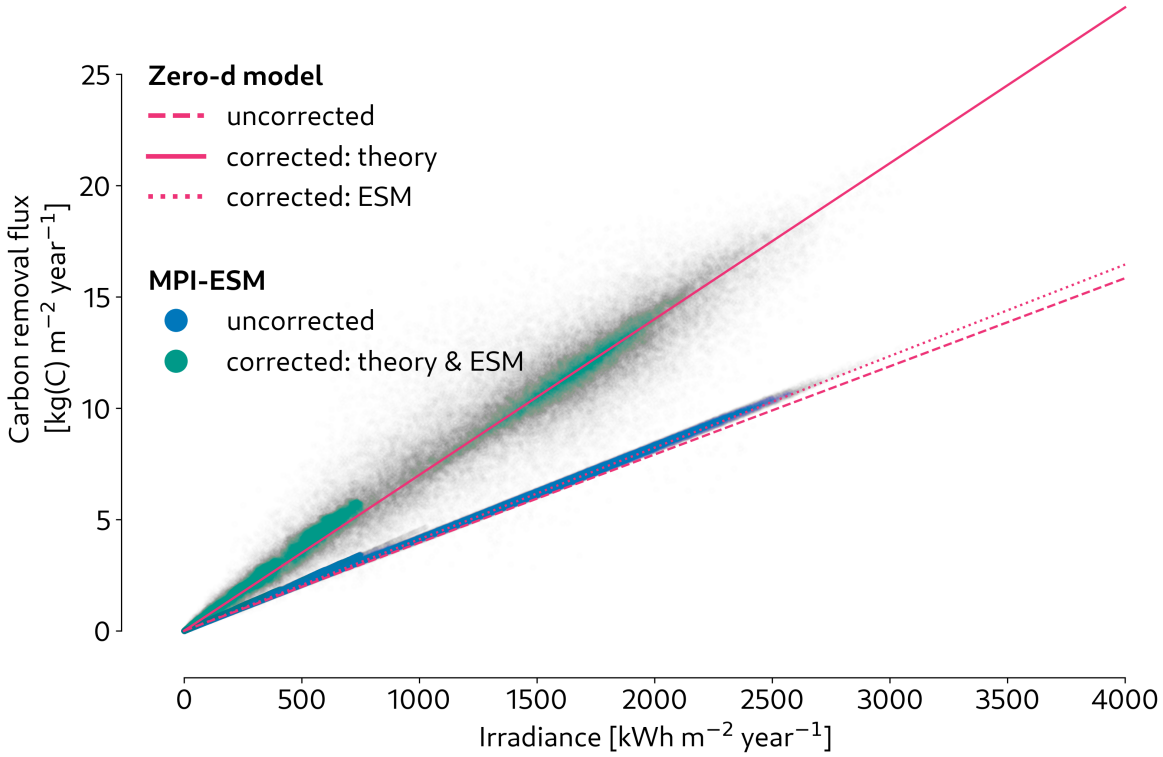

Figure S7 | Initial calibration of the sDACCCS footprint in the zero-dimensional model. First, the theoretically expected carbon removal (dashed line) is corrected for the ESM's response (blue dots). Then, based on this model (dotted line), we compute a calibration factor which causes the ESM's CO_2 removal (green dots) to conform with the theoretical footprint (solid line) deduced by May and Rehfeld [73]. Note that the depicted carbon removal fluxes already comprise the spacing factor converting between the module area of solar absorbers and the sDACCCS land footprint.

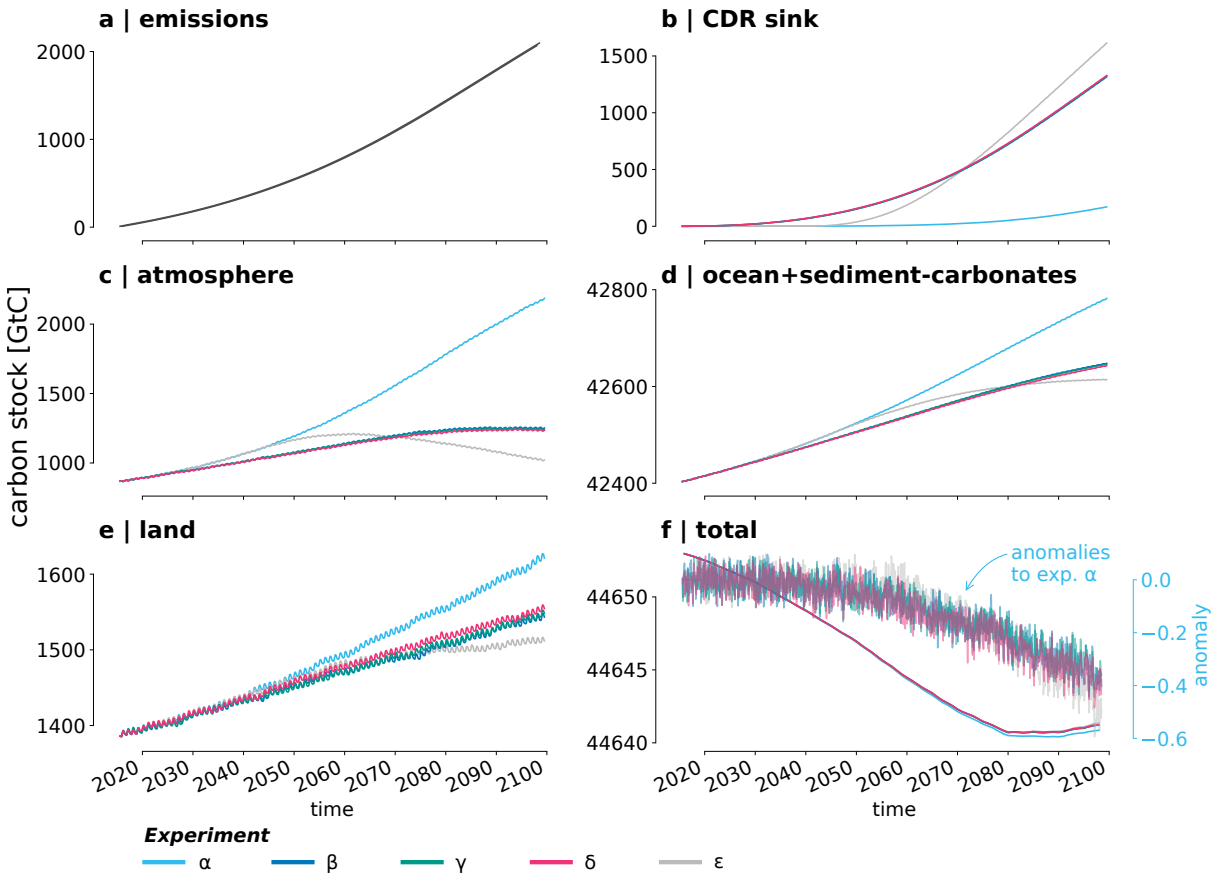

Figure S8 | Global carbon stocks and carbon conservation in simulations with sDACCCS CDR in test simulations spanning a range of CDR pathways under the same emission scenario. To compensate the residual CO_2 forcing of cumulative emissions (a) and CO_2 removal (b), atmospheric (c), marine (d), and terrestrial (e) carbon stocks accumulate carbon. Still, the total carbon budget (f) should be closed and constant. The model does not perfectly reflect this conservation. However, anomalies between different CDR experiments (second scale in f) are < 0.03% of the cumulative emission forcing over 85 simulated years and make up < 5% of the model's total drift. In (a), the emission forcing references the starting point of simulations as zero. The initial model state still includes past anthropogenic forcing.

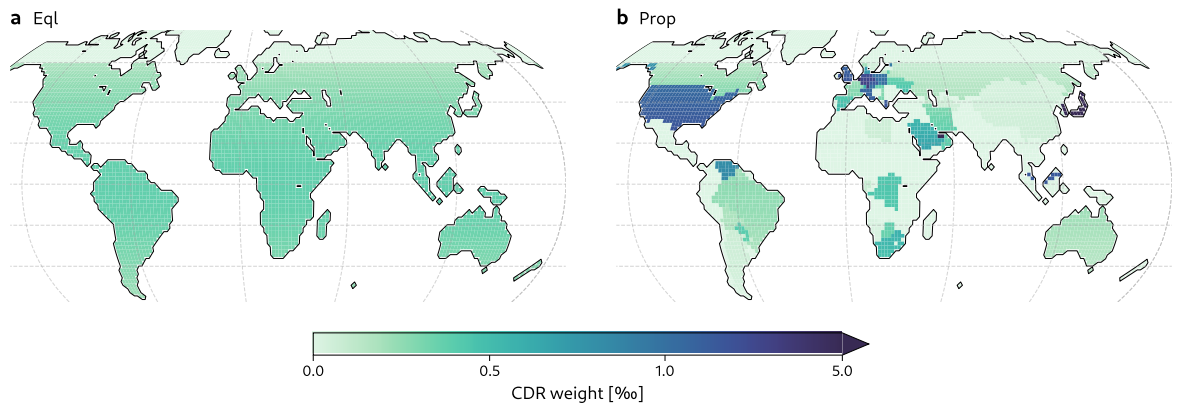

Figure S9 | CDR deployments weights of the Prop (a) and Eql (b) scenarios. Weights are derived from historic emissions (a) and relatively equal contributions (b) while accounting for cell area and permitting sDACCCS deployment only within 60°S and 60°N. In addition to the spatial scenario, CDR deployment is subject to land availability constraints (Figure 2).

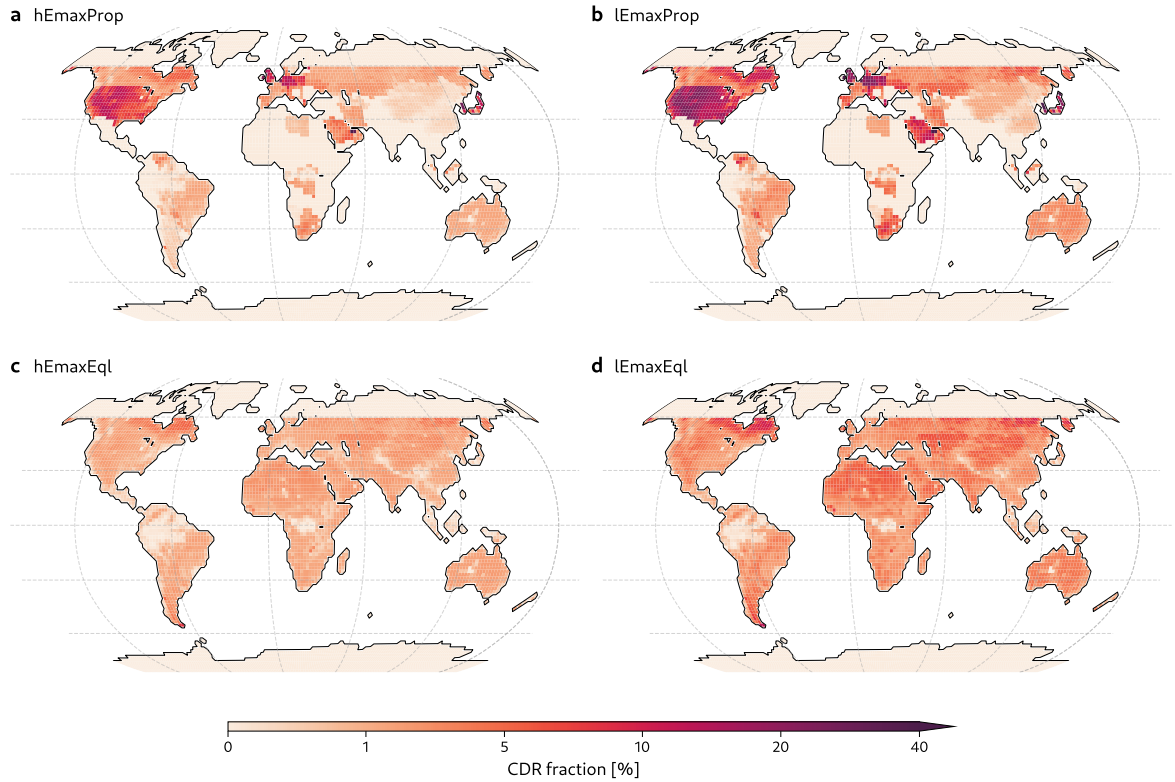

Figure S10 | Mean sDACCCS realized in maxProp (a, b) and maxEql (c, d) experiments during 2110-2139, supplementing Figures 4b, c.

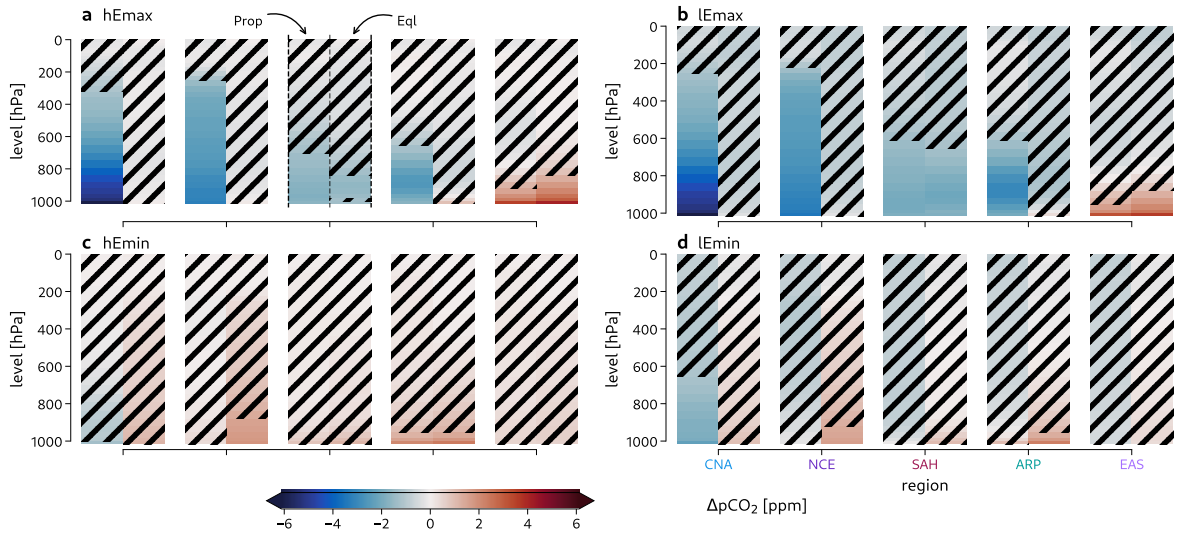

Figure S11 | Mean anomalies of CO_2 concentration along the atmospheric column in selected regions for hEmax (**a**), lEmax (**b**), hEmin (**c**), and lEmin (**d**) during 2110-2139, supplementing Figure 4d.

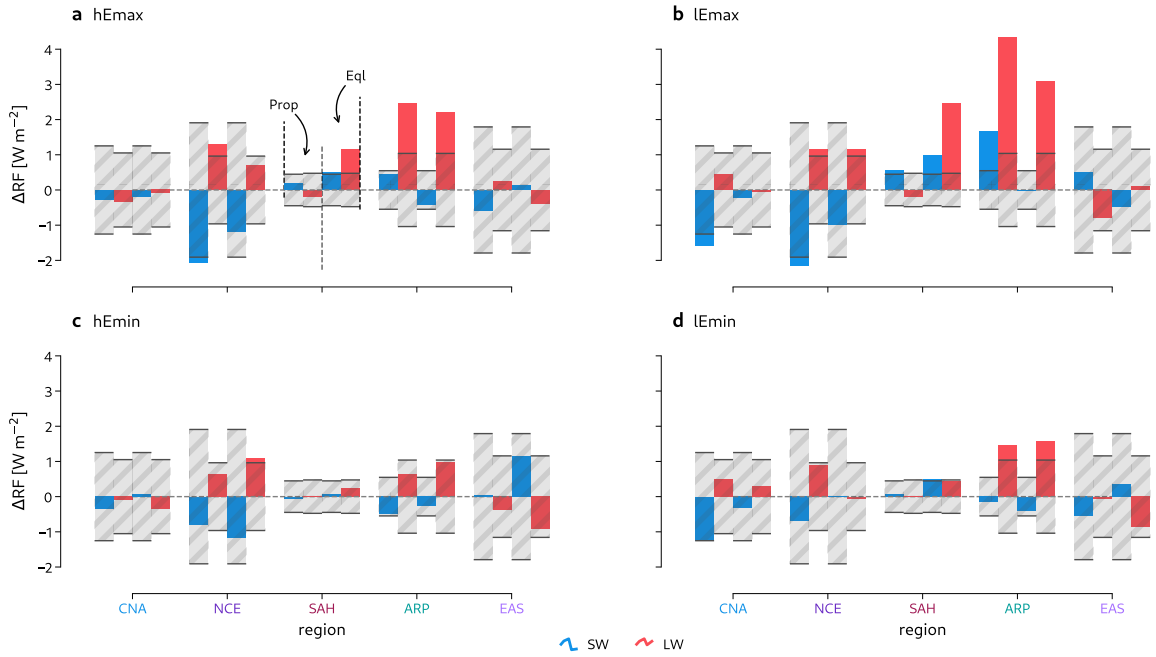

Figure S12 | Mean anomaly of short- (SW) and longwave (LW) radiative forcing at surface in selected regions analogous to Figure S11, supplementing Figure 4e.

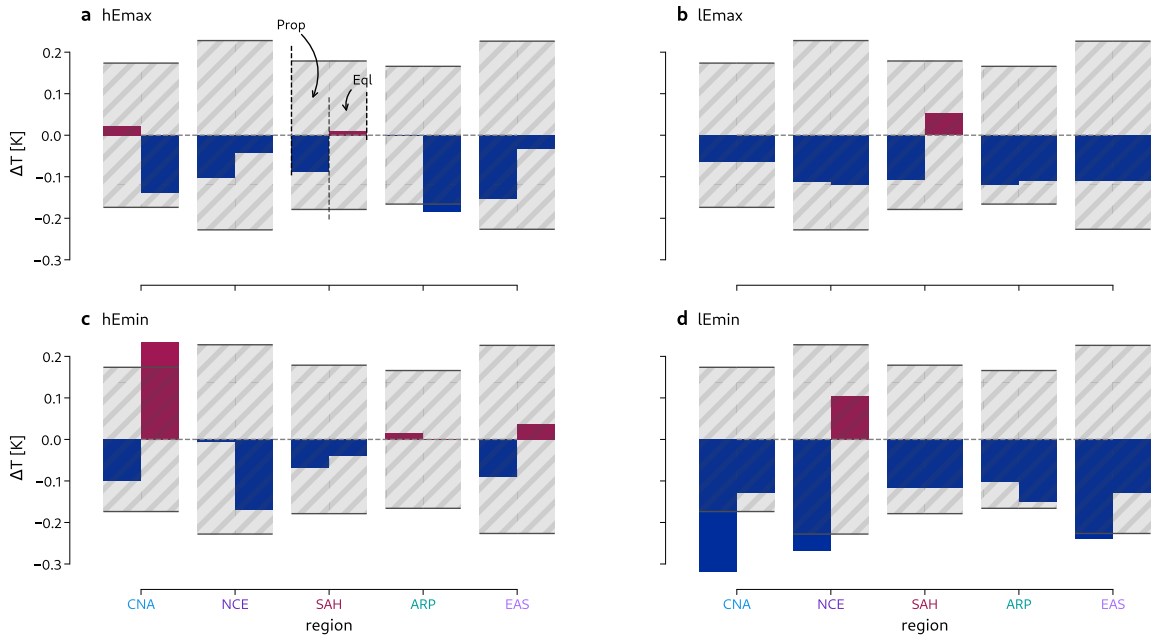

Figure S13 | Mean surface air temperature anomaly in selected regions analogous to Figure S11, supplementing Figure 4f.

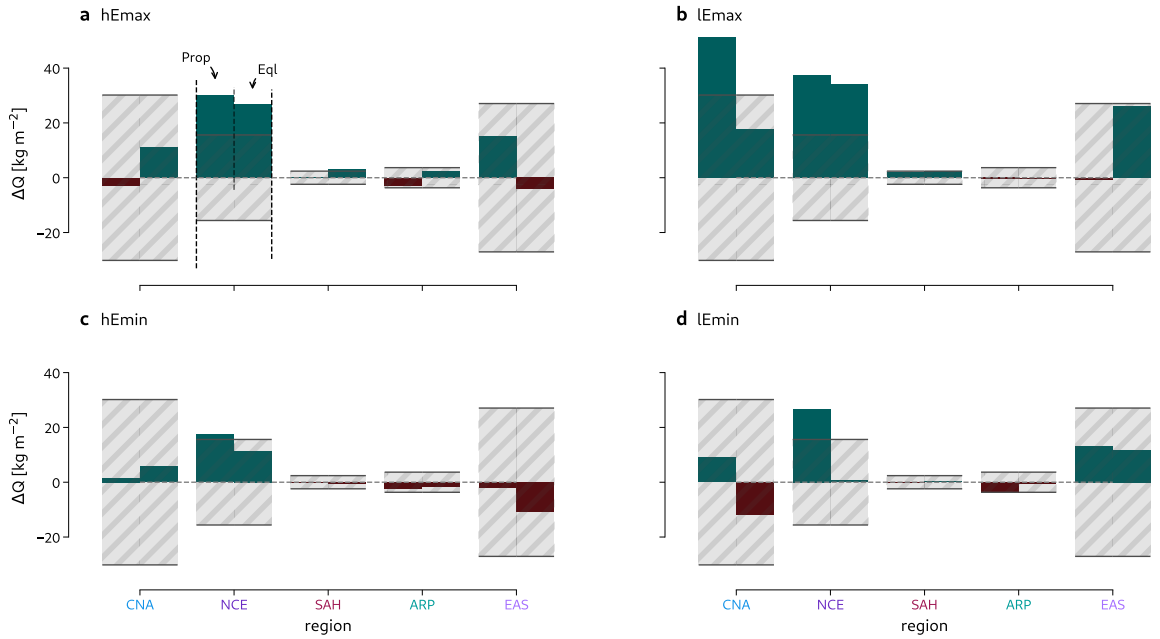

Figure S14 | Mean soil moisture anomaly in selected regions analogous to Figure S11, supplementing Figure 4g.

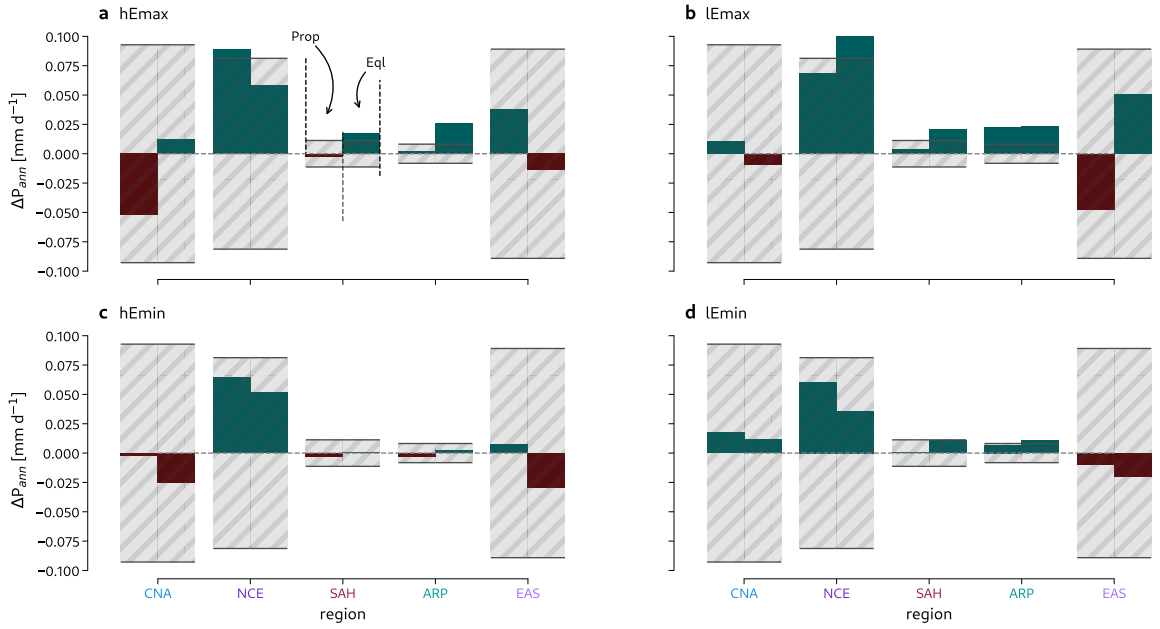

Figure S15 | Mean annual precipitation anomaly in selected regions analogous to Figure S11.

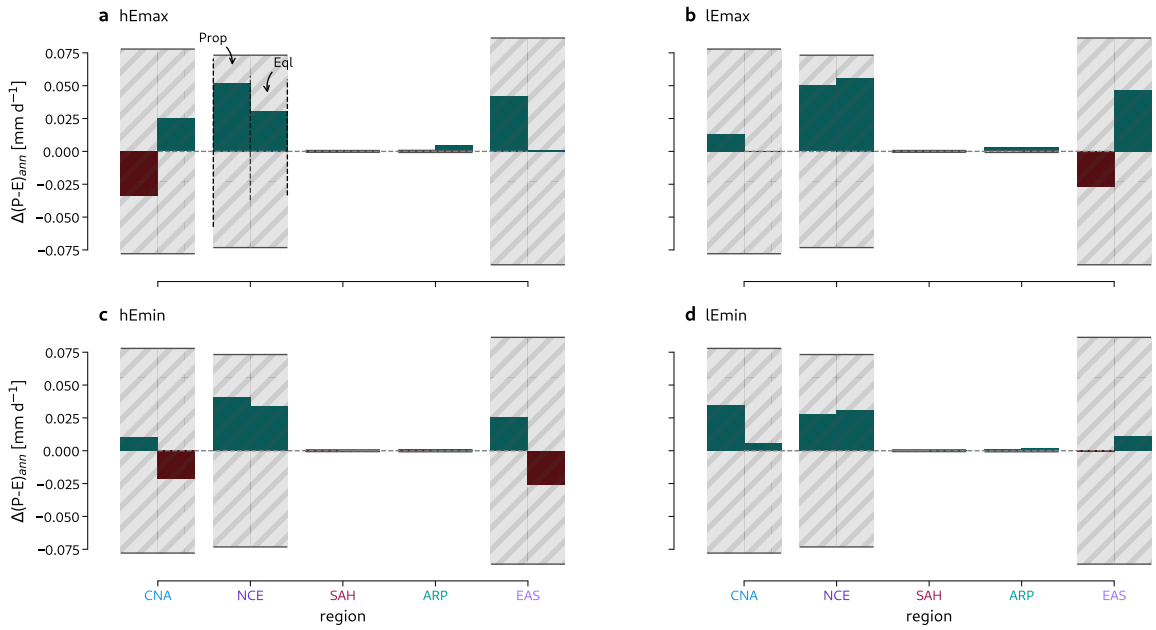

Figure S16 | Mean annual anomaly in moisture availability (precipication minus evaporation) within selected regions analogous to Figure S11.

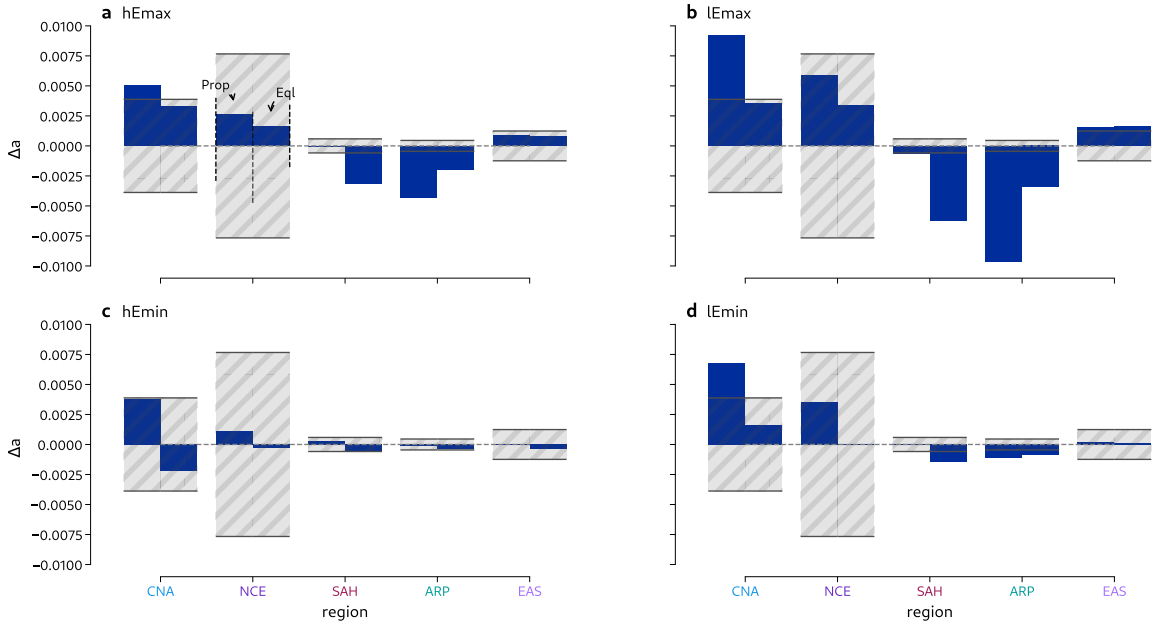

Figure S17 | Mean albedo anomaly in selected regions analogous to Figure S11.

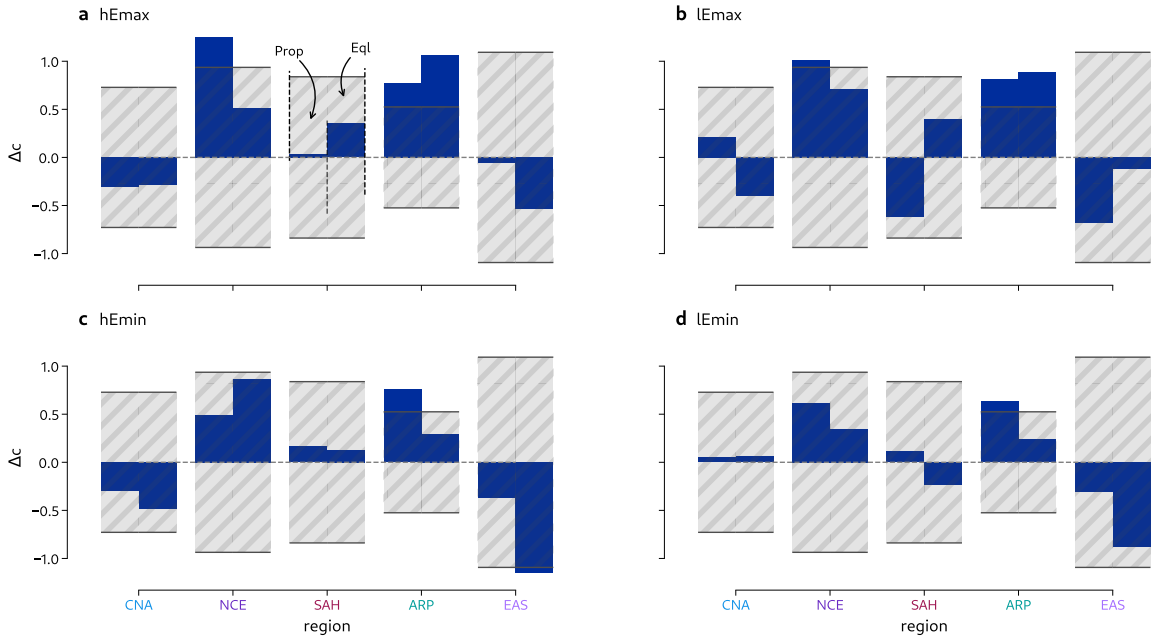

Figure S18 | Mean cloud cover anomaly in selected regions analogous to Figure S11.

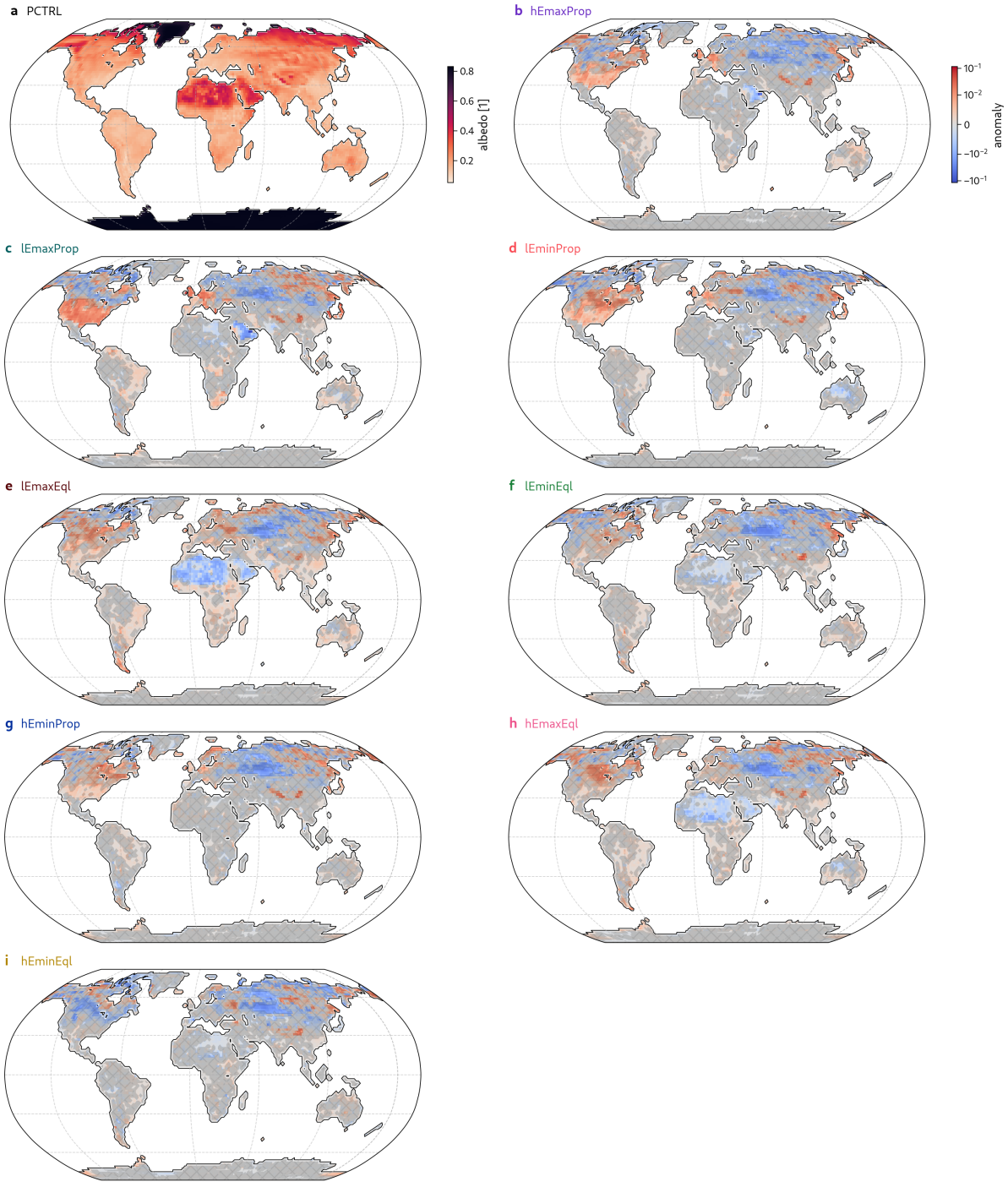

Figure S19 | Climatological anomalies in mean annual surface albedo in reference to the pathway control experiment (PCTRL, **a**) for all sDACCCS experiments (**b–i**) averaged over the reference period for constant CDR (2110–2139). Hatchings indicate insignificant data with respect to the 95th percentile from subsequent 30-year climatologies of the equilibrium control simulation (CTRL).

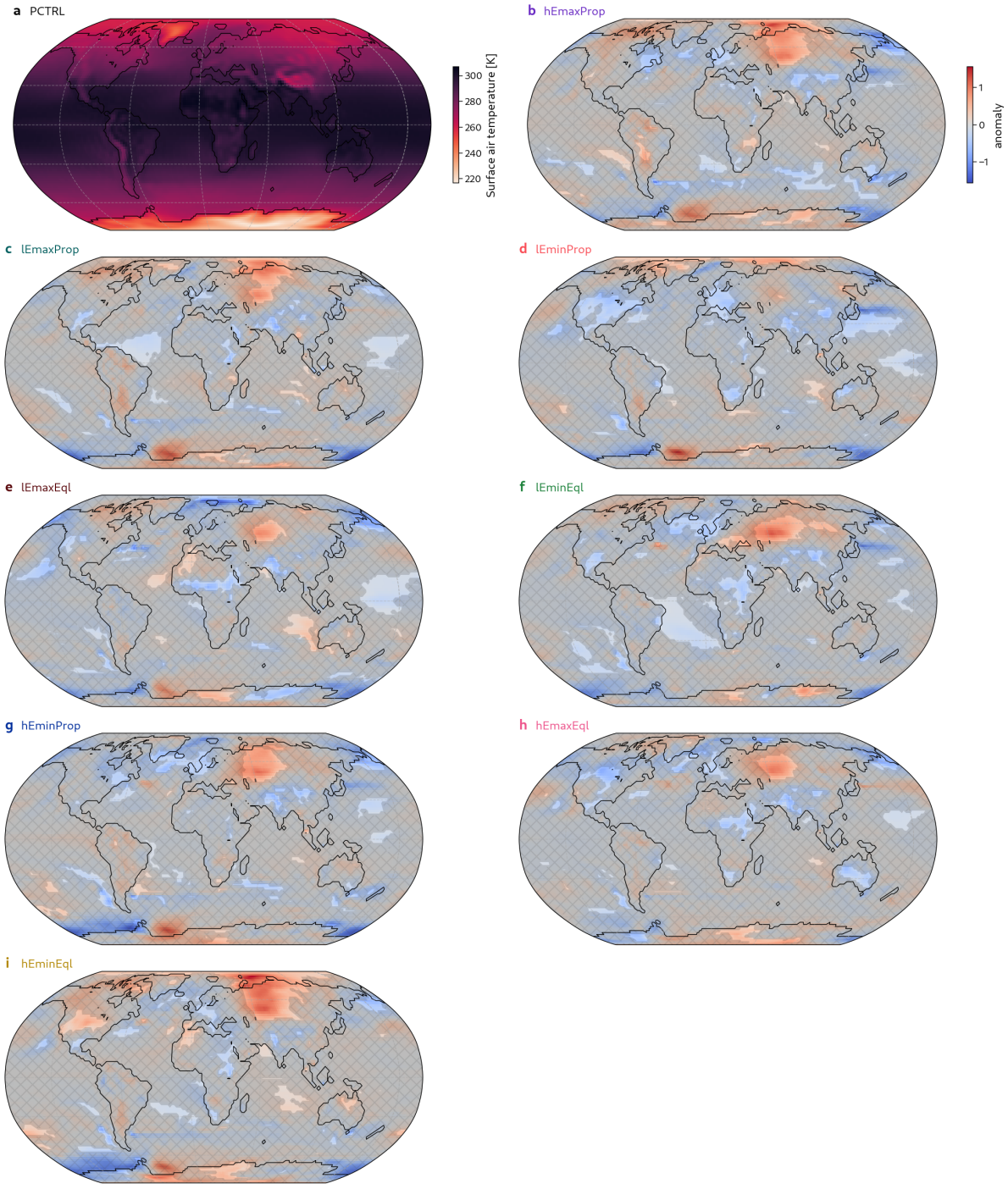

Figure S20 | Climatological anomalies in mean annual surface air temperature analogous to Figure S19.

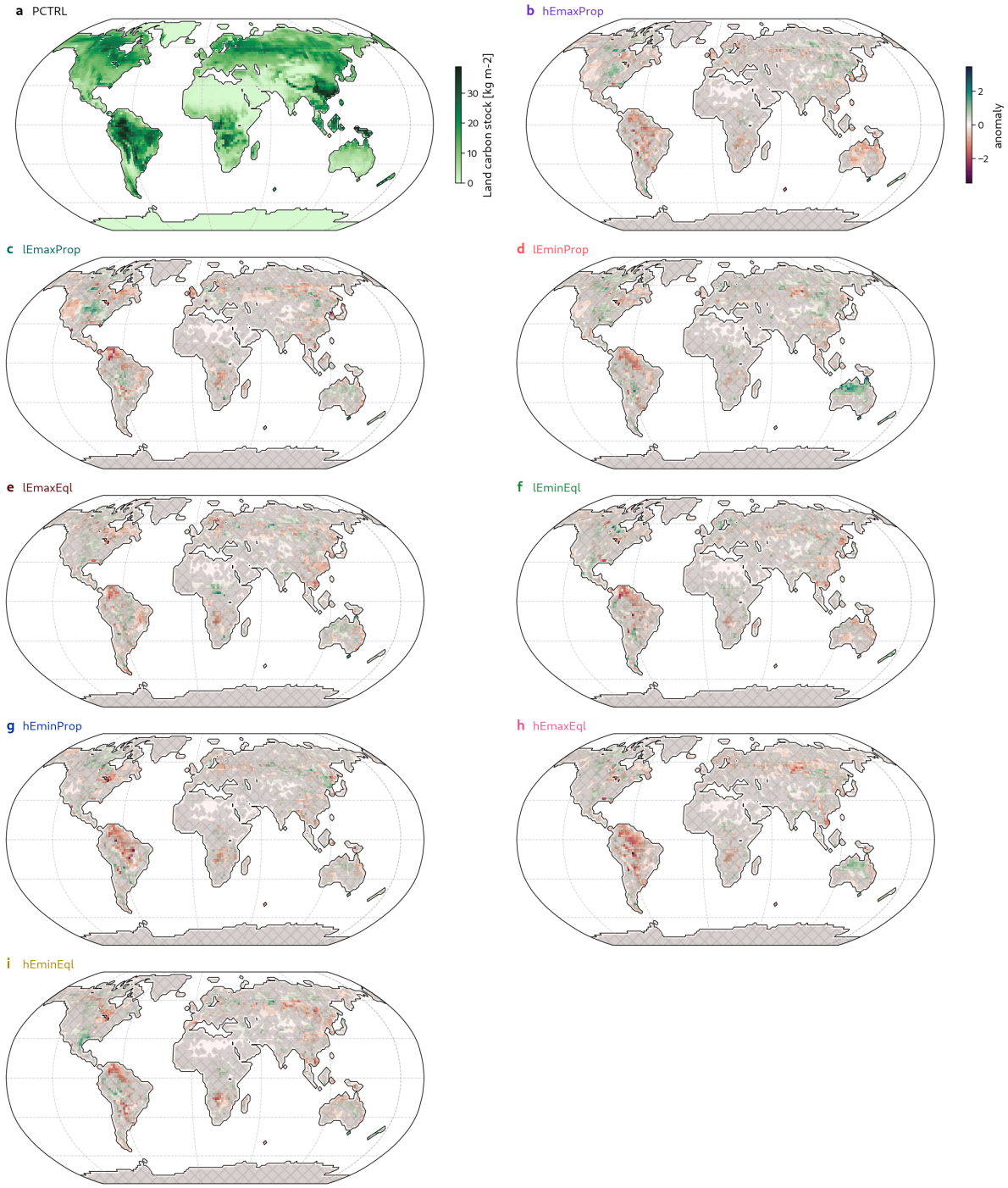

Figure S21 | Climatological anomalies in total land carbon stocks analogous to Figure S19.

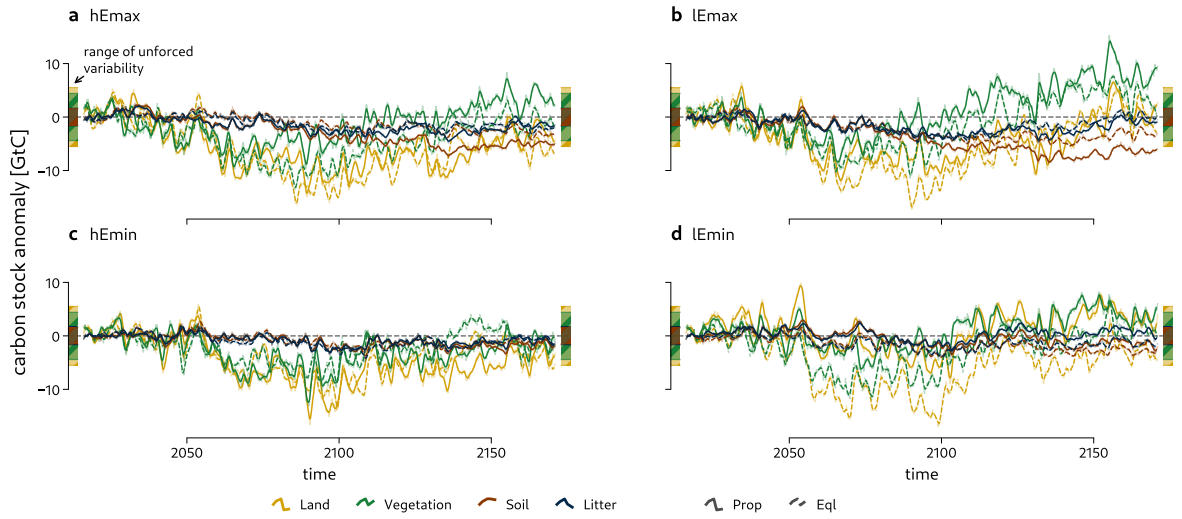

Figure S22 | Global carbon stock response in hEmax (a), and lEmax (b), hEmin (c), and lEmin (d) experiments, supplementing Figure 5a, b.

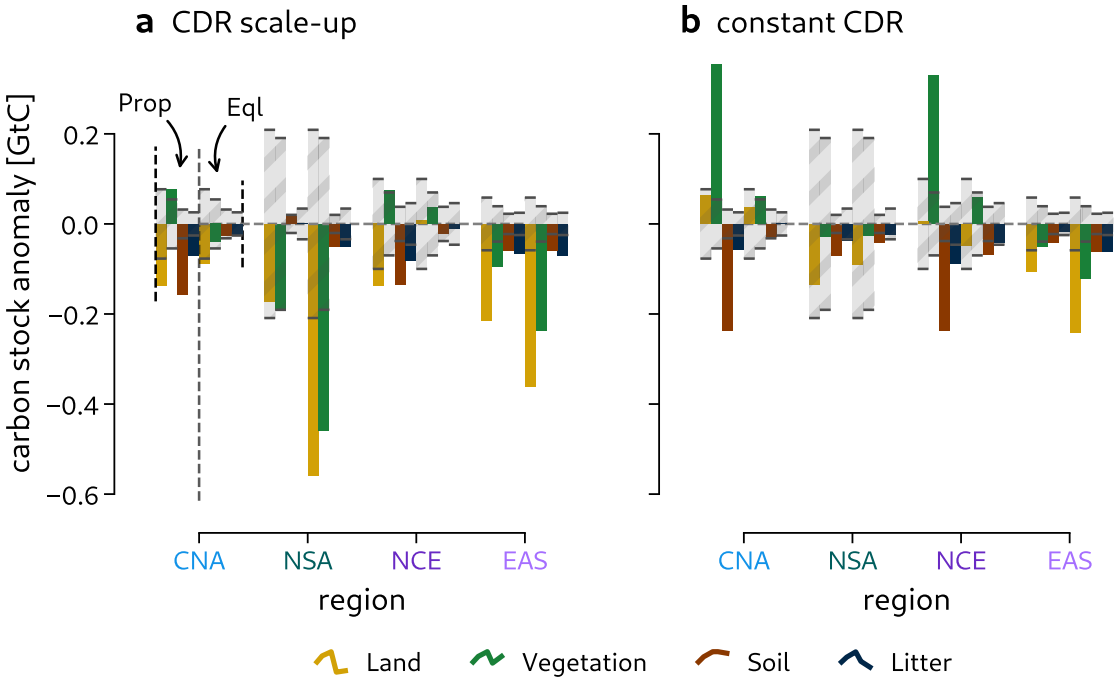

Figure S23 | Total carbon stock anomaly in selected regions within lEmax experiments during the periods of CDR scale-up (**a**) and constant CDR (**b**), supplementing Figure 5c, d.

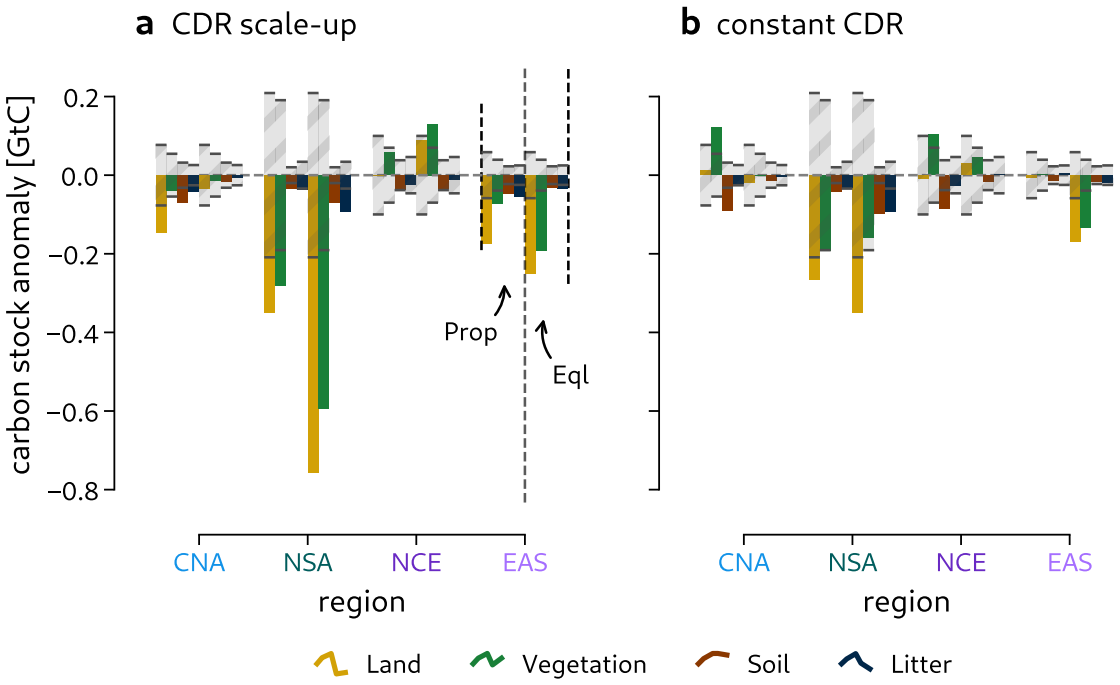

Figure S24 | Total carbon stock anomaly as in Figure S23 but for lEmin experiments.

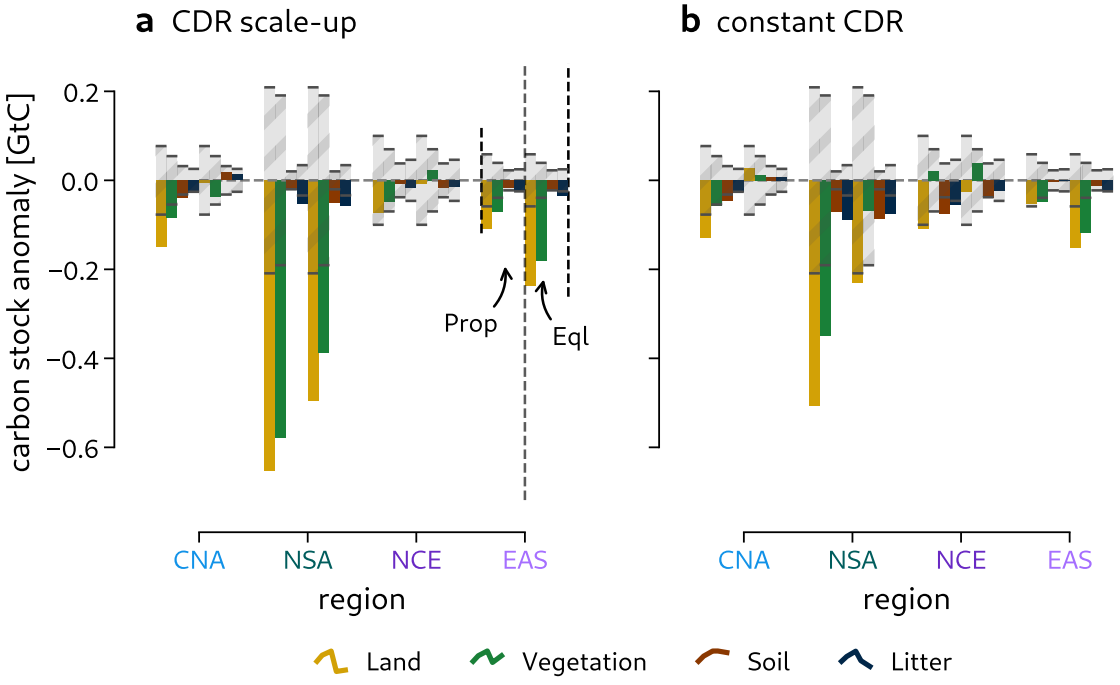

Figure S25 | Total carbon stock anomaly as in Figure S23 but for hEmin experiments.

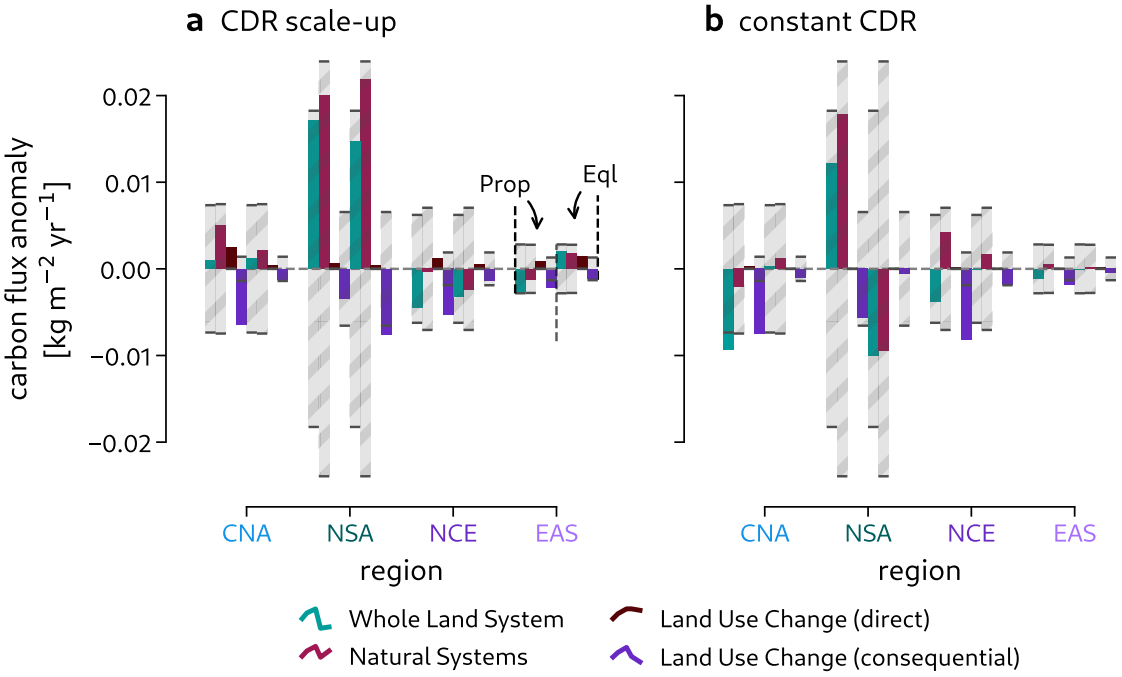

Figure S26 | Mean carbon flux anomaly in selected regions within lEmax experiments during the periods of CDR scale-up (**a**) and constant CDR (**b**), supplementing Figure 5e, f.

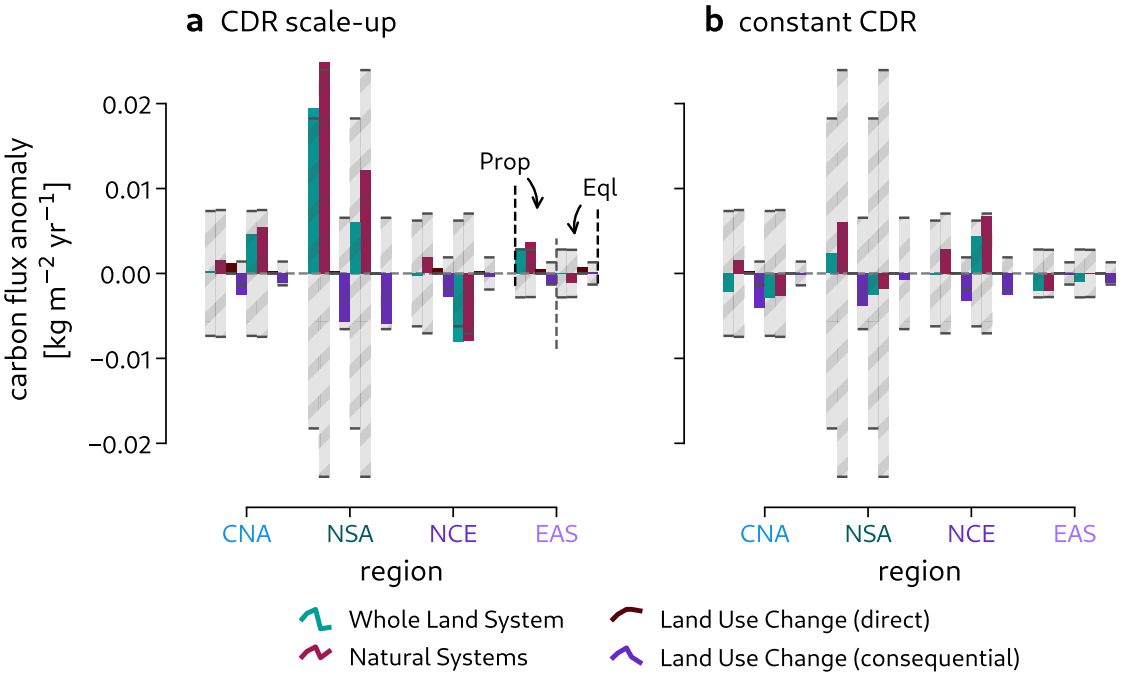

Figure S27 | Mean carbon flux anomaly as in Figure S26 but for lEmin experiments.

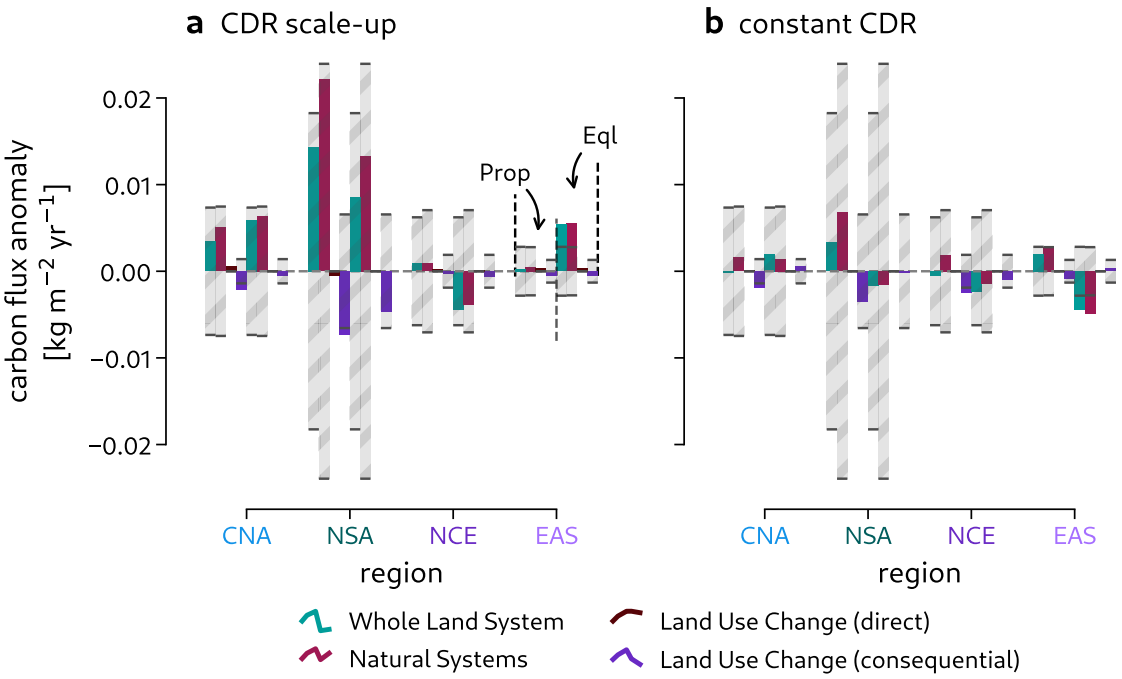

Figure S28 | Mean carbon flux anomaly as in Figure S26 but for hEmin experiments.

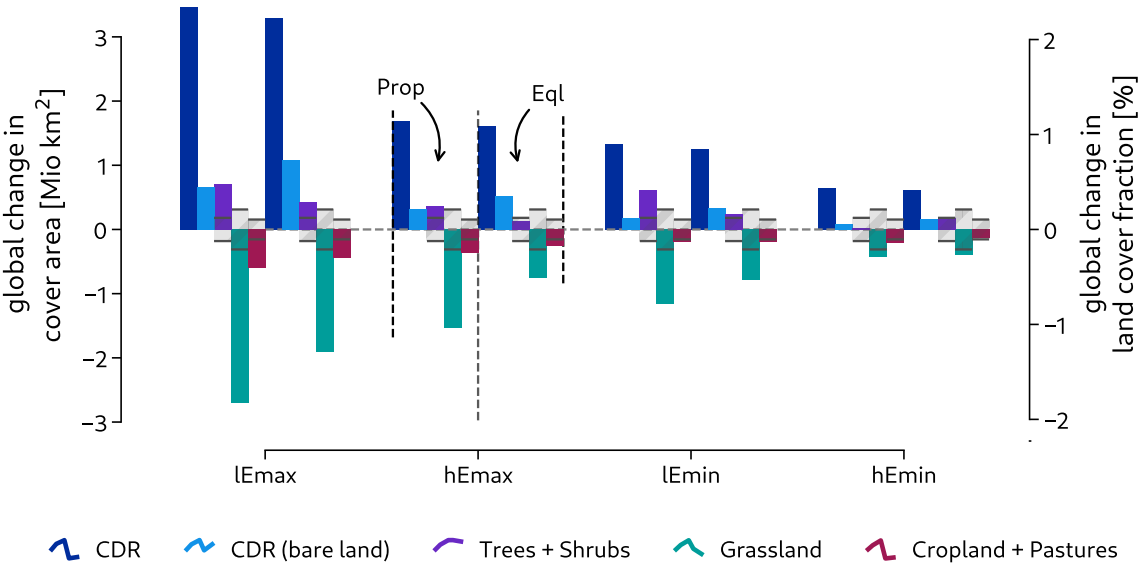

Figure S29 | Mean global changes in area and land cover fraction in the period of constant CDR in sDACCCS experiments compared to PCTRL, supplementing Figure 6a. The total CDR cover also includes the displayed CDR cover on bare land.

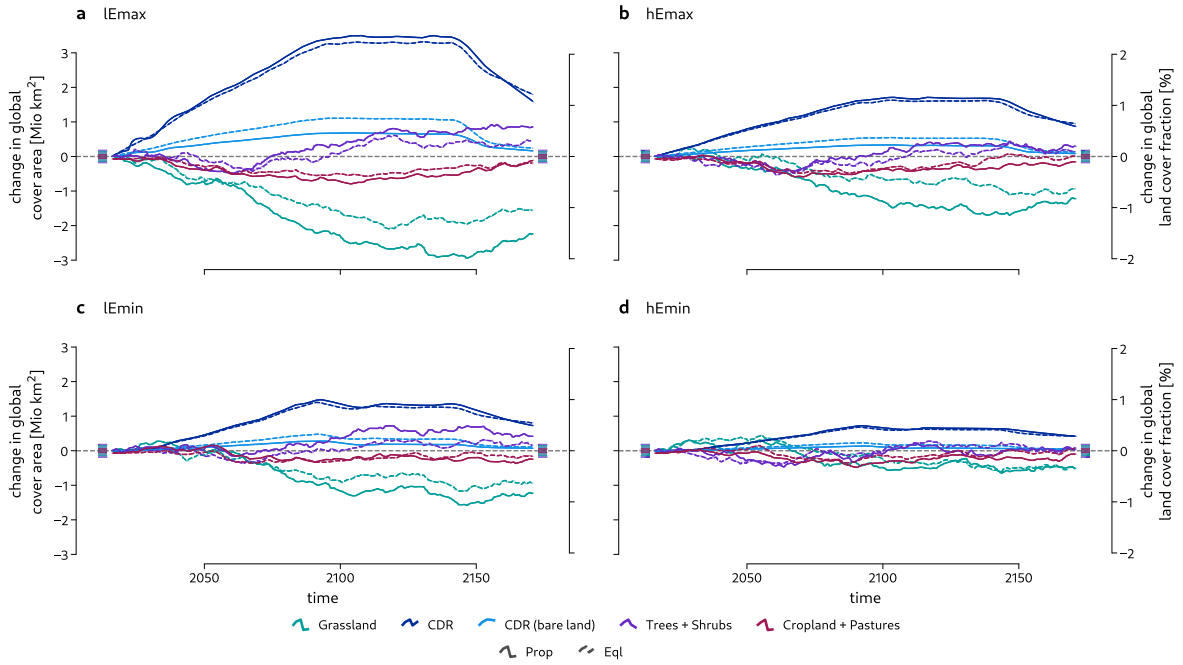

Figure S30 | Global changes in area and land cover fraction over time in lEmax (a), hEmax (b), lEmin (c), and hEmin (d) experiments compared to PCTRL. The total CDR cover also includes the displayed CDR cover on bare land.

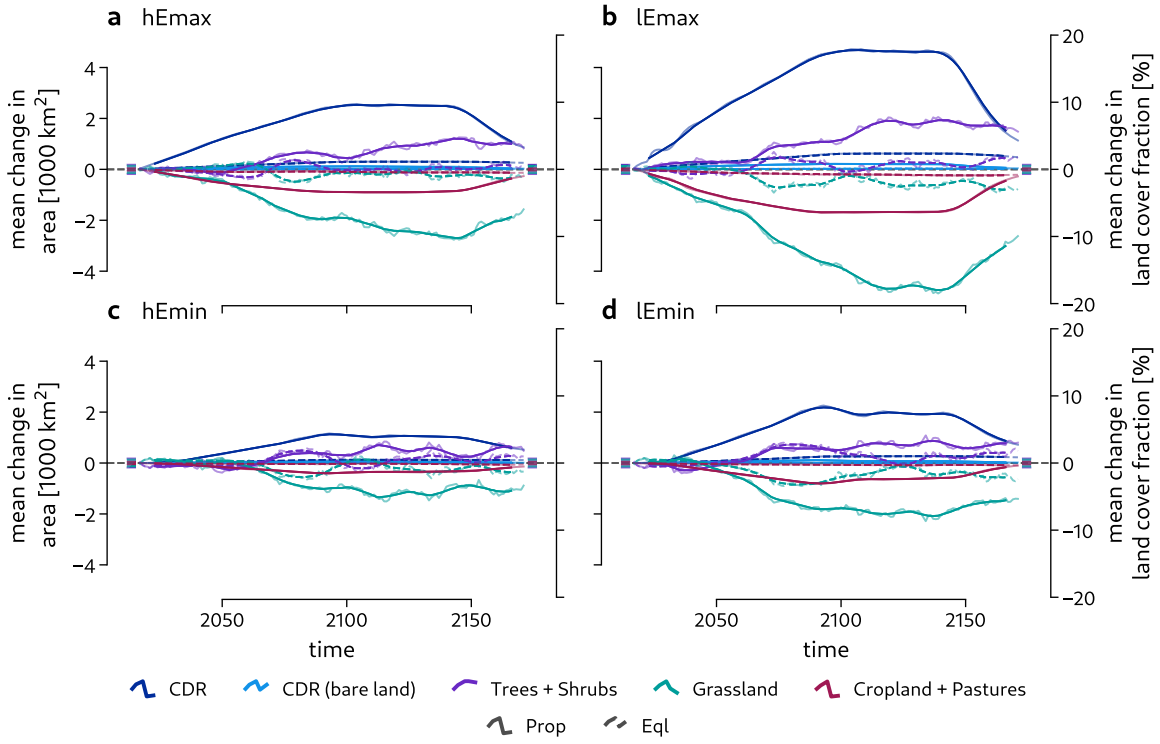

Figure S31 | Land conversions over time in the NCE* region when comparing hEmax **(a)**, hEmin **(b)**, and lEmin **(c)** experiments to PCTRL, supplementing Figure 6b.

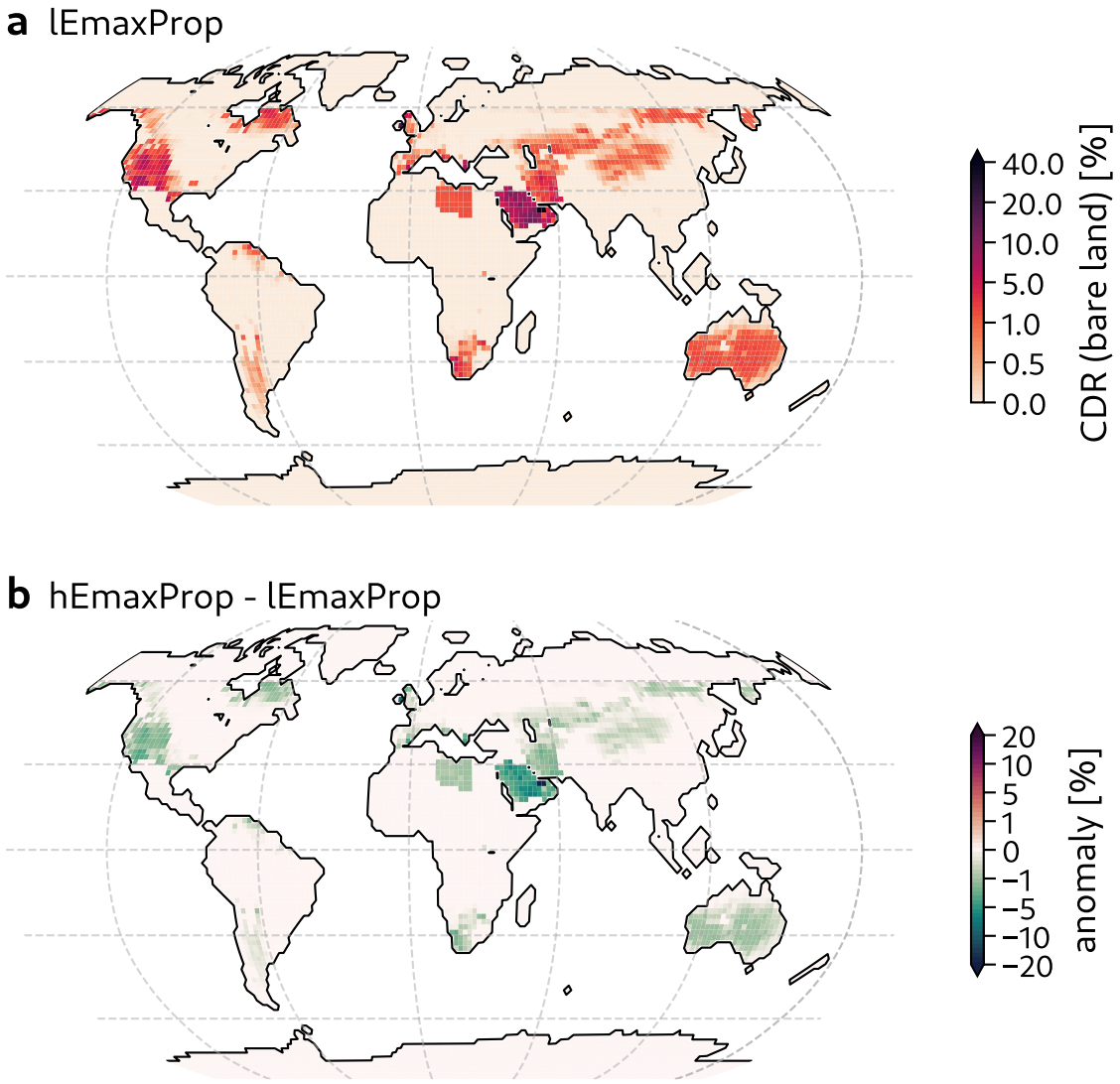

Figure S32 | Total land cover change on the bare fraction of land in lEmaxProp (**a**) and reduced land conversion in hEmaxProp (**b**), supplementing Figure 6c, d.

References – Supplementary Information

[67] C. H. Reick et al. "Representation of natural and anthropogenic land cover change in MPI-ESM". *Journal of Advances in Modeling Earth Systems* 5.3 (2013), 459–482. DOI: 10.1002/jame.20022.

[68] C. H. Reick et al. *JSBACH 3: The land component of the MPI Earth System Model - Documentation of version 3.2*. Reports on Earth System Science / Max Planck Institute for Meteorology. Max Planck Institute for Meteorology, 2021. DOI: 10.17617/2.3279802.

[69] Z. Lu et al. "Impacts of Large-Scale Sahara Solar Farms on Global Climate and Vegetation Cover". *Geophysical Research Letters* 48.2 (2021), 1–10. DOI: 10.1029/2020gl090789.

[70] M. Claussen. "Flux aggregation at large scales: on the limits of validity of the concept of blending height". *Journal of Hydrology* 166.3-4 (1995), 371–382. DOI: 10.1016/0022-1694(94)05098-i.

[71] G. C. Hurtt et al. "Harmonization of global land use change and management for the period 850–2100 (LUH2) for CMIP6". *Geoscientific Model Development* 13.11 (2020), 5425–5464. DOI: 10.5194/gmd-13-5425-2020.

[72] Y. Li et al. "Climate model shows large-scale wind and solar farms in the Sahara increase rain and vegetation". *Science* 361.6406 (2018), 1019–1022. DOI: 10.1126/science.aar5629.

[73] M. M. May and K. Rehfeld. "ESD Ideas: Photoelectrochemical carbon removal as negative emission technology". *Earth System Dynamics* 10.1 (2019), 1–7. DOI: 10.5194/esd-10-1-2019.

[74] M. M. May et al. "On the benchmarking of multi-junction photoelectrochemical fuel generating devices". *Sustainable Energy & Fuels* 1.3 (2017), 492–503. DOI: 10.1039/c6se00083e.

[75] D. W. Keith et al. "A Process for Capturing CO2 from the Atmosphere". *Joule* 2.8 (2018), 1573–1594. DOI: 10.1016/j.joule.2018.05.006.

[76] M. A. Green et al. "Solar cell efficiency tables (Version 61)". *Progress in Photovoltaics: Research and Applications* 31.1 (2023), 3–16. DOI: 10.1002/pip.3646.

[77] M. Schreier et al. "Efficient photosynthesis of carbon monoxide from CO2 using perovskite photovoltaics". *Nature Communications* 6.1 (2015), 7326. DOI: 10.1038/ncomms8326.

[78] J. Hong et al. "Photocatalytic reduction of CO 2 : a brief review on product analysis and systematic methods". *Analytical Methods* 5.5 (2012), 1086–1097. DOI: 10.1039/c2ay26270c.

[79] W. W. Focke et al. "Kinetic interpretation of log-logistic dose-time response curves". *Scientific Reports* 7.1 (2017), 2234. DOI: 10.1038/s41598-017-02474-w.

[80] United States National Renewable Energy Laboratory. *Reference Air Mass 1.5 Spectra*. 2003. URL: https://www.nrel.gov/grid/solar-resource/spectra-am1.5.html.

[81] C. A. Gueymard. "The sun's total and spectral irradiance for solar energy applications and solar radiation models". *Solar Energy* 76.4 (2004), 423–453. DOI: 10.1016/j.solener.2003.08.039.

[82] M. Schreier et al. "Solar conversion of CO2 to CO using Earth-abundant electrocatalysts prepared by atomic layer modification of CuO". *Nature Energy* 2.7 (2017), 17087. DOI: 10.1038/nenergy.2017.87.

[83] Y. Xiao et al. "An artificial photosynthetic system with CO 2 -reducing solar-to-fuel efficiency exceeding 20%". *Journal of Materials Chemistry A* 8.35 (2020), 18310–18317. DOI: 10.1039/d0ta06714h.

[84] W. Gao et al. "Industrial carbon dioxide capture and utilization: state of the art and future challenges". *Chemical Society Reviews* 49.23 (2020), 8584–8686. DOI: 10.1039/d0cs00025f.

[85] A. Francis et al. "A review on recent developments in solar photoreactors for carbon dioxide conversion to fuels". *Journal of CO2 Utilization* 47 (2021), 101515. DOI: 10.1016/j.jcou.2021.101515.

[86] M. Ozkan et al. "Current status and pillars of direct air capture technologies". *iScience* 25.4 (2022), 103990. DOI: 10.1016/j.isci.2022.103990.

[87] A. J. Bard and L. R. Faulkner. "Electrochemical Methods: Fundamentals and Applications" (2001).

[88] K. Riahi et al. "The Shared Socioeconomic Pathways and their energy, land use, and greenhouse gas emissions implications: An overview". *Global Environmental Change* 42 (2017), 153–168. DOI: 10.1016/j.gloenvcha.2016.05.009.

[89] C. L. Fyson et al. "Fair-share carbon dioxide removal increases major emitter responsibility". *Nature Climate Change* 10.9 (2020), 836–841. DOI: 10.1038/s41558-020-0857-2.

[90] ESMAP. *Global Photovoltaic Power Potential by Country*. 2020. URL: https://globalsolaratlas.info/global-pv-potential-study.

[91] M. M. May and K. Rehfeld. "Negative Emissions as the New Frontier of Photoelectrochemical CO2 Reduction". *Advanced Energy Materials* (2022), 2103801. DOI: 10.1002/aenm.202103801.

[92] D. Esrafilzadeh et al. "Room temperature CO2 reduction to solid carbon species on liquid metals featuring atomically thin ceria interfaces". *Nature Communications* 10.1 (2019), 865. DOI: 10.1038/s41467-019-08824-8.

[93] M. Iturbide et al. "An update of IPCC climate reference regions for subcontinental analysis of climate model data: definition and aggregated datasets". *Earth System Science Data* 12.4 (2020), 2959–2970. DOI: 10.5194/essd-12-2959-2020.